

CLARKSON UNIVERSITY

Numerical simulation of particle-laden turbulent flows-Environmental applications

A Dissertation

By

Behtash Tavakoli

Department of Mechanical and Aeronautical Engineering

Submitted in partial fulfillment of the requirements

for the degree of

Doctor of Philosophy

4/3/2015

UMI Number: 3700373

All rights reserved

INFORMATION TO ALL USERS

The quality of this reproduction is dependent upon the quality of the copy submitted.

In the unlikely event that the author did not send a complete manuscript and there are missing pages, these will be noted. Also, if material had to be removed, a note will indicate the deletion.



UMI 3700373

Published by ProQuest LLC (2015). Copyright in the Dissertation held by the Author.

Microform Edition © ProQuest LLC.

All rights reserved. This work is protected against unauthorized copying under Title 17, United States Code



ProQuest LLC.
789 East Eisenhower Parkway
P.O. Box 1346
Ann Arbor, MI 48106 - 1346

Abstract

In first part of the thesis a detailed study of the particulate pollutant distribution by wind flow over a building in an urban area was performed. The accuracy of RANS-RSTM and LES turbulence models for predicted airflow over a square cylinder was first evaluated. These models are then applied for simulating wind flows over the scale-model of the Center of Excellence (CoE) Building. Comparing the simulation results with the experimental data of Kehs et al. (2009) showed that the RSTM predicted the pressure distribution on the building consistent with the measurements, but it could not capture the details of the airflow velocity field around the building. The LES simulation, however, showed good agreement with the PIV data. The LES model was then used for analyzing the particulate pollutants transport and deposition analysis.

Particle motion was modeled using a one-way coupling, Lagrangian approach. Particular attentions were given to the effect of the turbulent velocity fluctuations on particles dispersion and deposition. Instantaneous turbulent velocity fluctuations were simulated using the Langevin stochastic differential equation. The particle transport model in turbulent flows was validated by comparing the predicted deposition velocity for vertical and horizontal channel flows with the existing experimental data and numerical simulation results. Finally the particulate pollutant dispersion and deposition around the scaled CoE Building were investigated using the LES and unsteady particle tracking approach.

In addition, the size-concentration distribution of secondary organic aerosols (SOAs), as an indoor air aldehyde pollutant, was numerically modeled. The population balance equation of the SOAs was solved using the method of moments (MOM). To close the

model, particle size distribution was assumed to follow a lognormal distribution, which was based on the experimental data of Chen and Hopke (2009). The nucleation of SOAs from the chemical reaction of α -pinene (a common emission from indoor furniture), and ozone in the air, as well as, their Brownian coagulation and the surface growth were considered in the numerical model. The computational model was evaluated by comparison with the experimental data of Chen and Hopke (2009).

The MOM was used for modeling the distribution of the SOAs in an office space. The concentrations of SOAs in the breathing zone of an occupant in the room were evaluated for two mixed-mode ventilation systems. The simulation results showed that the pollution concentration in the ventilation system with the air outlet placed in the ceiling was smaller than the one in which the air outlet was in the floor behind the manikin model.

Acknowledgements

I would like to express my special appreciation to my advisor Professor Goodarz Ahmadi for countless reasons. Even before I knew you, the research you and Dr. Omid Abouali were conducting about drug delivery and air inhalation in human respiratory system motivated me to pursue my graduate study at Shiraz University in 2005. Thereafter, I have been taking the advantage of your tree of knowledge. I am greatly thankful for your unconditional supports and opportunities during all these years. Beside the science you shared with me, I grasped an outlook on life and a wish to continue developing my competences and helping others to do so.

I would also like to thank my committee members, Professor John B. McLaughlin, Professor Suresh Dhaniyala, Professor Brian Helenbrook and Professor Andrea R. Ferro for your time and for examining and correction of this document. Your suggestions added value to this dissertation. Also, I appreciate the opportunities I received from the Department of Mechanical and Aeronautical Engineering, especially thanks to Professor Aidun for his advice, Professor Dhaniyala for what you taught about how to develop an innovative solution for a problem, and to Professor Helenbrook for what you taught about how to develop an engineering problem to investigate a physical phenomenon.

This work was not possible without the supports and productive suggestions I received from Fariddudin Behzad and Behrang Sajjadi. I appreciate your friendship.

At the end I would like to express appreciation to my beloved parents Khosrow and Shahrzad and my sister, Behnoosh, for all the sacrifices you have made on my behalf. I am grateful to you for your continuous support and encouragements.

TABLE OF CONTENTS

Chapter	Page
ABSTRACT	i
ACKNOWLEDGEMENTS	iii
TABLE OF FIGURES	vi
CHAPTER I. Introduction	
1.1 Outdoor air pollution	1
1.1.1 Air flow around wall mounted square cylinder	1
1.1.2 Wind flow around a building with a complex geometry	5
1.1.3 Particle transport in the turbulent flow	7
1.2 The secondary organic aerosols (SOAs) - pollution in indoor air	12
1.2.1 The numerical model of nucleation, coagulation and surface growth of SOAs in a dynamic mixing chamber	12
1.2.2 Effect of indoor air ventilation on particulate pollutant concentration distribution, including nucleation, coagulation and surface growth	17
1.3 Objectives	18
CHAPTER II. Computational model of airflow around an obstacle with complex geometry	
Abstract	20
2.1 Computational domain and boundary conditions	22
2.1.1 Computational domain and boundary conditions of the air flow model around the wall mounted square cylinder	22
2.1.2 Computational domain and boundary condition of the model of wind flow around the CoE Building	24
2.2 Governing equations	28
2.3 Results and discussion	33
2.3.1 Simulation of airflow around the wall mounted square cylinder	33
2.3.2 Simulation of wind flow around the CoE Building	37
2.3.2.1 Wind load and pressure field around the CoE Building	37
2.3.2.2 Velocity field around CoE building for the wind from north to south	46
2.4 Conclusions	50
References	51
CHAPTER III. Computational model of particle distribution and deposition over an obstacle with complex geometry	
Abstract	53
3.1 Introduction	54
3.2 Computational model and boundary conditions	55
3.2.1 Numerical model of particle transport in a 2D channel flow	55
3.3 Governing equations	57

3.3.1	Particle transport equation	57
3.3.2	Continuous Random Walk (CRW) Model for turbulent velocity fluctuations in RANS-RSTM turbulence model	60
3.3.3	Continuous Random Walk (CRW) Model of turbulent velocity fluctuations in LES	62
3.4	Results and discussions	64
3.4.1	Effect of turbulent velocity fluctuations on particle deposition rate in a channel flow	64
3.4.1.1	Channel flow	64
3.4.1.2	Particle distribution in a 2D channel flow	68
3.4.2	Particle deposition on the CoE Building model	74
3.5	Conclusions	82
	References	84
CHAPTER IV. Indoor secondary organic aerosols formation- Computer modeling of coagulation, surface growth and nucleation		
	Abstract	86
4.1	Introduction	88
4.2	Governing Equations	90
4.2.1	Population balance equation	90
4.2.2	Method of Moments (MOMs)	92
4.2.3	Coagulation	94
4.2.4	Surface growth	95
4.2.5	Nucleation	97
4.2.6	Conversion of moments to particle concentration	98
4.3	Validation of the numerical simulation for Brownian coagulation	98
4.4	Results and discussion	101
4.5	Distribution of SOAs in an office with mixed-mode ventilation system ..	104
4.5.1	Introduction	104
4.5.2	Results and discussion	106
4.6	Conclusions	110
	References	112
	CONCLUSIONS	114
	FUTURE WORKS	117
	REFERENCES	120
	APPENDIX	134

TABLE OF FIGURES

Figure		Page
Figure 1.1	The horse shoe flow over a square cylinder (Martinuzzi and Tropea 1993).....	2
Figure 1.2	The oil-film visualization of the surface flow patterns for the flow around the square cylinder (Hussein and Martinuzzi 1996).....	2
Figure 1.3	Location of the CoE building on the map.....	7
Figure 2.1	Center of Excellence Building at the intersection of Interstate Highways 81 and 629 at Syracuse, NY.....	21
Figure 2.2	Computational domain of the wall mounted square cylinder in a channel flow. Cube dimension = 25×25×25 mm ³	22
Figure 2.3	The plan view of the size distribution of girds in the numerical domain.....	23
Figure 2.4	Computational grid for flow analysis around the CoE Building.....	25
Figure 2.5	Contours of y^+ for the nearest grid point on the walls of the CoE building model for the wind speed of 10 m/s using the RANS-RSTM. (a) Contours of y^+ on the walls behind the building. (b) Contours of y^+ on the front walls facing the wind.....	27
Figure 2.6	Contours of y^+ on the walls of the CoE building model for wind speed of 10 m/s using LES. (a) Contours of y^+ on the walls behind the building. (b) Contours of y^+ on the front walls facing the wind...	28
Figure 2.7	The comparison of the velocity contours predicted by RSTM and LES.....	33
Figure 2.8	Comparison of the flow around the block in the channel, modeled by RSTM and LES and the LDV experimental data of Hussein and Martinuzzi (1996).....	35
Figure 2.9	The instantaneous and time-averaged velocity contours and streamlines around the obstacle as predicted by LES. (a) and (c) show instantaneous and time-averaged velocity contours along the plane $y/H = 0.5$. (b) and (d) are the 3D instantaneous and time-averaged streamlines introduced at a front line on the plane $y/H = 0.5$	36
Figure 2.10	Pressure data on the west side wall, wind from north at $Re = 81200$ ($U_\infty = 10$ m/s).....	38
Figure 2.11	Pressure data on the east wall (side face), wind from north at $Re = 81200$ ($U_\infty = 10$ m/s).....	38
Figure 2.12	Pressure data on the north wall (windward face), wind from north at $Re = 81200$ ($U_\infty = 10$ m/s).....	39

Figure 2.13	Pressure data on the south wall (downwind face), wind from north at $Re = 81200$ ($U_{\infty} = 10$ m/s).....	40
Figure 2.14	Pressure data on the roof (top face), wind from north at $Re = 81200$ ($U_{\infty} = 10$ m/s).....	40
Figure 2.15	Pressure data on the west wall (windward face), wind from west at $Re = 81200$ ($U_{\infty} = 10$ m/s).....	42
Figure 2.16	Pressure data on the east wall (downwind face), wind from west at $Re = 81200$ ($U_{\infty} = 10$ m/s).....	43
Figure 2.17	Pressure data on the north wall (side face), the wind from west at $Re = 81200$ ($U_{\infty} = 10$ m/s).....	44
Figure 2.18	Pressure data on the south wall (side face), the wind from west at $Re = 81200$ ($U_{\infty} = 10$ m/s).....	44
Figure 2.19	Pressure data on the roof (top face), wind from west at $Re = 81200$ ($U_{\infty} = 10$ m/s).....	45
Figure 2.20	Position of Planes (X1) and (X2), wind blowing from north to south.....	46
Figure 2.21	Comparison of the mean normalized velocity structures between the PIV experiment of Kehs et al. (2009), RSTM and LES for wind at $Re = 81200$ ($U_0 = 10$ m/s) on Plane X1.....	48
Figure 2.22	Comparison of mean normalized out of plane vorticity between the PIV experiment, RSTM and LES for the wind with $Re = 81,200$ ($U_0 = 10$ m/s) on Plane X1.....	49
Figure 2.23	Comparison of the flow field on plane X2, (a) PIV measurements, (b) RSTM turbulence model, and (c) LES model.....	50
Figure 3.1	Contours and profile of streamwise velocity in a 2D channel flow...	65
Figure 3.2	Contours and profile of turbulent kinetic energy in the channel flow.....	65
Figure 3.3	Reconstruction of the velocity fluctuations using Langevin stochastic equations (Eq. 3.8). On the left the contours of velocity fluctuations and on the right their magnitude on the center-line of the cross section passing the middle of channel are shown.....	66
Figure 3.4	Comparison of the root mean-square velocity fluctuations modeled through CRW and the square root of the time averaged Reynolds stress from RSTM.....	67
Figure 3.5	Comparison of the profile of the normalized root mean square of the velocity fluctuations by CRW model, Equation (3.8), shown by black diamond marks, and RSTM turbulence model, which are red the square marks.....	68
Figure 3.6	Comparison of particle distribution in the vertical (left) and	

	horizontal channel flow for particles in sizes of 3 μm (top) and 30 μm (bottom).....	70
Figure 3.7	Deposition velocities of particles in a vertical channel, comparison of the current simulation (RSTM and CRW model) with previous experimental and numerical data.....	73
Figure 3.8	Deposition velocities of particles in a horizontal channel, comparison of the current simulation, (RSTM and CRW model) with previous experimental and numerical data.....	74
Figure 3.9	Pressure distribution around the building (a) pressure on a cross section passing the high rise section of the building (b) pressure on the front façade of the building (c) pressure on the back walls of the building.....	75
Figure 3.10	The contours of instantaneous velocity magnitudes along two planes crossing the CoE building.....	77
Figure 3.11	The injection plane upstream the model of the CoE Building, the local deposition rate of particles on 8 positions on the walls of the building is calculated.....	78
Figure 3.12	12 local deposition rate of particles on (1) the ground far from the CoE building, (2) the ground close to the building (3) the roof in low-rise section (4) the roof in high-rise section (5) the back wall of the low-rise section (6) the back wall of the high rise section (7) the front wall of the low-rise section (8) the front wall of the high-rise section.....	80
Figure 3.13	The subgrid scale turbulent kinetic energy modeled in LES.....	81
Figure 4.1	Experimental setup of Chen and Hopke (2009 a) with the stainless steel chamber.....	88
Figure 4.2	Time series of SOA number concentration, volume concentration, mass concentration and ozone concentration in the experiment of Chen and Hopke (2009a).....	89
Figure 4.3	Comparison of numerical solution of particle Brownian coagulations with the analytical solution of Park et al. (1999) for three time intervals.....	100
Figure 4.4	Time evolution of particles concentration distribution due to coagulation, nucleation and surface growth.....	102
Figure 4.5	Comparison of the predicted particles concentration distribution with the experimental data of Chen and Hopke (2009a) at $t = 7$ h....	103
Figure 4.6	The time evolution of the moments of the particle concentration distribution.....	104
Figure 4.7	The 2D geometry of the office model, with two ventilation systems. In case (I), the air outlet is located at the ceiling. In Case (II), the air	

	outlet is located on the floor.....	105
Figure 4.8	Contours of velocity magnitude, [m/s], for ventilation systems (a) type (I) and (b) type (II).....	107
Figure 4.9	Pressure contours, [Pa], for ventilation systems (a) type (I) and (b) type (II).....	107
Figure 4.10	Contours of M0, total number of particles [#], at time intervals, (a) 500 s, (b) 1000 s and (c) 1500 s for ventilation systems (I) and (II)..	108
Figure 4.11	The time evolution of the moments of concentration distribution at a point close to the mouth of the manikin for ventilation system (I)..	109
Figure 4.12	Comparison of the total number concentration (M0) and the total mass concentration (M1) of particulate pollutants at the manikin's breathing zone.....	110

CHAPTER I. Introduction

The quality of the air we breathe inside buildings depends on the concentration of the air pollutants taken from outside buildings through walls and windows cracks, and from the inlet of the air handling systems on one hand, and the formation of air pollutants from indoor recourses on the other hand.

The indoor exposure to outdoor PM plumes was investigated by Qian et al. (2014). They showed that the air pressure and the concentration distribution of the particulate pollutants over the buildings indicate the rate of the pollution taken. Therefore, a precise study on the airflow and particle transport and deposition over a bluff body with complex geometry was needed to be conducted.

The reaction of some materials used for different applications inside building, like furniture, paints and cleaners, with ozone is a major source of indoor air pollution. A number of models have been developed to predict the formation of these aerosols, but very few validation and application studies have been conducted. The population density of these aerosols was needed to be modeled and coupled with the air ventilation in the room.

1.1 Outdoor air pollution

1.1.1 Air flow around wall mounted square cylinder

The turbulent flow over a square cylinder as a bluff body with simple geometry has been of interest in a number of studies, due to its application in validating the numerical

models. Flow field over a wall-mounted cube in a channel is characterized by the following elements; a dominating horseshoe vortex that initiates at the front face of the cylinder; the arc shaped vortex in the wake of the cube; the separation at the top and the side faces; and the vortex shedding downstream the cube. The schematics of the flow characteristics around a square cylinder are shown in Figure 1.1 and Figure 1.2.

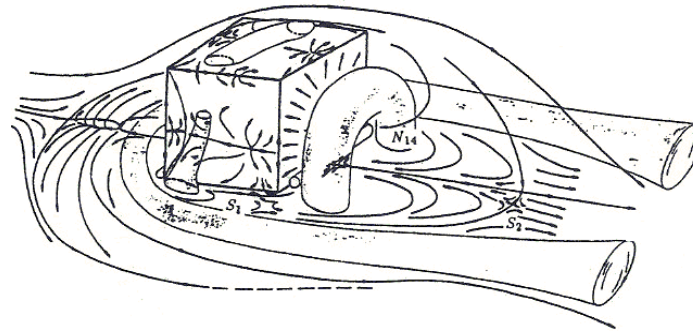


Figure 1.1 The horse shoe flow over a square cylinder (Martinuzzi and Tropea 1993).

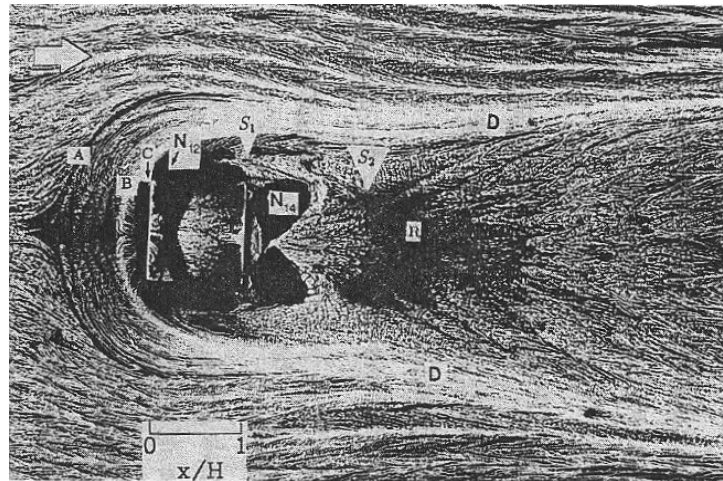


Figure 1.2 The oil-film visualization of the surface flow patterns for the flow around the square cylinder (Hussein and Martinuzzi 1996).

In Figure 1.2 the oil-film visualization of the flow patterns around the square cylinder, as obtained by Hussein and Martinuzzi (1996), are presented. Line A corresponds to the primary upstream separation line, line B determines the time averaged horseshoe center in front of the cube, line C specifies the secondary recirculation at the front base of the

cube, line D represents the location of the time averaged horseshoe vortex extensions downstream the cube, N14 identifies the concentrated recirculation region downstream the trailing edge of the cube, line N12 points to the separation line at the tip of the front edge, R indicates the reattachment zone downstream of the cube, and S1 and S2 are the saddle points.

Martinuzzi and Tropea (1993) reported their experiment results for the three dimensional flow around the surface mounted cube in the channel flow. Nakamura et al. (2001) experimentally investigated the flow field and the local heat transfer for the same geometry. They generated a turbulent boundary layer with the thickness in range of 1.5 to 1.8 times the cube height, H , by mounting a circular cylinder of diameter $\frac{1}{3}H$ at the distance of $16H$ in front of the cube. Wong et al. (1995) studied the flow passing over two square cylinders with different sizes, and measured the exerted aerodynamic forces. Calluaud et al. (2005) studied the vortex shedding dynamics of laminar flow over a wall mounted square cylinder, using Particle Image Velocity (PIV) technique. The experimental investigations performed by Calluaud et al. (2005), Castro and Robins (1977), Castro and Dianat (1983) and Hunt et al. (1978) showed that the flow characteristics depend on the turbulence intensity upstream of the cube as well as the cube dimensions.

In addition to the experimental studies, a variety of numerical models including Reynolds Averaged Navier-Stokes (RANS) models, Large Eddy Simulation (LES) and Direct Numerical Simulation (DNS) were used to simulate the flow field around bluff bodies. Iaccarino et al. (2003) used the unsteady two-layer $k-\varepsilon$ turbulence model proposed by

Durbin (1995), and showed that the application of unsteady model is critical in predicting the periodic vortex shedding, because the flow is not statistically stationary. Rodi (1997 a, b) compared the suitability of the $k-\epsilon$ model, the Reynolds stress-transport model (RSTM) and the LES model for predicting flows around square cylinders. They concluded that the $k-\epsilon$ model was not able to predict the mean flow of the periodic motion with reasonable accuracy. While the RSTM gave better results in comparison with the $k-\epsilon$ model, it still underpredicted the level of the turbulent fluctuations. The LES model, however, worked better in capturing the velocity fluctuations, but it was much more time consuming than RSTM. Cheng et al. (2003) compared the flow field around a matrix of cubes in a channel using the LES and the $k-\epsilon$ turbulence models at a low Reynolds number of 3800. They showed both models were able to predict the mean characteristics of the flow. However, the LES model predicted the spanwise mean velocity and Reynolds stresses better than the RANS model. Ochoa and Fueyo (2004) and Wong et al. (1995) used the LES model to simulate the flow of water over a square cylinder at Reynolds number of 21400. They compared their model prediction with that of the $k-\epsilon$ turbulence model and the experimental data. The LES model of the turbulent flow around a cubic cylinder, with Reynolds number of 40000, was carried out by Shah and Ferziger (1997). Fröhlich and Rodi (2004) simulated the flow around a circular cylinder at the Reynolds number of 43000 using LES with a variety of subgrid scale models. In particular, they compared the predicted mean velocity and stresses obtained with the Smagorinsky and dynamic Sub-Grid Scale (SGS) models with the experimental data. They reported that, when the grids in the computational domain are coarse, the Smagorinsky subgrid scale model is more accurate than the dynamic model. Yakhot et al.

(2006) simulated the flow field over a wall mounted cube using DNS method for the Reynolds number of 5610. They found that the unsteadiness due to the unstable interaction of the flow upstream and at sides of the cube generated the vortex shedding downstream the cube. Also, they argued that the inaccuracy of some of the RANS and LES turbulence models was because of their inability to predict the negative turbulence production in front of the cube, which was the source of the horseshoe vortex.

All in all, modeling turbulent flows using the LES leads to more accurate predictions of the turbulent fluctuations compared with the RANS-based turbulence models. However, the accuracy of the LES models strongly depends on the nature of the flow simulated as well as the grid sizes generated in the computational domain.

1.1.2 Wind flow around a building with a complex geometry

As part of this thesis, a study was conducted to simulate the airflow field around a building with complex configuration using RSTM and LES turbulence models. Baetke et al. (1990) simulated the wind flow in two different orientations over the surface mounted obstacles with different shapes using the k- ϵ and LES models. They found that in critical flow regimes the LES, although computationally more expensive, was more accurate and was more consistent with the experimental data compared to the k- ϵ model. Ferziger (1990) compared the RANS models with the LES for predicting the wind over a three dimensional obstacle. They found that the LES gave more accurate results. Stathopoulos and Zhou (1993) predicted the wind pressure on the surface of the buildings with different shapes using the k- ϵ turbulence model. Turkiyyah et al. (1995) used random vortex method which was based on the Lagrangian particle-based numerical simulation

scheme, to simulate the flow around a two dimensional bluff body. Hoxey and Richards (1993) simulated the flow and pressure fields around a full-scale building.

Tutar and Oguz (2002) compared the accuracy of the Re-Normalization Group (RNG) subgrid scale model, Smagorinsky-Lilly sub-grid scale LES model and a group of $k-\varepsilon$ turbulence models with the experiments performed by Murakami et al. (1990) for the flow around a cubical building at Reynolds number of 7×10^4 . They showed that the RNG subgrid scale model predicted the atmospheric flow fields in simple geometries reasonably well. However, this turbulence model lost its accuracy for more complex configuration. Lien and Yee (2004) modeled the flow over an array of buildings using the $k-\varepsilon$ and the Kato-Launder $k-\varepsilon$ turbulence models and compared the turbulent stresses with the experimental data. The greatest mean flow discrepancies between the turbulence models and the experimental data were found at the downstream of the array. Moreover, the turbulence quantities were about 50% underestimated. So they concluded that for more accurate numerical predictions, especially for the turbulence characteristics of the flow, more sophisticated turbulence models should be used.

Van Hooff and Blocken (2010) modeled the wind flow and natural ventilation for the Amsterdam Arena stadium. The physical domain contained the length scales between 0.02 m for the ventilation openings to 2900 m for the urban environment around the stadium. The high resolution body-fitted grids were simultaneously generated by using a series of, named, extrusion operations.

The accuracy of RSTM and LES simulations of the flow around the Center of Excellence (CoE) Building were assessed by comparing with the PIV (particle image velocimetry)

measurements performed by Kehs et al. (2009). The numerical model and the wind tunnel experiment of the wind flow around the CoE Building were a 1:192 scale of the physical model of the building. Two flow orientations were studied which were the typical wind directions from north to south and west to east of the building. The location of the building is shown in Figure 1.3.



Figure 1.3 Location of the CoE building on the map.

1.1.3 Particle transport in the turbulent flow

After evaluation of turbulence models, the transport and deposition of the particles in the turbulent flow of a square channel were studied. The Direct Numerical Simulation (DNS) of the flow, at a low Reynolds number, in a vertical channel was carried out by McLaughlin (1989). He found that the shear-induced lift force has significant effects on particle accumulation and deposition in the viscous sub-layer. Higson et al. (1994) and Mirzai et al. (1994) performed wind tunnel experiments concerning dispersion of gaseous

pollutants around an isolated building. Wood (1981), Hinds (1982), Li and Ahmadi (1992), Li and Ahmadi (1993), Li et al. (1994) and Liu and Ahmadi (2006) studied the turbulent airflows and deposition of particles emitted from a point source in a duct with and without obstructions. Direct numerical simulation of particle transport and deposition in turbulent duct flows are studied by Ounis et al. (1991), Zhang and Ahmadi (2000) and Zhang et al. (2001). Tian and Ahmadi (2007) studied the effect of different boundary conditions close to the wall on particle deposition rate. The effect of turbulent fluctuations on the particle dispersion and deposition was included using the discrete random walk (DRW) and the continuous filter white noise (CFWN) models. The accuracy of the standard wall function and the two layer zonal models in predicting the flow field near the wall was discussed. They concluded that the Reynolds stress model with two layer boundary condition was more accurate than the k- ϵ turbulence model. The corrections for the near wall quadratic variation of the turbulent normal fluctuations were critical for correct evaluation of the particle deposition velocity in the channel flow.

Brzoska et al. (1997) studied the fraction of the pollution concentration captured in the recirculation zone of a cubical building using a 2D finite element computational model and the k- ϵ turbulence model. The pollution was released with different velocities in the recirculation zone at the back of the building. When the emission velocity of the pollutant plume was high, smaller fraction of the pollutants was captured in the recirculation zone. Chi et al. (1996) modeled the air quality in a street canyon using a 2D Monte Carlo scheme of the particle distribution. Pollutant dispersion in urban street canyons was analyzed by Baik and Kim (1999) and Xia and YC Leung (2001). Ahmadi and Li (2000) reported their computer simulations of particle transport and deposition near a small

isolated building. Chang and Meroney (2001) modeled the flow passing an array of buildings using the RNG k- ϵ turbulence model, in FLUENT code, and found reasonable results compared with the wind tunnel experimental data. Gidhagen et al. (2003) modeled the airflow in a wind tunnel using the RNG k- ϵ turbulence model and predicted the concentration of ultrafine particles. Zhu and Hinds (2005) presented a model to predict the particle number concentration near a highway qualitatively based on the number particles emitted from the traffic, the wind and the location. Nazridoust and Ahmadi (2006) studied the effect of wind speed on particle dispersion and deposition in a 2D model of a street canyon using the Reynolds stress-transport model (RSTM). Hefny and Ooka (2009) studied the effect of the geometry of the computational cells on the accuracy of the analyzing the pollutant dispersion around the buildings.

The subgrid scale modeling of the particulate phase

LES turbulence model is able to predict the detail features of the turbulent flow which play an important role in particles dispersion and deposition. Thus, to consider the effect of small scale fluctuations on particle transport, a number of sub-grid scale (SGS) models have been developed. Armenio et al. (1999) investigated the effect of the subgrid scale (SGS) turbulent fluctuations on the particle motion by comparing the LES and the Direct Numerical Simulation (DNS) results for Reynolds number of $Re_\tau = 175$. They concluded that at low Reynolds numbers, the subgrid scale turbulent fluctuations did not affect the distribution of particles with high inertia. When the filter width increased, as a consequence of large grid sizes, the LES model, however, lost its accuracy of tracking low-inertia particles. They suggested that the SGS fluctuations close to the boundaries are the important factors affecting the particle deposition rate. Also, comparing Smagorinsky

SGS model with dynamic SGS model in a computational domain with reasonably fine grids showed that the latter is more accurate in predicting particle distribution.

Fan and Ahmadi (1993) and Shams et al. (2000) developed the sublayer model for particle deposition, which is based on the coherent vortical structure of the near wall turbulent flows. Li et al. (1994) simulated the mean velocity of a complex turbulent flow using thermodynamically consistent rate-dependent algebraic stress model. The turbulent fluctuations were modeled as a continuous Gaussian random field using the Kraichnan (1970) model. Smirnov et al. (2001) also used the Kraichnan (1970) model to reconstruct the turbulent fluctuations from LES and RANS velocity fields. The model satisfied the continuity and anisotropy of the flow, but did not satisfy the momentum equations.

Shotorban and Mashayek (2005) used LES to model a particle-laden homogenous turbulent shear flow. The mean velocity was captured by the LES using the Gaussian filter, and the instantaneous subgrid scale velocity was modeled by the deconvolution of the mean velocity and the inverse filter kernel, as the truncated Van Cittert series expansion. The deconvolution approximation for the SGS velocity was evaluated by comparing the DNS results with the LES flow predictions, with and without considering the SGS model for the particles distribution. The particles under study had large time constants. They concluded that the residual velocities, which were not solved in LES, could affect the particle dispersion and deposition especially in wall bounded flows. Winkler et al. (2006) modeled the turbulent flow in a square duct using LES and studied the effects of secondary flows, subgrid turbulent fluctuations, one way, two way and four way coupling approaches on particle deposition in the duct. They showed that for volume

fractions less than 10^{-4} the interaction of particles with themselves and with the flow is negligible and one way coupling approach would be sufficient.

Langevin stochastic model is applied by Pozorski and Apte (2009) to reconstruct the SGS turbulent velocities. In Langevin equation model the time scale, δT_{LP} , representing the interaction time between the particle and the SGS eddies, depends on the particle's Stokes number and the LES filter width, which is modeled either by Lagrangian time scale of the fluid (Shotorban and Mashayek 2005; Pozorski and Apte 2009) or by a time scale, based on the length scale of the geometry and the selected velocity of the whole flow field (Berrouk et al. 2007). Jin et al. (2010) represented an empirical closure model for the inertial particle-SGS eddy interaction timescale, δT_{LP} , versus the particle Stokes number and the filter width to improve the prediction of the particles dispersion. Gobert and Manhart (2011) interpolated the velocity field, predicted by LES on the Eulerian grid, on the particle positions in order to model the velocity seen by the particles. The modeled subgrid velocity was the combination of the Lagrangian base functions, as the interpolation kernels, and the Eulerian frame velocities. Therefore, a spectrum of the fluid velocity was transferred to the particles positions using Fourier transform. They named their model spectrally optimized interpolation (SOI). This model conserved the first and second moments of the particle distributions while the approximate deconvolution method (Shotorban and Mashayek 2005), as a SGS model was not able to predict that. However, in high Reynolds numbers or for small Stokes numbers ($St < 1$) SOI was not as accurate as the LES with no SGS model effecting on particles.

1.2 The secondary organic aerosols (SOAs) pollution in indoor air

According to U.S. Environmental Protection Agency (1995) the concentration of indoor air pollution can be two to five times greater than that of outdoor especially during the summer time. Many materials used in interior furniture emit terpenes which react with ozone in the air and produce nonvolatile aerosols. In addition, air fresheners, paints and cleaning products in residential buildings, printers and copiers are also major sources of emission of chemicals that react with ozone in indoor environments (Weschler 2000; Lee et al. 2001; Sarwar et al. 2003; Nazaroff and Weschler 2004; Singer et al. 2006; Toftum et al. 2008; Weschler 2009). The Reactive Oxygen Species (ROSs) in the air, for instance peroxides, are highly threatening to human health (Chen and Hopke 2009b). The reaction of terpenes with ozone produces aldehydes and carboxylic acids, which are semi-volatile organic compounds, and eventually leads to particle nuclei and surface growth (Chen and Hopke 2009a; Fan et al. 2003). The particulate matter generated from this process is referred to as the Secondary Organic Aerosol (SOA).

Keywords: Smocholovski Method, Classes Method, Methods of Moments

1.2.1 The numerical model of nucleation, coagulation and surface growth of SOAs in a dynamic mixing chamber

Population Balance Equations (PBEs) represent the property distribution of particles due to their coagulation, nucleation and surface growth. PBEs are highly non-linear, and several numerical and analytical methods were proposed to solve these equations, depending on the problem under study.

The Classes Methods (CMs) are one approach to overcome the issue of solving the nonlinear PBEs of particles. In CMs the particles are classified by a number of size bins and the PBEs are discretized based on those classes. The particle size distribution (PSD) can be classified by the fixed bins (Kumar and Ramkrishna 1996a) and adaptive size bins (Kumar and Ramkrishna 1996b). If the PSD was discretized linearly, each class would be the product of its number, i , and the volume of the smallest particles, ($v_i = i \times v_0$). However, the discretized particle sizes should be very fine for an accurate model, which is computationally expensive (Hidy 1965). Batterham et al. (1981) assumed that the new particles are generated from collision of two equal size particles ($v_i = 2v_{i-1}$). Yet, this method missed the conservation of moments of particles. Hounslow et al. (1988) modified the model presented by Batterham et al. (1981) by extending the size ranges of particle collisions. They considered the particles births and deaths of a specific size, respectively, due to the coagulations of smaller particles and breakages of larger ones. In this model, the conservation of the zeroth moment of particles was satisfied. Lister et al. (1995) used an adjustable PSD discretization to optimize the simulation of the particles growth and aggregation.

The mean particles concentration distribution function was presented by Bleck (1970), Gelbard and Seinfeld (1979) and Nambiar et al. (1992) as $\overline{n_i(t)} = \frac{1}{v_{i+1} - v_i} \int_{v_i}^{v_{i+1}} n(v, t) dv$, to simplify the PBEs. But, this method could only satisfy the particles mass conservation. Also, because of the double integrating over the number concentration density and the particle collision frequency in PBEs, this approach was computationally time consuming.

Alexopoulos and Kiparissides (2005) studied the simultaneous particle nucleation, growth and aggregation using orthogonal collocation on finite elements as an approximation of the number density function of the particles' concentration. Rigopoulos (2007) used probability density functions (PDF) to solve the PBEs combined with the flow field in a turbulent reactive flow. He used the Monte-Carlo methods to solve the PDF equations.

Discretized population balance equations (DPBEs) as well as Monte-Carlo methods were computationally rather expensive, in terms of time and computer capacity. Therefore, in order to reduce the computation expenses instead of the actual size distribution functions, the moment distributions of particles were simulated by Lee and Chen (1984), Williams (1986), Frenklach and Harris (1987), Otto et al. (1993), Barrett and Jheeta (1996), Lee et al. (1997), Markutsya et al. (2008) and Liu and Lin (2008).

The moment equations of the particle distribution were obtained by integrating the appropriate properties of the particle, including radius, volume or mass of the particle, over the PBEs. The Method of Moments (MOMs) was computationally more time efficient rather than the Classes Methods (CMs) because it did not need to consider a vast number of discretized equations to capture a reasonable concentration distribution of particles. Hulburt and Katz (1964) were the first to use the method of moments (MOM) to reduce the order of PBEs. Marchisio and Fox (2005), Markutsya et al. (2008) and McGraw (1997) used the Quadratic Method of Moments (QMOM) to capture the moments from integration over concentration density functions. Unlike the discretized population balance equations (DPBEs), the MOM was well-mannered in conjunction

with the CFD simulations. Wang and Fox (2003) prepared an algorithm to study a reactive precipitation, including mixing-limited reaction, nucleation, growth, and aggregation by implementing QMOM.

However, it was not possible to predict the number concentration of particles directly from the moment property of particles. Therefore, in literature several concentration distribution functions were assumed as closure models for the moment equations. For instance, Brock and Oates (1987); Kiełkiewicz (1994); Lee (1983); Pratsinis (1988) and Williams (1986) used the lognormal function, Hulburt and Katz (1964) used γ distribution function and Frenklach (2002) assumed particles were distributed through a polynomial function. Baldyga and Orciuch (1999) proposed the PSD closure model which was based on Pope's (1979) study. Diemer and Olson (2002) used polynomial interpolation closure model, and evaluated the accuracy of the MOM. Also, they proposed basis sets to reconstruct the PSDs from the moments. Friedlander (1977), Frenklach and Harris (1987) and Frenklach (2002) used interpolative closure of moments instead of predicting the PSD function a priori. Barrett and Jheeta (1996), used the polynomial closure functions of the moments with different orders, and showed that the second order polynomial function of the moments was equivalent to the lognormal function of PSD, which accurately predicted the moment distributions. Bandyopadhyay et al. (2005) and Abramov (2007) used Maximum Entropy Method (MEM) to reconstruct the PSD from the moments. MEM states that the probability distribution that maximizes the information entropy is the one that is statistically most likely to happen. However, Kass and Wasserman (1996) and Scales and Tenorio (2001) showed that the accuracy of

MEM strongly depends on the number of prior moments applied which is limited for an experimental measurement.

The lognormal function was more practical in terms of computational time and accuracy than other closure functions, and it has been used in several studies. Bensberg et al. (1999) assumed a lognormal PSD as a closure of the moment method, and simulated the formation of silicon nitride from the confined coflow diffusion flame of SiCl_4 and NH_3 in a wall-heated flow. Pratsinis (1988), Jain et al. (1997) and Jain and Kodas (1998) used the lognormal PSD to study the aggregation and growth of nano-particles. Wright (2000) studied the optical properties of the aerosols experimentally, and showed that the particle concentrations were distributed following the lognormal function of their sizes. Lee (1983) proposed an analytical solution of PBEs based on log normal PSD for particles' Brownian coagulation with two different collision frequencies and modified the Smoluchowski (1917) model.

Otto et al. (1993) and Otto et al. (1994) used moment method with lognormal PSD function to study the Brownian coagulation of particles in transition regime. Lee et al. (1997) studied the coagulation of particles in the free molecular regime by using the lognormal closure function of PSD and presented an analytical solution of MOM. They showed that the PSD reaches steady state condition after a certain time.

MOM was used to simulate the practical applications including crystallization, polymerization, as well as soot formation and distribution in conjunction with the flow field. Wu and Menon (2001) coupled the MOM with the linear eddy model of plum turbulent flow, and studied the particle nucleation and coagulation. Liu and Lin (2008)

studied the particle collision in a two dimensional Poiseuille flow field using MOM with lognormal closure.

Park et al. (1999), divided the particle size range into three regimes in terms of the Knudson number, Kn , and represented an analytical solution of the particles Brownian coagulation. The Knudson number is defined as the ratio of the air mean free path, at temperature T , to the particle's radius, $Kn = \frac{\lambda}{r_d}$. Ultra-fine particles are found in free molecular regime with $Kn > 50$, where particles are much smaller than the air mean free path, and their Brownian motion is the dominant distribution mechanism. Coarse particles are included in continuum regime with $Kn < 1$, where the particle sizes are large enough to follow the main flow field. In between is the transition regime with $1 < Kn < 50$. They assumed lognormal size distribution, and used the harmonic mean of the collision frequency function over the entire particle size range.

1.2.2 Effect of indoor air ventilation on particulate pollutant concentration distribution, including nucleation, coagulation and surface growth

People in average spend more than 70% of their time at indoor environments (Robinson et al. 1991 and Kim et al. 2001), which indicates the importance of studying the indoor air quality. The particles inside buildings are more bioactive than the outdoor particles (Long et al. 2001). Also, a high fraction of the indoor air pollutants are ultra-fine particles (Santanam et al. 1990). Long et al. (2000), Rohr et al. (2003) and Weschler and Shields (2003) showed that the reaction of ozone with terpenes was the main source of the indoor air pollutants, which produced ultra-fine particles. Singer et al. (2006) measured the concentration of the SOAs in a model of residential room, and presented a mathematical

model, considering the effect of ozone concentration in indoor air pollution. Several experimental investigations in production of Secondary Organic Aerosols (SOAs) at ventilation ducts (Fick et al. 2005), room size stainless steel chambers (Fan et al. 2003; Sarwar et al. 2003), unoccupied offices (Weschler and Shields 2003) and residences (Long et al. 2000; Hubbard et al. 2005) are conducted. Chen and Hopke (2009a) studied the formation of SOAs due to the reaction of α -pinene and ozone in a dynamic chamber system, wherein the conditions of the ventilated indoor environment were provided.

1.3 Objectives

The general goal of this thesis is to develop a computational model for analyzing particles transport and deposition in turbulent flows over obstacles with complex geometries. Such a reliable computational model would help to understand the dispersion patterns of air pollution in urban areas. The specific objectives are:

1. The accuracy of the RSTM and LES turbulence models in predicting detail features of the transient flow field over a 3D obstacle with complex configuration should be evaluated.
2. A particle transport model should be developed to consider the effect of instantaneous velocity fluctuations on particles dissipation and deposition.
3. The evaluated models provided in previous steps are to be applied to predict the concentration distribution of the particulate pollutants around the CoE Building, which is located in intersection of two major highways.

In addition, the population density of indoor air pollutions is to be addressed in the second part of the thesis. A numerical model should be developed to predict the size-

concentration distribution of secondary organic aerosols (SOAs) which are a major component of the pollutants in indoor environments. Therefore,

1. The population balance equation should be solved using method of moments (MOM) to model the SOAs size and concentration distribution over time, considering the nucleation, Brownian coagulation and surface growth.
2. The numerical model is to be applied in evaluating the efficiency of two mixed-mode ventilation systems in removing the indoor air pollution from an office model.

CHAPTER II. Computational model of airflow around an obstacle with complex geometry

Abstract

The air flow field around a wall mounted square cylinder was numerically modeled and the simulation results were compared with the experimental data. The airflow field was simulated using Reynolds Averaged Navier-Stokes (RANS) models as well as Large Eddy Simulation (LES). Particular attention was given to the case with Reynolds number of 80,000 for which the experimental data of Hussein and Martinuzzi (1996) were available. The nature of the 3D wakes behind the cube as well as the vortices in front and at the back of the cube were analyzed. The simulation results were compared with the experimental data and the accuracy of different models were investigated. It was shown that LES better captured the features of the separated flow, while it was computationally expensive. The Reynolds stress-transport model (RSTM), however, missed some features of the separated flow, but was comparatively more economical. The accuracy of the RSTM in predicting the turbulence features of separated flows was discussed, and its application for the flow around a realistic model of a building was pointed out.

The study of the wall mounted cube as a 3D simple geometry was conducted to verify the accuracy of the turbulence models for the more complex geometries of the Center of Excellence (CoE) Building. The Center of Excellence (CoE) Building was built in Syracuse NY at the intersection of two major highways. A picture of the CoE Building

and the nearby highways are shown in Figure 2.1. In this Chapter, the wind flow over the CoE Building model is studied.



Figure 2.1 Center of Excellence Building at the intersection of Interstate Highways 81 and 629 at Syracuse, NY.

The wind flow around the model of the CoE Building (from north to south and from west to east) was first simulated using RANS-RSTM model. Comparison of the numerical simulations with the wind tunnel experimental data showed that although RSTM pressure field on the walls of the building model consisted with the data measured by the pressure taps, some aspects of the airflow velocity profile were not as accurate. The complexity of the building's geometry and formation of separated flow regions caused the discrepancies between the RSTM model and experiment data. Therefore, LES turbulence model was applied to improve the predictions of the velocity field. The comparison of the numerical model with the PIV measurements approved that.

2.1 Computational domain and boundary conditions

2.1.1 Computational domain and boundary conditions of the air flow model around the wall mounted square cylinder

The geometry of the wall mounted cube in a wind tunnel was reconstructed, in GAMBIT software, based on the dimensions of the wind tunnel experiment of Hussein and Martinuzzi (1996). Figure shows the detail configuration of the wall mounted cube in the wind channel. In their experiment the cube height was $H = 25 \text{ mm}$ and the channel height was 50 mm , twice the height of the cube. The inlet and outlet of the channel were, respectively, at distances of $10H$ and $15H$ from the cube.

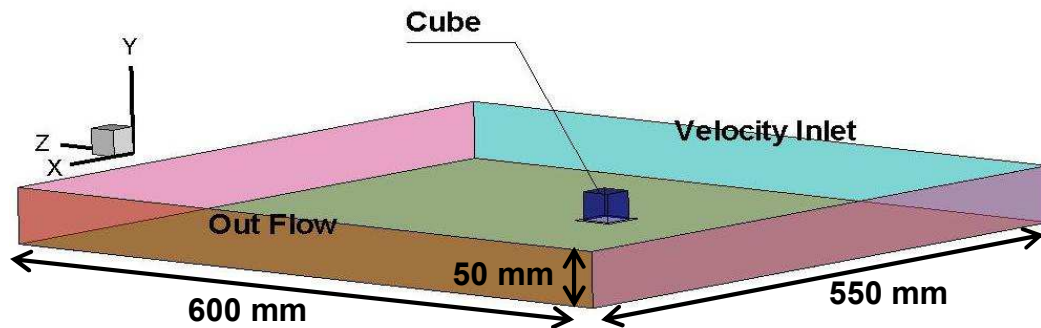
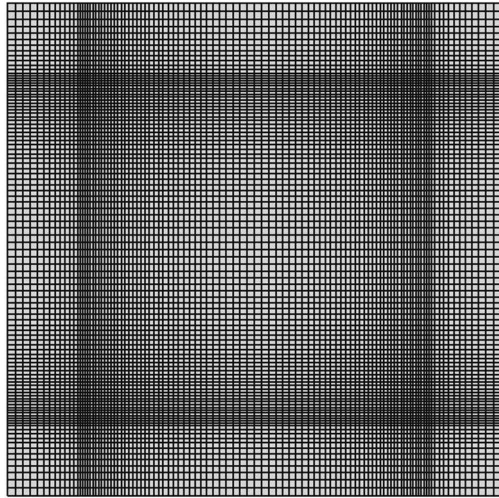


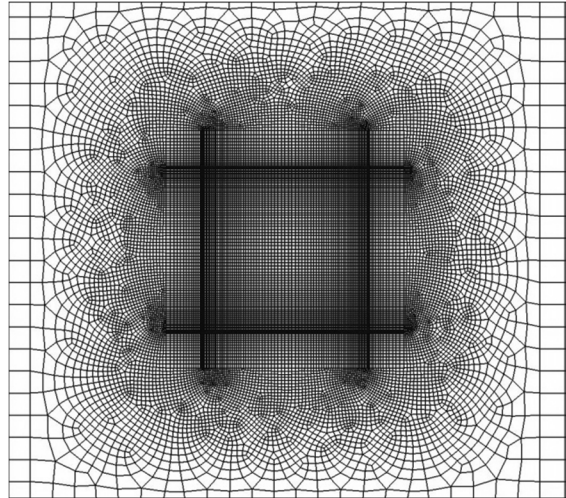
Figure 2.2 Computational domain of the wall mounted square cylinder in a channel flow. Cube dimension = $25 \times 25 \times 25 \text{ mm}^3$.

Three sets of meshes with 0.8×10^6 , 1.5×10^6 and 2.5×10^6 cells were used for mesh sensitivity analysis. The velocities predicted by the steady RSTM, at 8 different points near the top and back side of the cube were compared. The velocity magnitudes of the first two sets of meshes had 3% discrepancy in average, while the simulated variables did not have more than 1% difference on average for the 1.5×10^6 and 2.5×10^6 cell meshes. The selected mesh of 2.5×10^6 structured and unstructured cells that was generated in 4 blocks was used for analysis. Figure 3 shows sample cross sections of the grid in different locations. The attention was given to keep the cell size quite fine of about 0.15

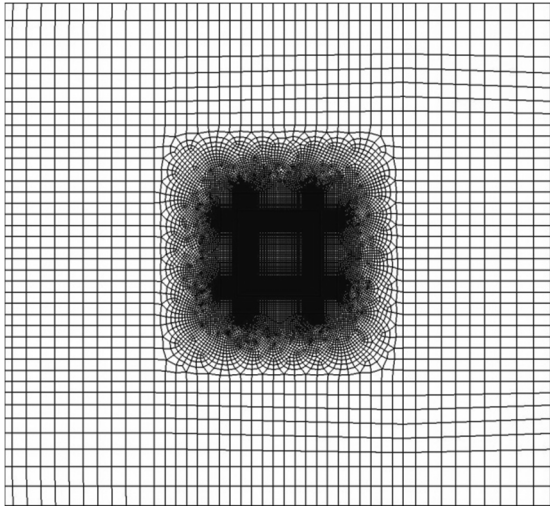
mm in the boundary layer around the cube, while the grid size was increased with the distance from the surface of the cube to 5.7 mm. The structured grid was generated where it was possible to reduce the number of nodes and the solution time consequently.



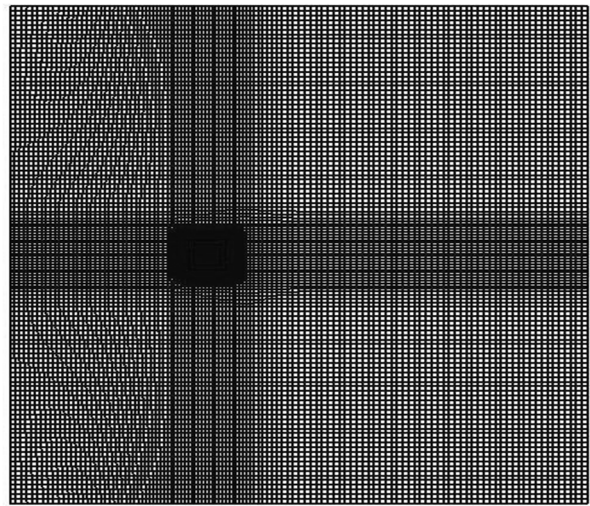
(a) Zoom in I. Grids at the boundary of the cube



(b) Zoom in II. Exchanging from fine to coarse grids through hexahedral grids



(c) Structured grid in the channel flow



(d) Fine structured grid close to the cylinder and coarse grid far from it

Figure 2.3 The plan view of the size distribution of grids in the numerical domain.

The numerical simulation was performed by using the commercial software FLUENT 12.1. The unsteady RSTM, developed by Launder, Reece and Rodi (Launder et al. 1975), with the time step of 0.001 s was used for simulating the airflow field. The velocity distribution at the channel inlet was considered to be uniform at 28.6 m/s, with 5%

turbulent intensity, which was based on the software recommendations, $I = 0.16Re^{-\frac{1}{8}}$.

The fully developed velocity profile was set as the outlet boundary condition. That is, the velocity normal to the main stream direction at the outlet was assumed to be zero.

The simulation result of the two equation k- ϵ turbulence model was used as the initial condition for the RSTM. The continuity and momentum (pressure linked) equations were solved by the SIMPLE algorithm. A 4 core, 12 GB RAM computer was used to perform these simulations.

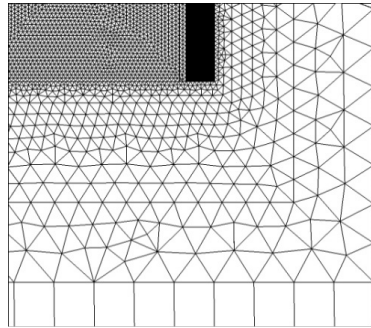
In addition to the RSTM, the LES with the subgrid scale model of Smagorinsky-Lilly (Smagorinsky 1963; Lilly 1992) was used in the analysis of airflow around the square cylinder. The time step in the LES model was 0.0001 s. The LES simulations were performed on a cluster of 6 parallel computers for 72 hr computation time. The time averaged results obtained from LES were compared with the RSTM results.

2.1.2 Computational domain and boundary condition of the model of the wind flow around the CoE Building

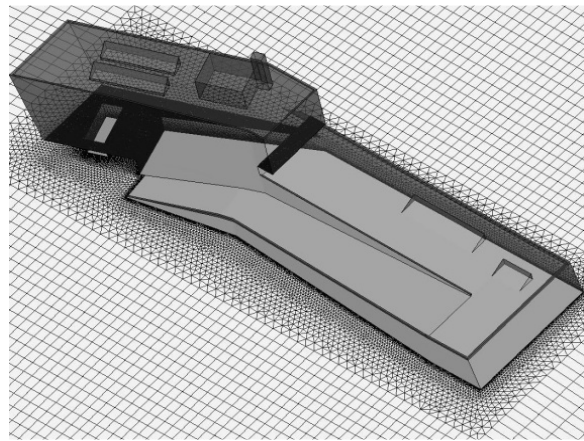
The Center of Excellence (CoE) Building is a large building located at the intersection of two major highways as shown in Figure 2.1. A 1:192 scale physical model of the CoE Building was fabricated using a stereo-lithography model and was tested in the wind tunnel by Kehs et al. (2009). The airflow around the building model was tested in the 3'×4' wind tunnel test section, where the flow field was fully developed. The maximum height of the model from floor to the top side of the chimney was 0.168 m.

A computational model based on the wind tunnel condition of Kehs et al (2009) was developed using GAMBIT software. In order to control the number of grids in the computational model, 8 mesh blocks with a combination of structured and unstructured

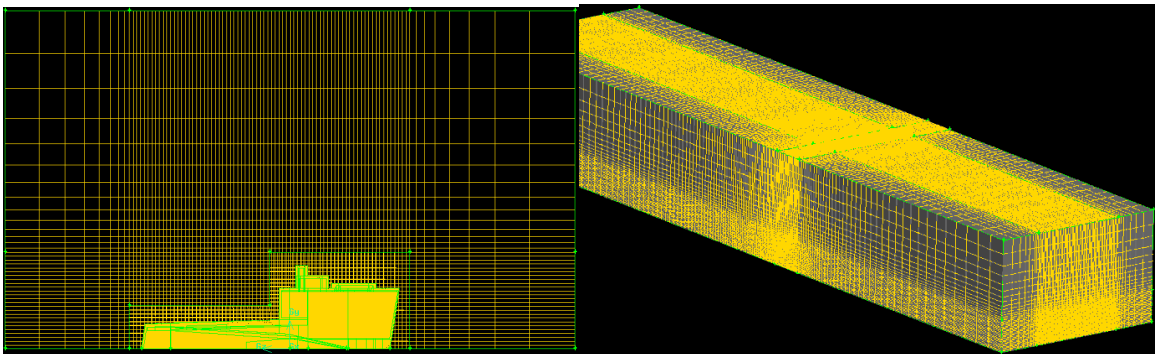
cells were generated. Fine mesh near the building surfaces and relatively coarse mesh far from the building were used. A sample grid is shown in Figure 2.4. A series of grid sensitivity studies with 0.9×10^6 , 1.86×10^6 and 2.2×10^6 grid cells were conducted using the LES turbulence model. Since LES is more sensitive to the grid sizes, the case study with 1.86×10^6 computational cells was considered for both the LES and the RSTM turbulence models.



(a) Grids at the boundary of the building (Zoom in)



(b) Combination of unstructured and structured grids at two blocks



(a) Structured grid in the channel flow

(b) Fine structured grid close to the building and coarse grid far from building

Figure 2.4 Computational grid for flow analysis around the CoE Building.

The numerical simulation was performed using the commercial software, Fluent 12.1. Three wind speeds of low, 5 m/s, moderate, 10 m/s, and high, 15 m/s, were simulated by

the RSTM for two different wind flow orientations toward the building, namely, from north to south and west to east. The corresponding Reynolds numbers for the range of wind speeds under study were respectively, 40600, 81200 and 121800 which are based on the height of the main part of the building model, $H_b = 0.1218$ m. In this section two examples with wind speeds of 10 m/s and 15 m/s from north to south are presented.

More details of the turbulent flow characteristics were studied by using the LES for modeling the wind flow from north to south of the CoE building with the velocity magnitude of 10 m/s. The LES results were compared with the corresponding RSTM predictions and discussed.

A uniform velocity with 10% turbulent intensity was assumed for the wind at the inlet boundary condition. The outlet was placed far downstream from the building model. The out flow boundary condition was imposed at the outlet. That is the axial derivative of the axial velocity is zero and the velocities perpendicular to the flow stream is zero.

Grid study

For a steady RANS-RSTM simulation of airflows around the model of the CoE Building, the quality of the generated grids is examined. Here the wind speed is 10 m/s from north to south of the CoE Building ($Re = 81,200$), and the number of grid cells is 1.86×10^6 . To evaluate the grid quality, the contours of first node from the wall in wall units on the surfaces of the building are evaluated and the results are presented in Figure 2.5. The wall unit is defined as $y^+ = yu^*/\nu$, where y is the distance of the first node from the wall boundary, u^* is the shear velocity which is $u^* = \sqrt{\frac{\tau}{\rho}}$, where τ is the wall shear.

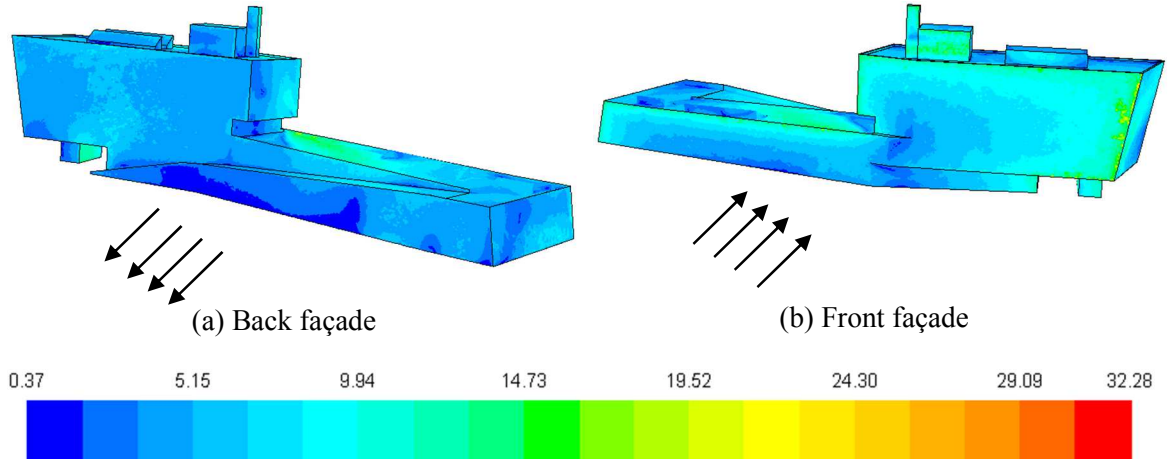


Figure 2.5 Contours of y^+ for the nearest grid point on the walls of the CoE building model for the wind speed of 10 m/s using the RANS-RSTM. (a) Contours of y^+ on the walls behind the building. (b) Contours of y^+ on the front walls facing the wind.

The contour of first grid node from the wall in wall units shows a rather fine grid distribution in the computational domain near the surface of the building. The maximum y^+ is about 30, the minimum is of the order of 0.5, and the area-weighted average y^+ is 6.08.

Also, since the same grid structure is used for the LES turbulence model, the area-averaged Kolmogorov length scale, η , and Taylor length scale, λ , are compared with the averaged distance of the first node from the walls and compared. The Kolmogorov length scale is calculated as $\eta = \left(\frac{\nu^3}{\varepsilon}\right)^{\frac{1}{4}}$ and the Taylor length scale is estimated as $\lambda = \left(\frac{10\nu k}{\varepsilon}\right)^{\frac{1}{2}}$ (Tennekes and Lumley, 1972), here ν , ε and k are, respectively, the kinematic viscosity, turbulent dissipation rate and turbulent kinetic energy. The averages are $\eta_{mean} = 0.0041$ mm, $\lambda_{mean} = 2.44$ mm and $y_0 = 0.3$ mm, where y_0 is the averaged distance of the first node from the walls. Therefore, $\eta_{mean} < y_0 < \lambda_{mean}$, and the grid size distribution is appropriate for the LES turbulence model as well.

To show the consistency of the computational domains for LES and RANS-RSTM, the contours of first grid in wall units as obtained from time-averaged LES simulation is presented in Figure 2.6. It is seen that for the LES, the values of y^+ for the first grid point is again in the range of 0.5 and 30. Here the area-weighted average y^+ is 8.5.

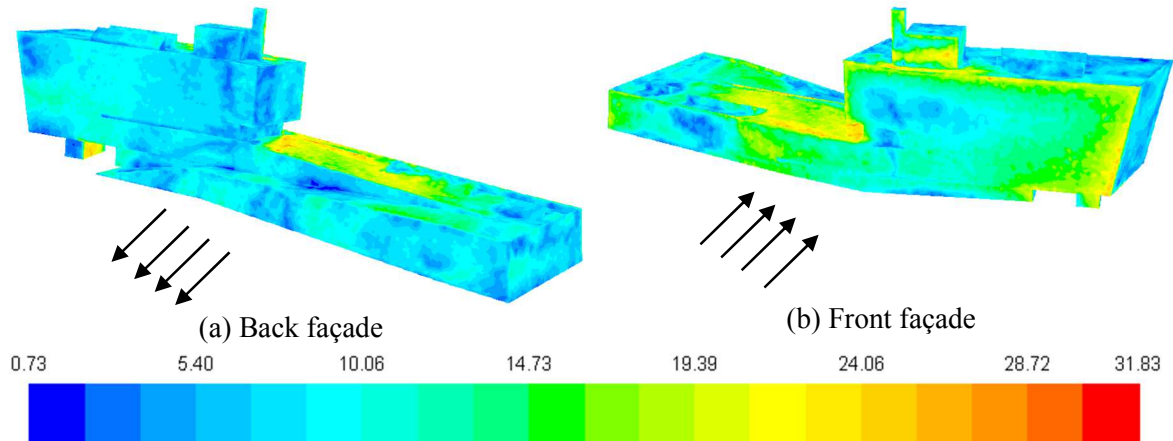


Figure 2.6 Contours of y^+ on the walls of the CoE building model for wind speed of 10 m/s using LES. (a) Contours of y^+ on the walls behind the building. (b) Contours of y^+ on the front walls facing the wind

The grid study presented here shows that the size of the cells near the walls of the CoE building is sufficiently refined and could capture the viscous sublayer and buffer layer in most of the region. Also, there is a consistency between the LES and RANS-RSTM turbulence models.

2.2 Governing equations

Reynolds Stress Transport Model (RSTM)

The incompressible, unsteady airflow around the models of the wall mounted square cylinder and the CoE Building was simulated using the Reynolds stress transport turbulence model. The ensemble averaged continuity and momentum equations are given as,

$$\frac{\partial \bar{u}_i}{\partial x_i} = 0 \quad (2.1)$$

$$\frac{\partial \bar{u}_i}{\partial t} + \bar{u}_j \frac{\partial \bar{u}_i}{\partial x_j} = -\frac{1}{\rho} \frac{\partial \bar{p}}{\partial x_i} + \frac{\partial}{\partial x_j} \left(\nu \frac{\partial \bar{u}_i}{\partial x_j} - \overline{u'_i u'_j} \right) \quad (2.2)$$

The Cartesian tensor notation is used throughout this chapter. The left hand side of the equation (2.2) is the convective transport of the averaged velocity. On the right-hand side,

$\frac{\partial \bar{p}}{\partial x_i}$ is the pressure gradient, $\nu \frac{\partial \bar{u}_i}{\partial x_j}$ is the viscous shear stress, ν is the fluid molecular

viscosity and $\overline{u'_i u'_j}$ is the Reynolds turbulence stress tensor. In order to simulate the

airflow the turbulence stresses need to be modeled. The stress transport model of

Launder, Reece and Rodi (1975) is given as,

$$\frac{\partial}{\partial t} (\overline{\rho u'_i u'_j}) + \bar{u}_k \frac{\partial}{\partial x_k} (\overline{\rho u'_i u'_j}) = d_{ij} + P_{ij} - \varepsilon_{ij} + \phi_{ij} \quad (2.3)$$

The terms on the right hand side of equation (2.3) are, respectively, diffusion, production, dissipation and pressure/strain terms, which are given as,

Diffusion

$$d_{ij} = c_s \frac{\partial}{\partial x_k} \left\{ \frac{k}{\varepsilon} \left[\overline{u'_i u'_l} \frac{\partial \overline{u'_j u'_k}}{\partial x_l} + \overline{u'_j u'_l} \frac{\partial \overline{u'_k u'_i}}{\partial x_l} + \overline{u'_k u'_l} \frac{\partial \overline{u'_i u'_j}}{\partial x_l} \right] \right\}$$

Production

$$P_{ij} = \overline{u'_j u'_k} \frac{\partial \bar{u}_i}{\partial x_k} + \overline{u'_i u'_k} \frac{\partial \bar{u}_j}{\partial x_k}$$

Dissipation

$$\varepsilon_{ij} = \frac{2}{3} \delta_{ij} \varepsilon$$

Pressure Strain

$$\phi_{ij} = c_1 \frac{\varepsilon}{k} \left(\overline{u_i' u_j'} - \frac{2}{3} \delta_{ij} k \right)$$

The transport equation for the turbulence energy dissipation is given as,

$$\left(\frac{\partial}{\partial t} + u_k \frac{\partial}{\partial x_k} \right) \varepsilon = c_\varepsilon \frac{\partial}{\partial x_k} \left(\frac{k}{\varepsilon} \overline{u_k' \varepsilon'} \frac{\partial \varepsilon}{\partial x_k} \right) - c_{\varepsilon 1} \frac{\varepsilon}{k} \overline{u_i' u_k'} \frac{\partial \overline{u_i}}{\partial x_k} - c_{\varepsilon 2} \frac{\varepsilon^2}{k} \quad (2.4)$$

where C_s are the constant coefficients and the terms on right hand side of the equation (2.4) are, respectively, diffusion, generation and destruction. The values of model constants may be found in Launder et al. (1975).

Large Eddy Simulation (LES)

The large eddy simulation was used to predict the details of the flow recirculation regions and reattachments on the top and at the back sides of the bluff bodies including the cylindrical block and the CoE Building in cross flows.

In LES model, the flow field velocity and pressure are decomposed to filtered values and sub-grid scale values Smagorinsky (1963). That is the filtered quantities are resolved (large eddies), \bar{f} , and the residual (subgrid scale) components, f' are not resolved. The large eddies are responsible for carrying most of the mass, momentum and energy, while the small eddies in Kolmogorov length scales dissipate the energy. The filtration is represented as,

$$\bar{f}(x_i, t) = \int f(y_i, t) G_{\Delta x}(x_i, y_i) dy_i; \quad f = \bar{f} + f' \quad (2.5)$$

where $G_{\Delta x}$ is a filter of width Δx . The filter function, $G_{\Delta x}$ is considered based on the cell volume, V ,

$$G_{\Delta x} = \begin{cases} 1/V & y_i \in V \\ 0 & y_i \text{ other wise} \end{cases} \quad (2.6)$$

The filtered Navier-Stokes equation for an incompressible flow is given as,

$$\frac{\partial}{\partial t}(\overline{u_i}) + \frac{\partial}{\partial x_j}(\overline{u_i u_j}) = -\frac{1}{\rho} \frac{\partial \overline{p}}{\partial x_i} + \frac{\partial}{\partial x_j}(\sigma_{ij}) - \frac{\partial}{\partial x_j}(\tau_{ij}) \quad (2.7)$$

where σ_{ij} is the stress tensor due to the molecular viscosity, given by

$$\sigma_{ij} = \nu \left(\frac{\partial \overline{u_i}}{\partial x_j} + \frac{\partial \overline{u_j}}{\partial x_i} \right) \quad (2.8)$$

Here, τ_{ij} is the subgrid-scale stress tensor defined as,

$$\tau_{ij} = \overline{u_i u_j} - \overline{u_i} \overline{u_j} \quad (2.9)$$

The subgrid-scale stress is modeled as

$$\tau_{ij} = 2\nu_t \overline{S_{ij}} \quad (2.10)$$

where the rate of strain tensor, $\overline{S_{ij}}$, is given as

$$\overline{S_{ij}} \equiv \frac{1}{2} \left(\frac{\partial \overline{u_i}}{\partial x_j} + \frac{\partial \overline{u_j}}{\partial x_i} \right) \quad (2.11)$$

and ν_t is the subgrid scale turbulent eddy viscosity. The Smagorinsky-Lilly (Smagorinsky 1963; Lilly 1992) subgrid scale turbulence viscosity was used for modeling the wind flow around the wall mounted square cylinder. For the more complex CoE Building model the Wall Adaptive Local Eddy viscosity model (WALE), provided by Nicoud and Ducros (1999), was used.

Smagorinsky-Lilly subgrid-scale model

Smagorinsky (1963) and Lilly (1992) proposed the following mixing length type expression for the subgrid scale turbulence viscosity. That is,

$$\nu_t = l_s^2 \sqrt{2S_{ij}S_{ij}} \quad (2.12)$$

where l_s is the mixing length for the subgrid scale, and is given by

$$l_s = \min(\kappa d, C_s \Delta) \quad (2.13)$$

κ is the von Kármán constant, d is the distance to the closest wall and C_s is the Smagorinsky constant and Δ is the local grid scale,

$$\Delta = V^{1/3} \quad (2.14)$$

where V is the grid volume.

Wall Adaptive Local Eddy-Viscosity (WALE) subgrid-scale model

The Wall Adaptive Local Eddy-Viscosity (WALE), developed by Nicoud and Ducros (1999), was used for the complex geometry of the building model. That is,

$$\nu_t = L_s^2 \frac{(S_{ij}^d S_{ij}^d)^{3/2}}{(\overline{S_{ij} S_{ij}})^{5/2} + (S_{ij}^d S_{ij}^d)^{5/4}} \quad (2.15)$$

where L_s and S_{ij}^d in the WALE model are,

$$L_s = \min(\kappa d, C_w V^{1/3}) \quad (2.16)$$

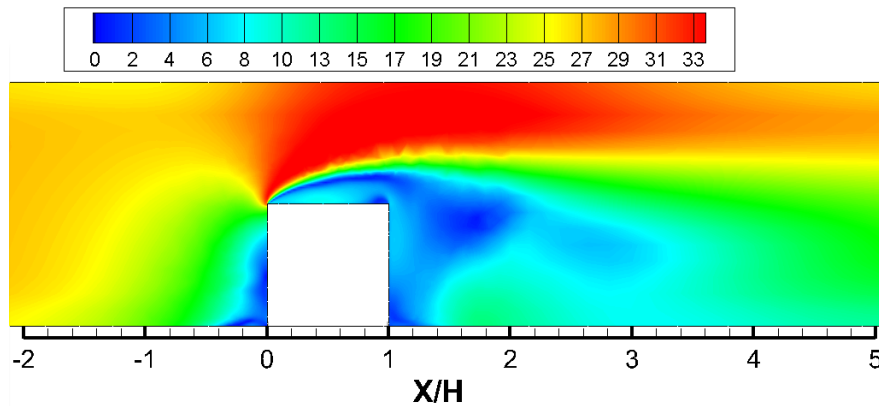
$$S_{ij}^d = \frac{1}{2} \left(\left(\frac{\partial \overline{u}_i}{\partial x_j} \right)^2 + \left(\frac{\partial \overline{u}_j}{\partial x_i} \right)^2 \right) - \frac{1}{3} \delta_{ij} \left(\frac{\partial \overline{u}_k}{\partial x_k} \right)^2 \quad (2.17)$$

where κ is the von Kármán constant, d is the distance to the closest wall and C_w is about 0.325. The WALE subgrid scale model leads to zero eddy viscosity in the vicinity of a wall; therefore, the dynamic adjustment or the damping function is not necessary in the numerical solution. These characteristics of the WALE subgrid scale model make it suitable for modeling the LES simulation of flow in complex geometry regions.

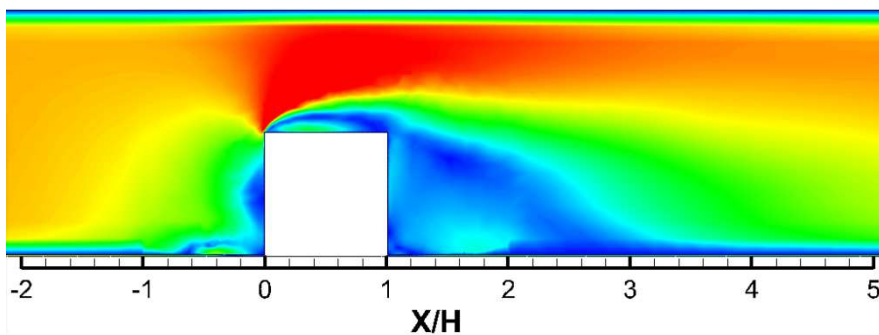
2.3 Results and discussion

2.3.1 Simulation of airflow around the wall mounted square cylinder

The numerical simulation of the airflow field around a surface mounted cube, with a half channel height, in a fully developed turbulent channel flow is presented in this section. The Reynolds number, based on the channel height and the bulk velocity, was set as 80,000, which was the same as the Reynolds number in the experiment performed by Hussein and Martinuzzi (1996). The cube was located 10H far from the channel inlet, so that the airflow was fully developed in front of the cube. Also, the channel length aft the cube was designed 15H long to capture the wake flow downstream of the cube.



(a) Time averaged velocity contours at plane $z/H = 0$ as predicted by the RSTM



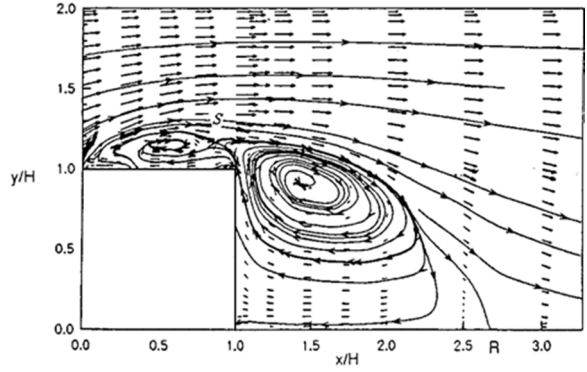
(b) Time averaged velocity contours at plane $z/H=0$ as predicted by the LES

Figure 2.7 The comparison of the velocity contours predicted by RSTM and LES.

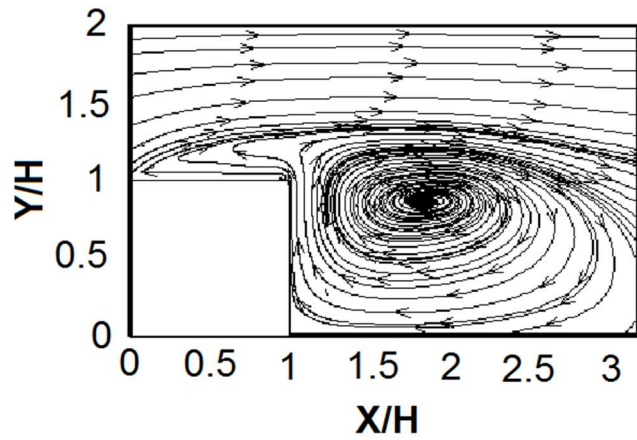
The unsteady Reynolds stress transport, as well as, the LES model was used to study the turbulent flow field around the block in the channel.

The velocity contours predicted by the RSTM and the LES model, around the wall mounted square obstacle, along the plane $z/H = 0$, are shown, in Figure 2.7. The contours represent the magnitude of the projection of the velocity on the plane parallel to the main airflow stream. The velocity field before reaching the front face of the cylinder (before $x/H = -2$) is fully developed. In the vicinity of the front and back sides of the block, recirculation zones are formed. At the front face of the obstacle ($x/H = 0$), the airflow separated from the leading edge and a recirculation region is formed at the top of the cylinder.

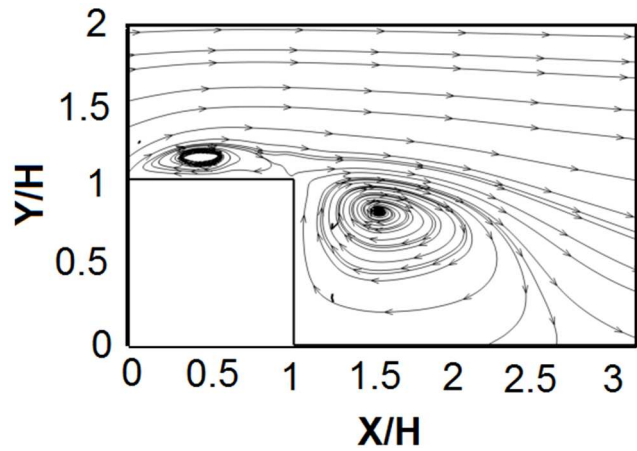
The streamlines close to the cylinder are magnified in Figure 2.8 and the details of the flow field simulated by the RSTM and the LES models are compared with the Laser-Doppler Velocimetry measurements performed by Hussein and Martinuzzi (1996). The flow separation from the leading edge of the cylinder is predicted by the three models. In RSTM the reattachment point at the back side of the obstacle is located at $x/H \approx 4$, while the LES model predicts the location of the reattachment point at $x/H \approx 2.7$, which is consistent with the Hussein and Martinuzzi (1996) experimental data. Also the recirculation zone at the top side of the obstacle is predicted wider in RSTM rather than the LES and LDV measurements. After all, the LES model very well captures the reattachment of the air flow at the trailing edge of the obstacle at its top side, which is the same as the experiment.



(a) Laser-Doppler Velocimetry measurements by Hussein and Matinuzzi (1996)



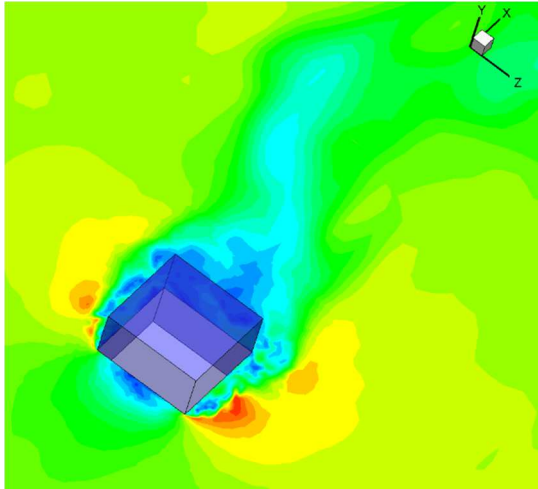
(b) RSTM model



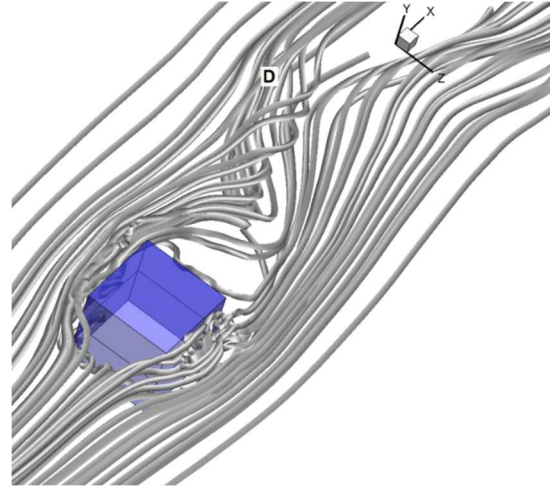
(c) LES model

Figure 2.8 Comparison of the flow around the block in the channel, modeled by RSTM and LES and the LDV experimental data of Hussein and Matinuzzi (1996).

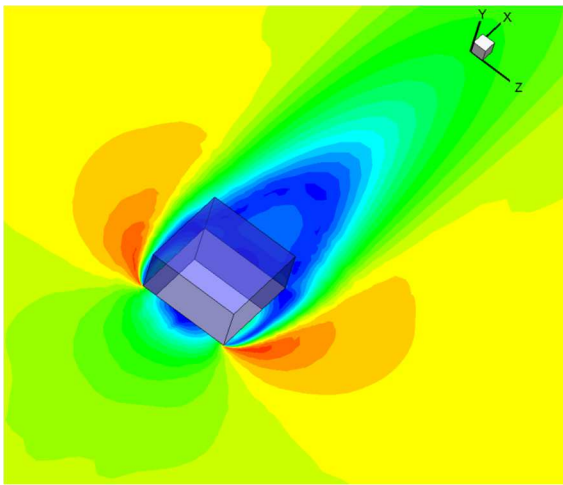
The instantaneous and time averaged LES of velocity field along the plane parallel the channel floor at $y/H = 0.5$ are shown in Figure 2.9. The flow field is sampled every 0.0001 second and time averaged over 1 minute.



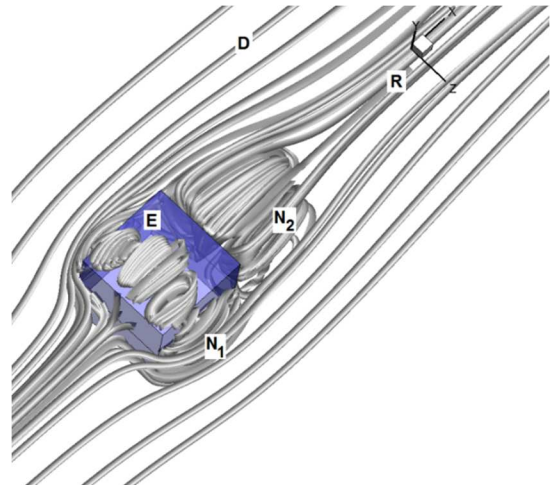
(a) A snapshot of velocity contours around the obstacle



(b) A snapshot of horseshoe vortices shedding from the obstacle



(c) The time-averaged velocity contours



(d) The 3D time-averaged streamlines

Figure 2.9 The instantaneous and time-averaged velocity contours and streamlines around the obstacle as predicted by LES. (a) and (c) show instantaneous and time-averaged velocity contours along the plane $y/H = 0.5$. (b) and (d) are the 3D instantaneous and time-averaged streamlines introduced at a front line on the plane $y/H = 0.5$.

The 3D streamlines, introduced upstream the block on the plane $y/H = 0.5$, are also depicted in Figures 2.9 (b, d). The large-scale flow structures identified from the time-

averaged computational simulation (Figure 2.9, (c) and (d)) include the recirculation region behind the block (N_2), the downstream reattachment region (R), and the lateral and top side vortices, (N_1) and (E) respectively. Also the streamlines around the horseshoe vortices (D) shedding from the block could be captured from the snap shot of the instantaneous streamlines in Figure 2.9 (b).

2.3.2 Simulation of wind flow around the CoE Building

2.3.2.1 Wind load and pressure field around the CoE Building

The simulated pressure coefficients for each major face of the building are compared with the experimental data of Kehs et al (2009) in this section. In the experiment fifty pressure taps were installed in the walls of the model, and the corresponding pressures of the wind flow on the building model were measured. The dimension of the building model is $12H \times 60L \times 20W$ (cm^3), where H is the height, L is the length and W is the width of the building. The simulation results are compared with the experimental data of Kehs et al (2009) for wind directions of north to south and west to east and with the bulk velocity of 10 m/s. The pressure coefficient defined as,

$$C_p = \frac{P - P_\infty}{1/2\rho U_\infty^2} \quad (2.18)$$

Wind pressure on the building when wind blows from north to south at $\text{Re}=81200$ ($U_\infty = 10$ m/s)

In this case study the wind blowing from north to south with velocity of $U_\infty = 10$ m/s, which corresponds to the Reynolds number of $\text{Re} = 81200$. The pressure data from the westward and the eastward facing walls of the building are presented, respectively, in

Figure 2.10 and Figure 2.11. These walls are parallel to the free stream flow. The flow separation from the leading edges of the side walls of the building leads to negative pressure magnitudes on these faces.

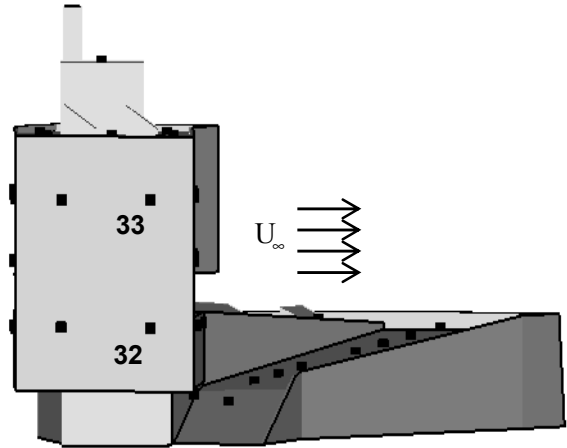
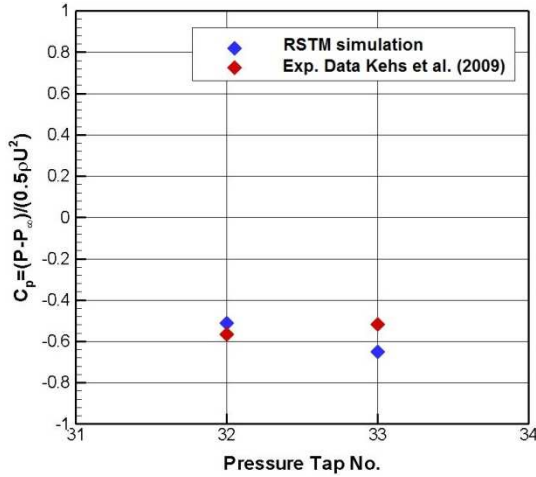


Figure 2.10 Pressure data on the west side wall, wind from north at $Re = 81200$ ($U_\infty = 10$ m/s).

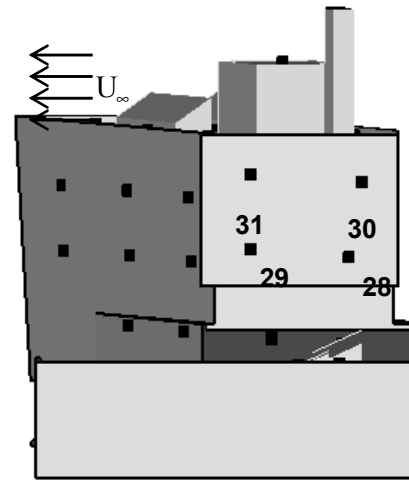
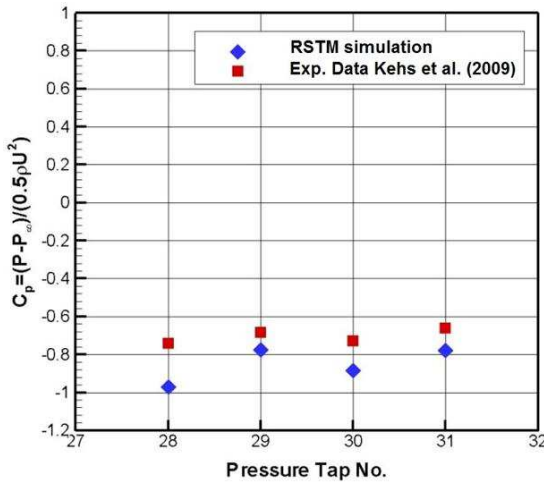


Figure 2.11 Pressure data on the east wall (side face), wind from north at $Re = 81200$ ($U_\infty = 10$ m/s).

Figure 2.12 compares the computed pressure coefficients with the experimental data on the windward side of the building, on the north face. It is seen that the pressure coefficients are positive and relatively high. The predicted pressure coefficients are in range of 0.4 to 0.8, which are in agreement with the experimental measurements. The largest discrepancies occurs for taps 7 and 11, which are in the lower parts of the building

model, and small recirculation underneath the building affected the predicted pressures at these taps.

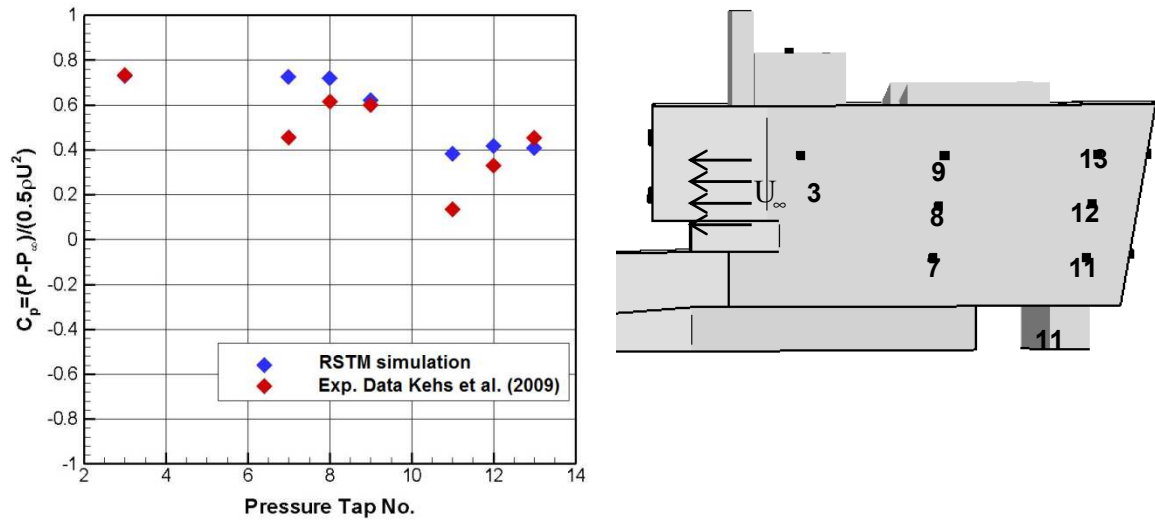


Figure 2.12 Pressure data on the north wall (windward face), wind from north at $Re = 81200$ ($U_\infty = 10$ m/s).

The predicted pressures on south side wall of the building are compared with the experimental data of Kehs et al. (2009) in Figure 2.13. A low pressure pocket, with pressure coefficients less than $C_p = -0.4$, were predicted in the numerical simulation for the south wall, at the downwind side of the building. The simulations are well following the experimental data except for the pressures taps 25 and 26, where the complex geometry of the building has made the flow field more complex at those locations.

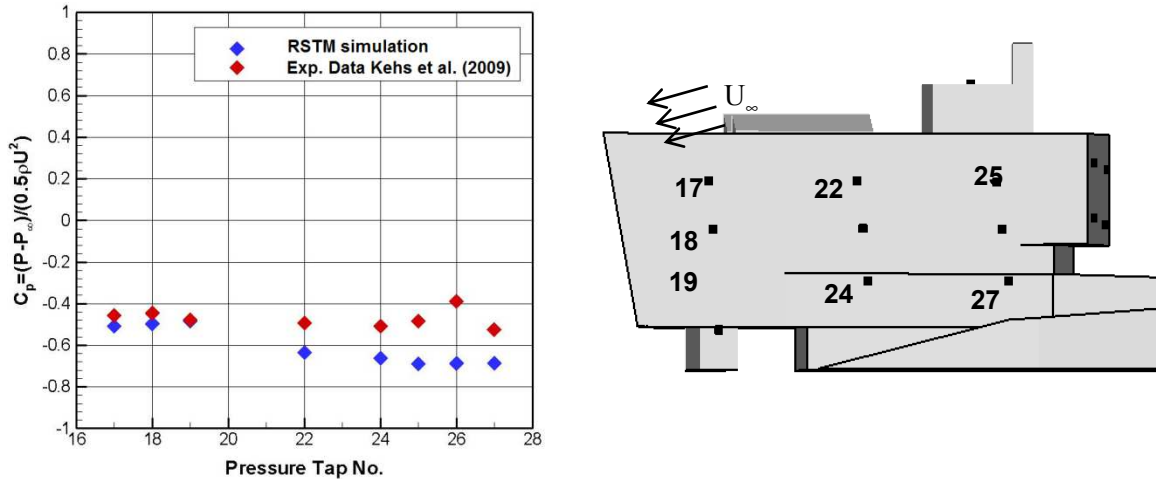


Figure 2.13 Pressure data on the south wall (downwind face), wind from north at $Re = 81200$ ($U_{\infty} = 10$ m/s).

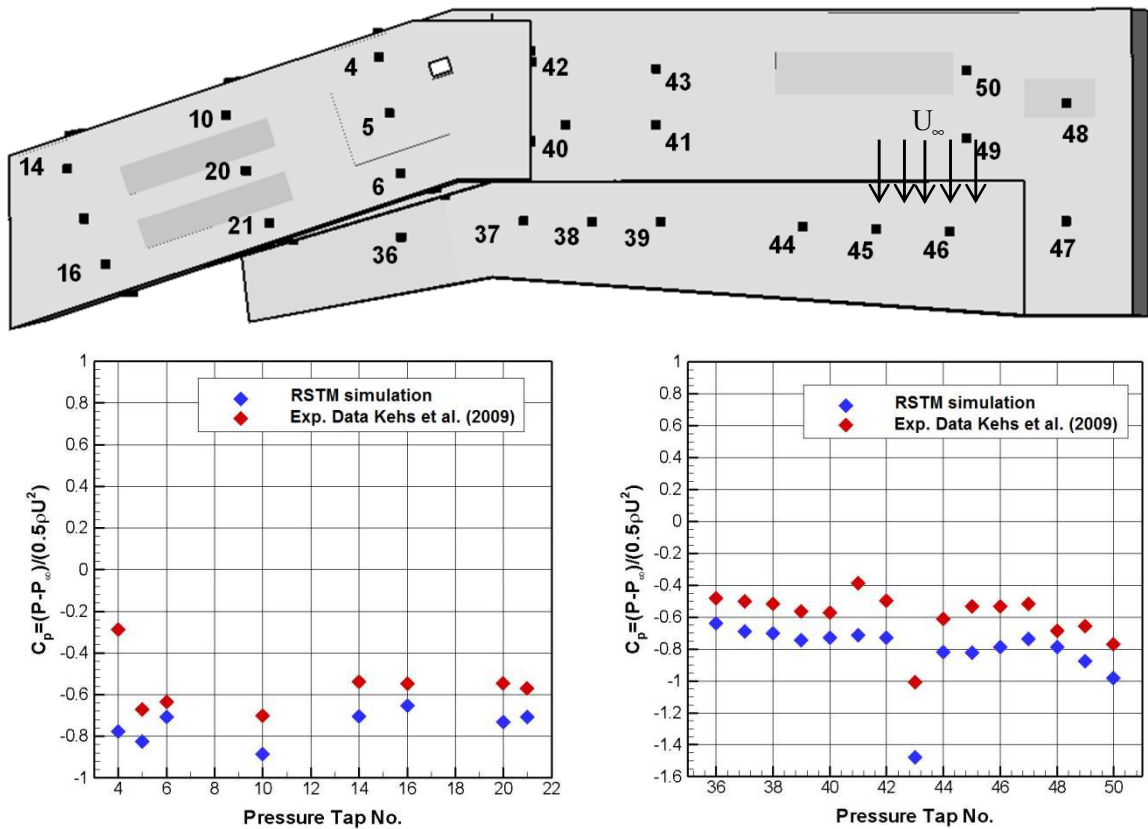


Figure 2.14 Pressure data on the roof (top face), wind from north at $Re = 81200$ ($U_{\infty} = 10$ m/s).

The roof surface was parallel to the wind stream. A negative pressure pocket was observed on the roof, which was due to the flow separation at the leading edge of the building and the flow recirculation over the roof surface. Comparing the numerical

simulation with the experimental measurements in Figure 2.14 showed that, excluding the pressures in tap locations 4, 41 and 43, the numerical simulation predicted the pressure magnitudes with less than $\Delta C_p = 0.2$ discrepancy from the experimental measurements. The multiple obstructions to the wind flow, such as the skylights, chimney and ventilation units, led to the complication in the flow close to the roof surface and caused the difference between the numerical simulation and the experimental measurements.

In this case study, where the wind blew from north to south, the pressure on the upstream face of the building was positive. The pressure magnitudes were negative on the rest of the building's walls. The numerical simulation was in good agreement with the experimental data and the average difference between the simulation data and the pressure tap measurements was $\Delta C_p = 0.168$.

Wind pressure on the building when wind blows from west to east at $Re=81200$ ($U_\infty = 10$ m/s)

The case when the wind direction is from west to east with free stream velocity of 10 m/s ($Re = 81200$) is described in this section. Figure 2.15 shows the pressure data simulated in the computer model and measured in the experiment of Kehs et al. (2009) on the windward face, when wind blows from west at $Re=81200$ ($U_\infty=10$ m/s). The pressure pocket on the west wall of the building is positive with the pressure coefficient, C_p , close to 1. The numerical simulation overpredicts the pressure magnitudes in the tap positions, 31 and 32 with the maximum discrepancy of $\Delta C_p = 0.3$. The westward facing wall of the building has a slight angle, 10° , toward the main stream, and it is not exactly perpendicular to the flow. The discrepancy between the pressure magnitude obtained

from the experiment and the simulation is due to the complexity of the geometry and the recirculation region after the separation of the flow stream from the leading edge of the side wall.

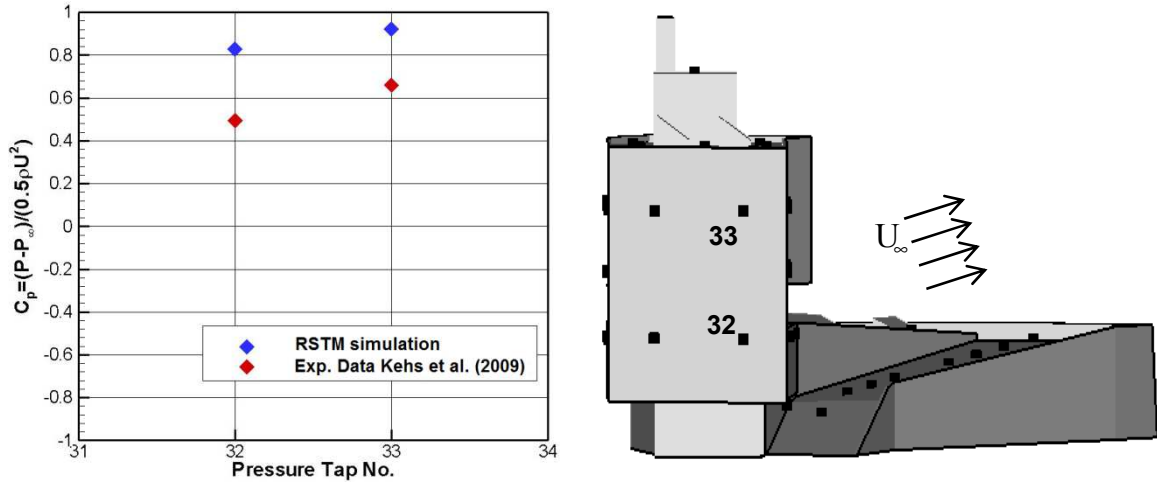


Figure 2.15 Pressure data on the west wall (windward face), wind from west at $Re = 81200$ ($U_\infty = 10\text{m/s}$).

Figure 2.16 shows that the pressure magnitude on the eastward facing of the building is predicted as $C_p = -0.4$. The face is at the downwind and the wind circulation at that vicinity causes the negative pressure pocket. The numerical simulation is in a good agreement with the pressure tap measurements, with the largest difference of $\Delta C_p = 0.15$ occurring at the tap 28.

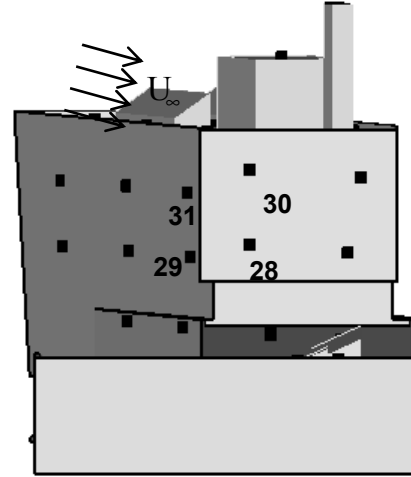
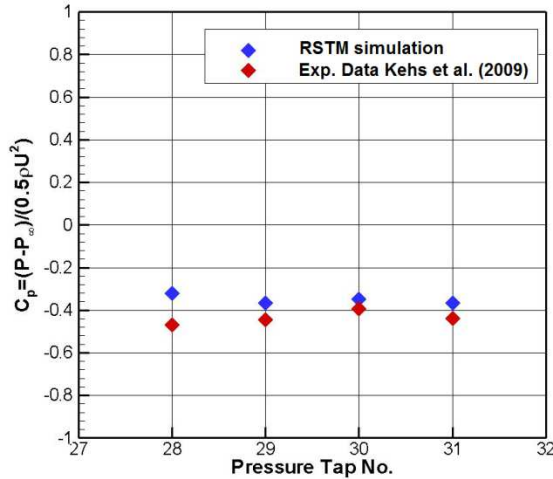


Figure 2.16 Pressure data on the east wall (downwind face), wind from west at $Re = 81200$ ($U_\infty = 10\text{m/s}$).

Figure 2.17 shows experimental and numerical pressure data on the northern wall of the building. The pressure coefficients on the north wall of the building are negative on the pressure taps 11, 12 and 13 close to the upstream edge of the building. However, the pressure becomes close to zero near the middle of the wall surface at the taps 7, 8 and 9, and again it changes to the negative magnitude at the area close to the trailing edge of the wall. The increase of the pressure magnitude at the middle of the north wall suggests that the wind flow reattached to the wall, while the negative pressure at the tap position 3 illustrates that the wind flow is detached from the trailing edge of the north wall. The simulation results overestimate the sub-ambient experimental pressures slightly, for the taps 11, 12, and 13 that the differences between the experiment and the simulation are about $\Delta C_p = 0.3$.

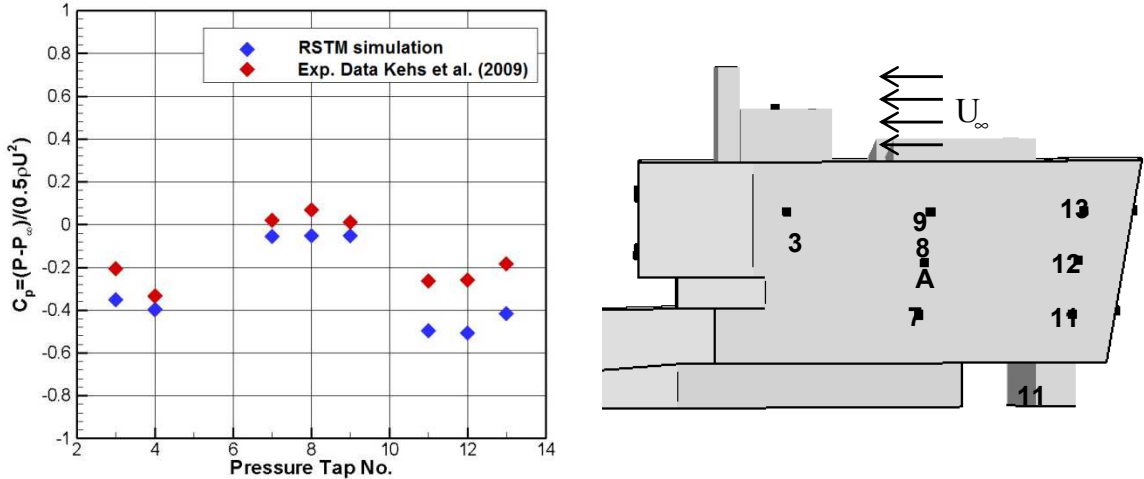


Figure 2.17 Pressure data on the north wall (side face), the wind from west at $Re = 81200$ ($U_\infty = 10\text{m/s}$).

Figure 2.18 shows a low pressure region is formed in the vicinity of the south wall, where the pressure coefficients varies between $C_p = -0.7$ and $C_p = -0.5$. Comparing the simulated pressure coefficients with the experimental data shows that the simulation results closely follow the experimental measurements for this side wall of the building.

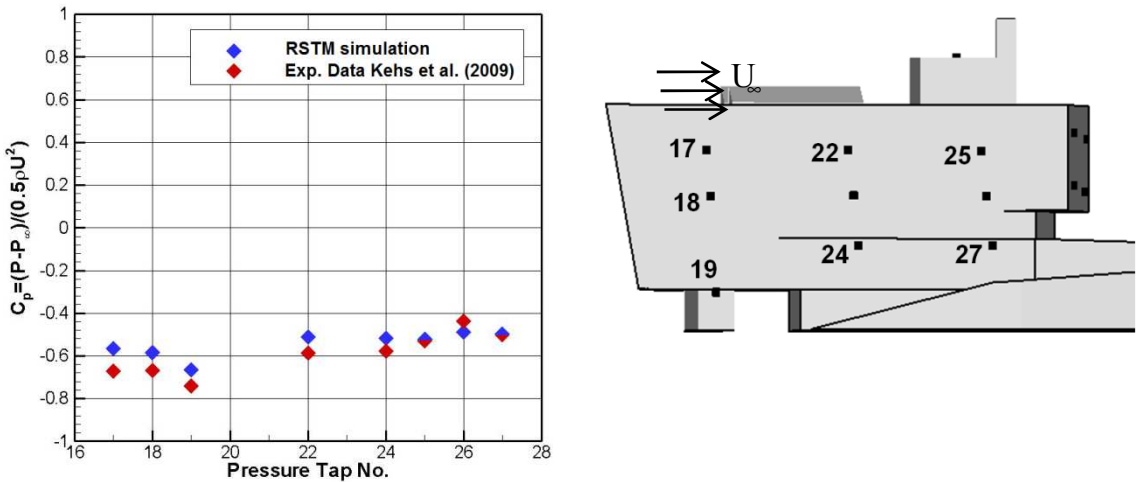


Figure 2.18 Pressure data on the south wall (side face), the wind from west at $Re = 81200$ ($U_\infty = 10\text{m/s}$).

A comparison between the simulated surface pressures and the experimental data of Kehs et al. (2009) on the roof surfaces is provided in Figure 2.19. It is seen that the pressure is sub-ambient on the roof of the building, and the simulation results are in good agreement with the experimental data. This figure also shows that positive pressure coefficients are

predicted in numerical simulation on the eastern end of the ramp. The positive pressure coefficients implied the reattachment of the flow. However, the experiment did not show the same reattachment signature in the pressure measurements. The experimental pressure coefficient is slightly positive at the tap 45, but is negative for the every other tap in this region. Most pressure coefficient differences between the simulation and the experiment, however are less than $\Delta C_p = 0.3$. The largest difference $\Delta C_p = 0.4$ between the experiment and the simulation occurs at the tap 20.

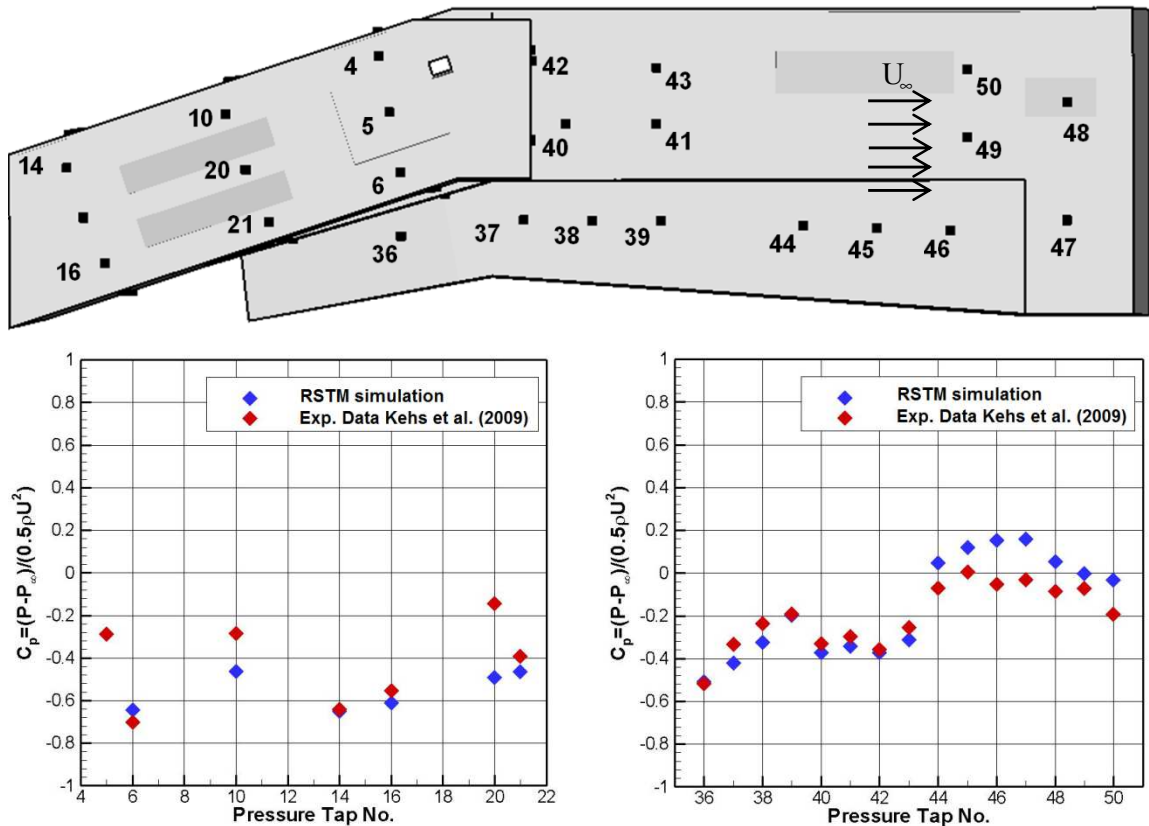


Figure 2.19 Pressure data on the roof (top face), wind from west at $Re = 81200$ ($U_\infty = 10\text{m/s}$).

Therefore, in summary, negative pressure regions form on the side walls and downstream walls of the CoE Building, while the pressure on the windward wall is positive. This observation is consistent with other bluff body experiments, which the pressure coefficients were less than zero on the roofs parallel the incident wind. The numerical

simulation results follow the trend of the experimental data of Kehs et al. (2009), with the average difference between the simulation results and the experimental data of $\Delta C_p = 0.100$.

2.3.2.2 Velocity field around CoE building for the wind from north to south

The accuracy of the simulation of the wind flow over a bluff body with complex geometry is evaluated by comparing the flow field over CoE Building model predicted by RSTM and LES turbulence models with the Particle Image Velocimetry (PIV) data of Kehs (2009). The PIV data was captured on two planes crossing the building in stream wise direction. The schematic of the building and the planes that the RSTM and LES simulations of the flow fields are compared with the PIV data are shown in Figure 2.20.

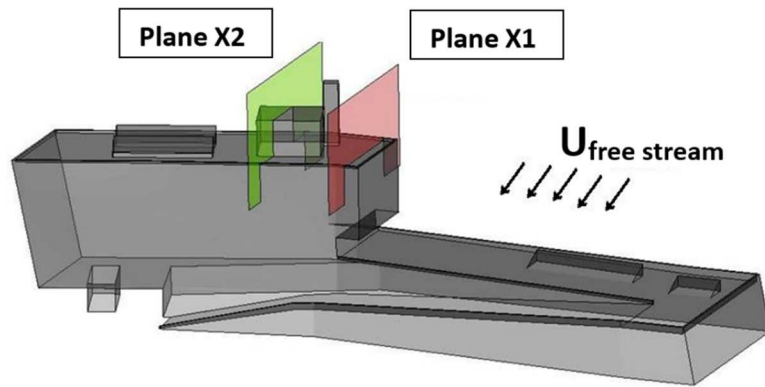


Figure 2.20 Position of Planes (X1) and (X2), wind blowing from north to south.

The velocity and the vorticity variables are normalized by the free stream velocity magnitude, U_0 , and the length scale of the building, H . The length scale is the height of the building model, $H = 121.8$ mm, and the free stream velocities, U_0 , is the wind speed of 10 m/s. The normalized velocity and vorticity scales are given as,

$$v_{norm} = \frac{v}{U_0} \quad (2.19)$$

$$\omega_{norm} = \frac{\omega H}{U_0} \quad (2.20)$$

The time-averaged velocity magnitudes which are predicted by the RSTM and LES, and projected on the plane X1 are compared with the PIV data of Kehs et al. (2009) in Figure 2.21. Here for free stream velocity of 10 m/s, the Reynolds number is 81,680. In the three case studies the wind flow separation occurs at the leading edge of the building, and a recirculation region appears at the back side of the building. However, although the PIV experiment shows that the wind flow reattaches to the top surface of the CoE Building on the plane X1, the RSTM simulation was not able to predict this trend. The streamlines simulated in RSTM illustrate the presence of a large recirculation region with no reattachment on the roof surface. The velocity magnitude in the recirculation region is also slightly larger than the experiment data.

The time-averaged velocity magnitude predicted by the LES model, Figure 2.21 (c), shows that the LES model is able to capture the flow reattachment on the top side of the building at $y/H = -0.35$, which is close to the reattachment point obtained from the PIV experimental data at $y/H = -0.3$.

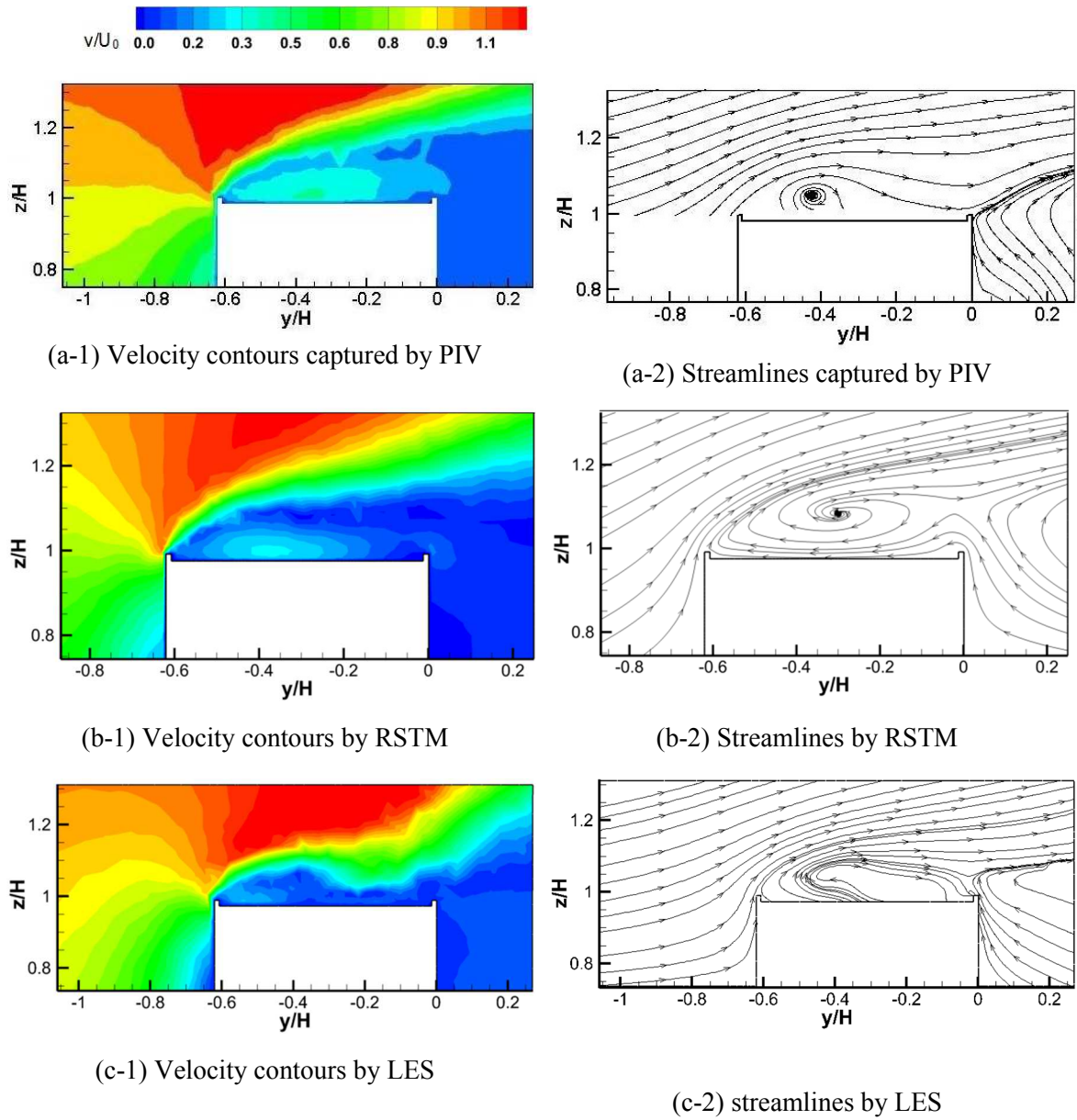
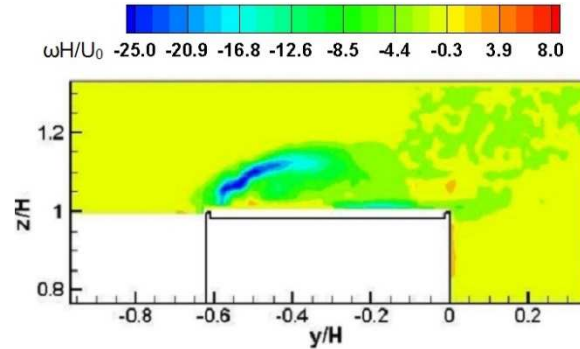


Figure 2.21 Comparison of the mean normalized velocity structures between the PIV experiment of Kehn et al. (2009), RSTM and LES for wind at $Re = 81200$ ($U_0 = 10$ m/s) on Plane X1.

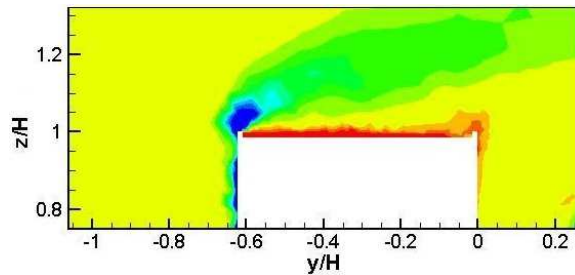
The time-averaged LES model, also, predicts the flow separation from the trailing edge on top surface of the building on Plane X1, which is consistent with the PIV experiments.

The mean out of plane vorticity, predicted by the RSTM and LES are also compared with the experimental data in Figure 2.22. The simulation results show a high mean vorticity

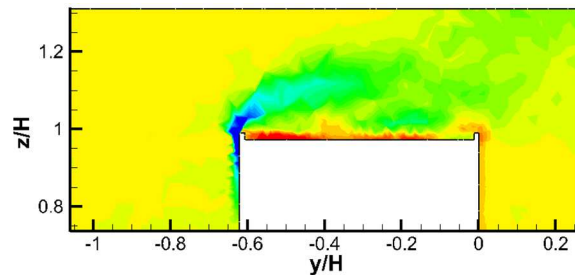
region near the leading edge of the building. The intensity of the downstream vorticity in the RSTM simulation did not decrease as rapidly as the experiment. The experimental results show a longer and narrower region of high magnitude vorticity, which is consistent with the LES results shown in Figure 2.22 (c). The magnitudes of the positive vorticities predicted by the simulations are similar to the experimental data.



(a) PIV of vorticity on plane X1



(b) RSTM prediction of vorticity on plane X1



(c) LES prediction of vorticity on plane X1

Figure 2.22 Comparison of mean normalized out of plane vorticity between the PIV experiment, RSTM and LES for the wind with $Re = 81,200$ ($U_0 = 10$ m/s) on Plane X1.

A high level of positive vorticity appeared directly beyond the roof surface in the simulations. PIV data in this region, however, was not available due to the shadow effects.

The contours of velocity magnitude on the plane X2 are presented in Figure 2.23. Similar to the experiment results, both the RSTM and the LES predict the flow separation at the leading edge of the building, with no reattachment on the top side of the plane X2. Two recirculation regions, are formed; one over the top face and the other one at the back of the building. In the RSTM simulations, the center of the recirculation region, over the top surface of the building, is at $y/H \approx -0.35$, $z/H \approx 1.23$, whereas in the experimental data the center is at $y/H \approx -0.30$, $z/H \approx 1.2$, which agrees with the LES predictions. The velocity magnitude predicted by the LES is also closer to the experimental data compared to that of RSTM.

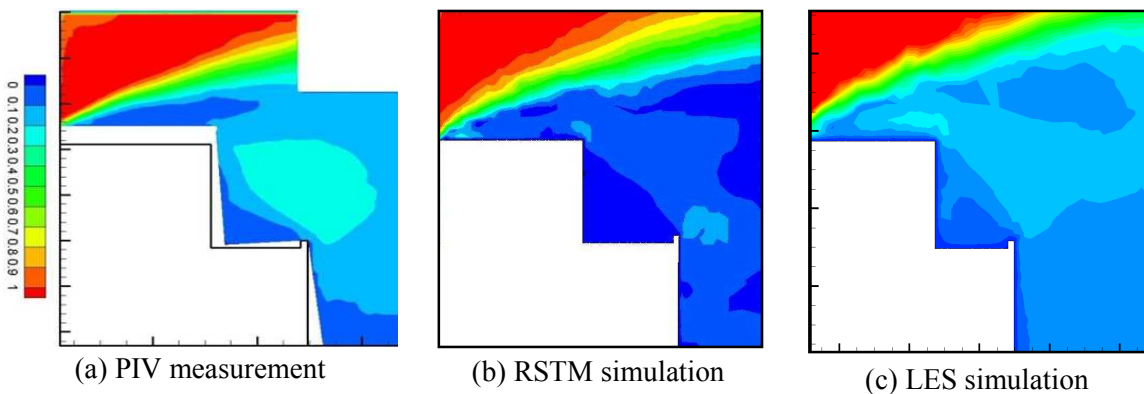


Figure 2.23 Comparison of the flow field on plane X2, (a) PIV measurements, (b) RSTM turbulence model, and (c) LES model.

2.4 Conclusions

Reynolds stress transport turbulence model and LES turbulence model were used to study the airflow field around a wall mounted square cylinder and the scale model of the CoE Building in the wind tunnel.

Both numerical simulations predicted the separation at the tip of the square cylinder, but the recirculation at the top was better predicted by the LES model. The RSTM predicted

the location of the reattachment point behind the block too far ($X_R/H \gg 2.7$) compared with the experimental data and the LES results ($X_R/H = 2.7$).

In addition, the comparison of the numerical simulations with the available PIV experimental data for the flow over the CoE building showed that the RSTM could predict the separation at the leading edges of the building; however, it could not capture the flow reattachment at the top side of the Plane X1. This could be due to the complexity of the building geometry. The LES turbulence model improved the prediction of the mean velocity field. It predict the flow reattachment at the top surface of the CoE Building on the plane X1 at $Y/H \approx -0.17$. While the (PIV) experiment could not show the exact reattachment point because of the reflections from the surface, it is approximated as $Y/H \approx -0.22$.

In summary, the Large eddy Simulation (LES) overcame the deficiencies of the RSTM in predicting the details of the airflow field for the rather complex configuration of the CoE Building at a high Reynolds number.

Acknowledgements

Thanks to EPA and CoE center at Syracuse, NY for funding this project.

References

- Ahmadi, G., and Li, A. (2000). "Computer simulation of particle transport and deposition near a small isolated building." *J.Wind Eng.Ind.Aerodyn.*, 84(1), 23-46.
- Hussein, H. J., and Martinuzzi, R. (1996). "Energy balance for turbulent flow around a surface mounted cube placed in a channel." *Phys.Fluids*, 8 764.
- Kehe, J. (December 2009). "Experimental Study of Airflow around the Syracuse COE Building." PhD thesis, Clarkson University, .

Kehs, J., Bohl, D., Ahmadi, G., and Tavakoli, B. (2009). "Experimental Study of Airflow Around the Syracuse CoE Building." ASME, .

Launder, B., Reece, G., and Rodi, W. (1975). "Progress in the development of a Reynolds-stress turbulence closure." *J.Fluid Mech.*, 68(03), 537-566.

Lesieur, M., and Metais, O. (1996). "New trends in large-eddy simulations of turbulence." *Annu.Rev.Fluid Mech.*, 28(1), 45-82.

Lilly, D. (1992). "A proposed modification of the Germano subgrid-scale closure method." *Physics of Fluids A: Fluid Dynamics*, 4 633.

Nicoud, F., and Ducros, F. (1999). "Subgrid-scale stress modelling based on the square of the velocity gradient tensor." *Flow, Turbulence and Combustion*, 62(3), 183-200.

Smagorinsky, J. (1963). "General circulation experiments with the primitive equations." *Mon.Weather Rev.*, 91(3), 99-164.

CHAPTER III. Computational model of particle distribution and deposition over an obstacle with complex geometry

Abstract

The deposition of particles in 2D horizontal and vertical channel under turbulent flow regimes are evaluated. The accuracy of the computational model is assessed by comparing the model predictions for deposition velocity with earlier experimental data and numerical simulation results. The turbulent velocity fluctuations are modeled using the Langevin stochastic differential equation. Effects of various parameters on the deposition velocity of particles in the turbulent duct flow is investigated.

In this chapter computational models for generating turbulent fluctuations when the RANS-RSTM is used, and subgrid scale fluctuations when LES is used are developed. User defined functions were developed and implemented into the ANSYS Fluent version 12.1 commercial CFD solver to include the effect of turbulent fluctuations. Formerly, a model is developed by Tian and Ahmadi (2007) to track particles in RANS models of steady turbulent flows. The subroutine developed here uses the Fluent software to track particles in transient turbulent flows, and modifies the velocity fluctuations in both RANS and LES turbulence models.

The validated particle transport equation is applied for tracking particulate pollutants around the model of the Center of Excellence (CoE) Building, which has a complex configuration. To account for the details of the wind flow around the CoE Building,

particles are injected in the large eddy simulation (LES) of the flow field. The subgrid scale velocity fluctuations are modeled using also the Langevin stochastic equation. The particles Brownian motion, Saffman lift force and gravity force are also included in the analysis. The local deposition velocity of particles on the walls and the ground around the building showed that a large fraction of particles trap on the ground and the building façade facing the wind flow. The minimum deposition occurs on the walls behind the building with respect to the wind direction and the pollution source. It was also found that a major fraction of injected particles concentration deposits on the top side of the building. This is due to the high levels of turbulent intensity and the formation of recirculation regions in this area.

3.1 Introduction

Urban air pollution, which is mainly attributed to vehicle emissions, has been of concern due to its adverse effect on human health. Using the outdoor air with low levels of pollution, however, can reduce the energy cost of the conventional HVAC systems. Therefore, an in-depth understanding of the wind flow condition and the pollutant transport to buildings is important for determining the air quality for mechanical and natural ventilation systems.

Center of Excellence (CoE) Building was built in Syracuse, NY at the intersection of two major highways. The wind flow around the scale model of the CoE Building was analyzed in chapter II. The RSTM and LES simulation results were compared with the PIV measurements of Kehs et al (2009) under the identical conditions and good agreements were found. This chapter is focused on understanding the mechanisms of

particle transport and deposition in turbulent wind flow fields. The Lagrangian particle trajectory analysis approach is used. Drag force, Saffman lift force, gravity and Brownian motion are considered in particles transport equations. The turbulent velocity fluctuations are modeled using the Langevin stochastic equation, and their effect on particle deposition velocity in the channel flow is evaluated by comparing the results with the existing experimental data as well as with the simulations in which the Discrete Random Walk (DRW) model is applied to reconstruct the turbulent fluctuations.

The dispersion and the local deposition of particulate air pollutants around the model of the CoE Building are investigated, considering turbulent velocity fluctuations. The transport of particles in the size range of 1 μm to 10 μm is studied using the Eulerian-Lagrangian approach. The computer simulations showed that the airflow separation at the side walls and at the wake behind the building generated strong recirculation regions. High intensity turbulent fluctuations formed in these regions, also, lead to dispersion and deposition of particles around the building.

3.2 Computational model and boundary conditions

3.2.1 Numerical model of particle transport in a 2D channel flow

The 2D channel-flow is simulated using transient Reynolds stress transport turbulence model (RST) and particle distribution and deposition in size range of 1.5 μm to 50 μm are studied. The dimensions and the flow conditions are set based on the numerical model presented by Tian and Ahmadi (2007). The channel height is $H_{ch} = 0.02\text{ m}$, and the Reynolds number based on the channel height is $Re = 6845$. To reduce the needed

computational time and capacity, the channel length is considered to be 0.05 m, and a periodic boundary condition for the flow velocity is imposed at the inlet and outlet of the channel so that a fully developed turbulent flow in the short channel length can be established. Highly resolved fine grids are generated in the boundary layer. The normal distance of the first node from the channel wall is 17.5 μm , which corresponds to the wall unit of $y^+ = \frac{y u^*}{\nu} = 0.2$. The shear velocity is $u^* = \sqrt{\frac{\tau}{\rho}} = 0.32 \frac{\text{m}}{\text{s}}$, which agrees with Tian and Ahmadi (2007) simulation conditions. The enhanced wall treatment is applied to resolve the velocity profile in the boundary layer near the wall. When the first nodes are located in the viscous sublayer ($y^+ \propto 1$), the two layer zonal boundary condition of Chen and Patel (1988) is used. The enhanced wall function of Kader (1981) is used for coarser grids. The implicit time integration scheme with a time step of 5×10^{-5} s is employed for the RANS-RSTM model.

The particle distribution and deposition in the channel flow are analyzed using the one way coupled Lagrangian approach. Particles in size range of 1.5 μm to 50 μm are injected from the inlet plane. When a particle reaches the outlet, it would be re-injected from the inlet at the same position due to the periodic boundary condition. In the particle transport equation, the effects of Brownian motion, Saffman lift force and gravity force, as well as, the turbulent velocity fluctuations are considered. The velocity fluctuations are derived from a Continuous Random Walk (CRW) model using Langevin stochastic equation. The terms in the Langevin equation are described in more details in the section of governing equations.

After evaluating the particle transport model for the test case of the channel flow, the particulate pollutant distribution and deposition around the CoE Building is investigated. As discussed in chapter I, while the RSTM model could not capture all details of the flow field around the CoE Building, LES was consistent with the PIV experimental data of Kehs et al. (2009). Therefore the particle transport around the CoE Building is studied in the flow field predicted by the LES. Particles are injected upstream from the projection plane of the building which is in the distance of 0.22 m which is about two times as long as the building height. The injection plane size is large enough so that the injected particles can cover the space surrounding the building model. In order to consider the effect of Sub-Grid Scale (SGS) turbulent fluctuations on particle distribution and deposition, a Gaussian fluctuating random field model is used. The SGS root-mean square velocity fluctuation, σ_{SGS} , is considered as the residual fluid velocity scale seen by particles and local grid size as the length scale to capture the Lagrangian time scale.

The deposition rate of particles in sizes of 1, 3, 5, 7 and 10 μm on several locations on the walls and the ground surrounding the building is analyzed.

3.3 Governing equations

3.3.1 Particle transport equation

Since the number concentration of particulate pollutants is small, a one-way coupling Lagrangian approach is applied to study the particle transport in the flow field. The equation of motion of particle is given as,

$$\frac{du_i^p}{dt} = F_D(u_i^f - u_i^p) + \frac{g(\rho_p - \rho_f)}{\rho_p} + n_i(t) + F_i^L \quad (3.1)$$

The first term on RHS of equation (11) is the drag force where F_D is given as,

$$F_D = \frac{1}{\tau} \frac{C_D Re_p}{24} \quad (3.2)$$

Here C_D represents the drag coefficient adopted from the expression of Morsi and Alexander (1972) and τ is the particle relaxation time defined as,

$$\tau = \frac{S_p d_p^2 C_c}{18\nu} \quad (3.3)$$

where S_p , ν and C_c are the particle-to-fluid density ratio, fluid kinematic viscosity and Stokes-Cunningham slip correction factor, respectively. The particle-to-fluid density ratio is fixed at $\frac{\rho_p}{\rho_f} = S_p = 2000$. The relative Reynolds number, Re_p , is defined as,

$$Re_p = \frac{d_p |u^p - u^f|}{\nu} \quad (3.4)$$

The second term on RHS of equation (11) is the gravity force which is an important factor in distribution and deposition of large particles. For small particles ($d_p < 0.1 \mu\text{m}$), Brownian motion is the key mechanism for particles dispersion, which is included in term $n_i(t)$ in the RHS of equation (3.1). The Brownian motion is modeled as a white noise excitation, $n(t)$, with spectral intensity given as (Li and Ahmadi, 1992)

$$S_{nn} = \frac{216\nu k_b T}{\pi^2 \rho_f d_p^5 S_p^2 C_c} \quad (3.5)$$

where $k_b = 1.38 \times 10^{-23}$ j/K is the Boltzmann constant, and T is the ambient air temperature. The Saffman lift force F_i^L is given as,

$$F_i^L = \frac{2K_c \nu^{\frac{1}{2}}}{S_p d_p (s_{lk} s_{kl})} s_{ij} (u_j^f - u_j^p) \quad (3.6)$$

where $K_c = 2.594$ is the constant coefficient of Saffman lift force (Saffman, 1965), and s_{ij} is the deformation rate tensor given as,

$$s_{ij} = \frac{1}{2} \left(\frac{\partial u_i^f}{\partial x_j} + \frac{\partial u_j^f}{\partial x_i} \right) \quad (3.7)$$

The instantaneous fluid velocity in the turbulent flow is given by $u_i^f = \overline{u_i^f} + u_i^{f'}$, where $\overline{u_i^f}$ is the time averaged velocity evaluated by the RANS turbulence model or the large scale velocity in the LES. $u_i^{f'}$ is the i^{th} component of the turbulent velocity fluctuation in RANS model or the subgrid-scale velocity in the LES. Either in Reynolds averaged Navier-Stokes (RANS) turbulence models like Reynolds stress transport turbulence model (RSTM) which is based on time averaging the instantaneous velocity, or in the large eddy simulation (LES) which filters the large scale eddies, the fluctuation velocity (or subgrid scale velocity) $u_i^{f'}$ is not modeled. As shown in section 3.4.1.2, small scale fluctuation velocity, $u_i^{f'}$, plays an important role in particles dispersion and deposition. In

section 3.3.2 the continuous random walk (CRW) model for generating velocity fluctuations from RSTM and in section 3.3.3 the terms of the CRW model for generating SGS velocities in LES are described.

3.3.2 Continuous Random Walk (CRW) Model for turbulent velocity fluctuations in RANS-RSTM turbulence model

To include the effect of turbulence on particles transport and dispersion, a stochastic model based on the Langevin equation is typically used for reconstruction of the turbulent velocity fluctuations. Accordingly, the Langevin equation is given as,

$$\frac{d}{dt} \left(\frac{u_i^{f'}}{\sigma_i} \right) = -\frac{u_i^{f'}}{\sigma_i \tau_L} + \frac{2}{\sqrt{\tau_L}} \xi_i(t) \quad (3.8)$$

Here σ_i is the fluctuating root mean square (RMS) of velocity, $\sqrt{u_i^{f'} u_i^{f'}}$, τ_L is the turbulent Lagrangian time scale, and $\xi_i(t)$ is a continuous Gaussian white-noise random process with spectral intensity of $1/\pi$. When Equation (3.8) is discretized for numerical simulation, $\xi_i(t)$ is evaluated as

$$\xi_i(t) = \frac{\lambda_i}{\sqrt{\Delta t}} \quad (3.9)$$

Here λ_i are selected from a population of independent random Gaussian numbers with zero mean and unit variance at every time step.

Based on the fits to the DNS of channel flow conducted by Dreeben and Pope (1997) Dehbi (2008) suggested the following expressions for RMS velocities near the wall for $y^+ < 100$,

$$\sigma_1^+ = \frac{\sigma_1}{u^*} = \frac{0.4y^+}{1 + 0.0239(y^+)^{1.498}} \quad (3.10)$$

$$\sigma_2^+ = \frac{\sigma_2}{u^*} = \frac{0.0116(y^+)^2}{1 + 0.203(y^+) + 0.00114(y^+)^{2.421}}$$

The above equation satisfies the quadratic variation of normal velocity fluctuations near the wall as suggested by Li and Ahmadi (2007), $\sqrt{v'^2} \propto y^2$ as $y \rightarrow 0$. In the bulk region with $y^+ > 100$, the RMS quantities evaluated from RSTM model are used. That is,

$$\sigma_1 = \sqrt{R_{11}} = \sqrt{u_1^{f'} u_1^{f'}} \quad (3.11)$$

$$\sigma_2 = \sqrt{R_{22}} = \sqrt{u_2^{f'} u_2^{f'}}$$

The Lagrangian time scale, τ_L , in near wall flows for , $y^+ < 100$, is given as,

$$\tau_L^+ = 10, \quad y^+ \leq 5$$

$$\tau_L^+ = 7.122 + 0.5731y^+ - 0.00129y^{+2}, \quad 5 \leq y^+ \leq 100 \quad (3.12)$$

where

$$\tau_L^+ = \frac{\tau_L(u^*)^2}{\nu}$$

For the RSTM turbulence model the Lagrangian time scale at $y^+ > 100$ is given as,

$$\tau_L = \frac{2}{C_0} \frac{k}{\varepsilon} \quad (3.13)$$

where k and ε are evaluated from the RSTM model. According to Mito and Hanratty (2002) study of turbulent dispersion of fluid particles in a channel flow, the Lagrangian time scale given by (3.13) with $C_0 = 14$ fits the DNS results.

3.3.3 Continuous Random Walk (CRW) Model of turbulent velocity fluctuations in LES

When compared with RANS-RSTM, LES better predicts the main flow features around the obstacles with complex geometries. However, the model for subgrid scale velocity fluctuation in LES is not available in the ANSYS Fluent version 12.1 for particle tracking. Therefore, a model for subgrid scale velocity fluctuations in LES with dynamic kinetic energy subgrid-scale model is developed. The subgrid velocity scale, σ_{sg} , and the subgrid Lagrangian time scale, τ_{sg} , in equation (3.8) are defined as follows,

$$\sigma_{sg} = \sqrt{\frac{2}{3} k_{sg}} \quad (3.14)$$

$$\tau_{sg} = \frac{\Delta F}{\sqrt{\frac{2}{3} k_{sg}}} \quad (3.15)$$

Where the ΔF is the LES filter length scale. The subgrid scale turbulent kinetic energy, k_{sg} , is evaluated using the dynamic kinetic energy subgrid-scale model proposed by Kim and Menon (1997). That is,

$$k_{sg} = \frac{1}{2} (\overline{u_k u_k} - \overline{u_k} \overline{u_k}) \quad (3.16)$$

The subgrid scale eddy viscosity, ν_t , is computed using k_{sg} . That is,

$$\nu_t = C_k k_{sg}^{\frac{1}{2}} \Delta F \quad (3.16)$$

where ΔF is the filter-size which is the cells length scale, $\Delta F \equiv V^{\frac{1}{3}}$

The transport equation for k_{sg} is given as,

$$\frac{\partial k_{sg}}{\partial t} + \partial \overline{u_j} \frac{\partial k_{sg}}{\partial x_j} = -\tau_{ij} \frac{\partial \overline{u_i}}{\partial x_j} - C_\varepsilon \frac{\partial k_{sg}^{\frac{3}{2}}}{\Delta F} + \frac{\partial}{\partial x_j} \left(\frac{\nu_t}{\sigma_k} \frac{\partial k_{sg}}{\partial x_j} \right) \quad (3.17)$$

where $\tau_{ij} = -2C_k k_{sg}^{\frac{1}{2}} \Delta F \overline{S_{ij}} + \frac{2}{3} k_{sg} \delta_{ij}$ is the shear stress, and the constants C_k and C_ε are determined dynamically by referring to the similarity between the parameters (stress and dissipation) in grid-filter level and test-filter level presented by Kim and Menon (1997) (for instance, $C_k = \frac{1}{2} \frac{L_{ij} \sigma_{ij}}{\sigma_{ij} \sigma_{ij}}$ where L_{ij} is the test-scale Leonard stress tensor).

3.4 Results and discussions

3.4.1 Effect of turbulent velocity fluctuations on particle deposition rate in a channel flow

3.4.1.1 Channel flow

The flow field in a 2D channel is simulated using unsteady Reynolds Stress Transport turbulence model. In order to generate fully developed velocity along the channel, inlet and outlet are treated as periodic boundaries. The contour of normalized velocity and turbulent kinetic energy along with their profiles on a line crossing the mid-channel are shown in Figure 3.1 and Figure 3.2. The flow is fully developed, and the profiles of the velocity and the turbulent kinetic energy are identical to the RSTM results of Lin and Ahmadi (2007). The turbulent kinetic energy is maximum in vicinity of the walls and minimum in the middle of the channel.

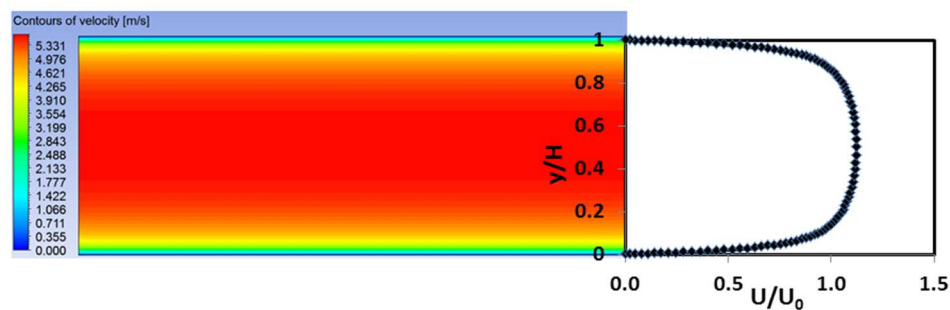


Figure 3.1 Contours and profile of streamwise velocity in a 2D channel flow.

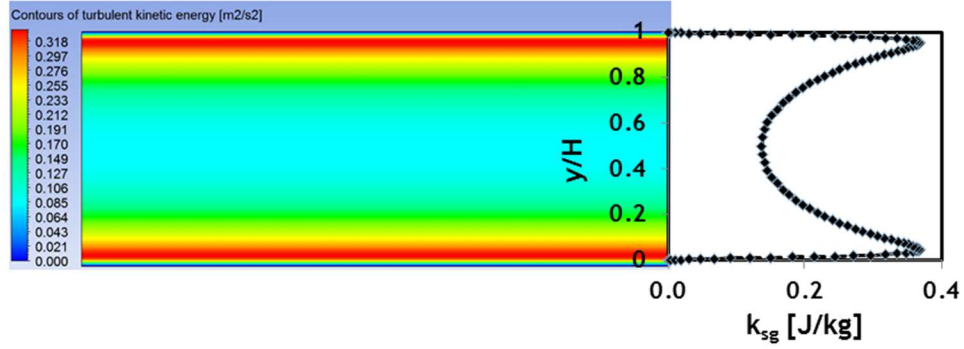
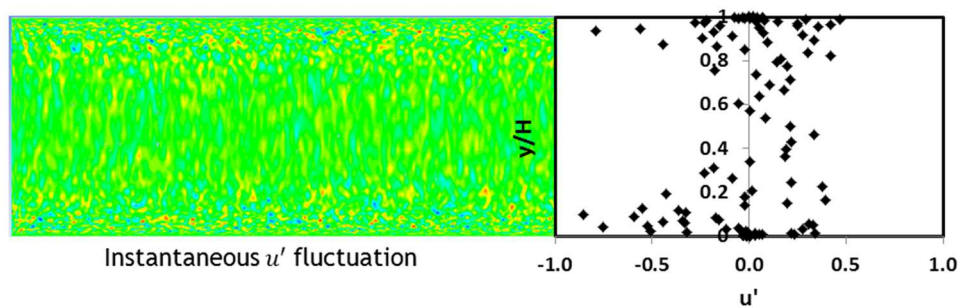
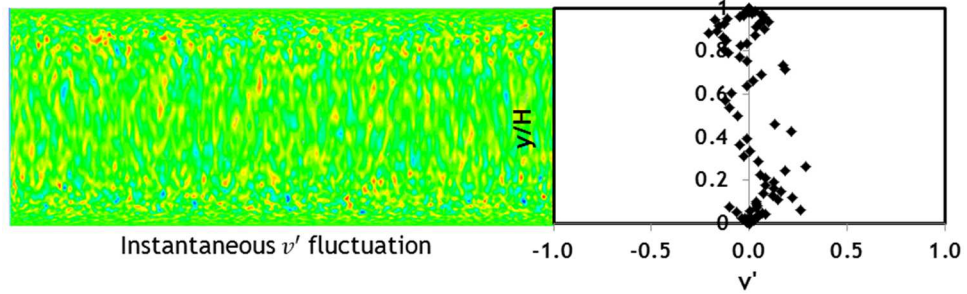


Figure 3.2 Contours and profile of turbulent kinetic energy in the channel flow.

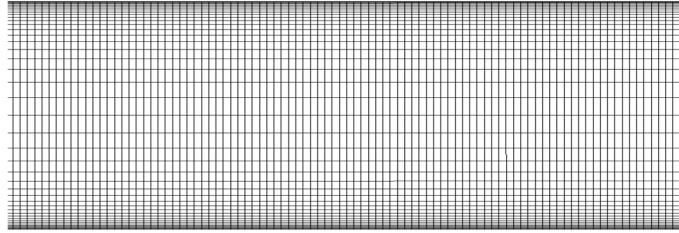
The instantaneous velocity fluctuations are modeled in the entire flow field using the Langevin stochastic differential equation. The snap shot of the contours of turbulent velocity fluctuations, u' and v' , on a plane along the channel length is presented in Figure 3.3. In addition to the contours, the magnitudes of the velocity fluctuations (u' and v') on the center line of the cross section in the middle of the channel, perpendicular to the main stream, are presented in RHS of Figure 3.3. The streamwise velocity fluctuations, u' , are larger close to the walls, which is due to the generation of turbulent kinetic energy in the buffer layer near the wall. Also, the streamwise fluctuations, u' , are much larger than the spanwise fluctuations v' .



(a) Instantaneous streamwise velocity fluctuations calculated using CRW model.



(b) Instantaneous spanwise velocity fluctuations calculated using CRW model.



(c) Grid distribution in the 2D channel.

Figure 3.3 Reconstruction of the velocity fluctuations using Langevin stochastic equations (Eq. 3.8). On the left the contours of velocity fluctuations and on the right their magnitude on the center-line of the cross section passing the middle of channel are shown.

The grid distribution in the channel is shown in Figure 3.3 (c). It is seen that the grid is staggered and the grid size is increasing with their normal distance from the walls. The maximum cell size is at the center of the channel.

The root mean-square turbulent velocity fluctuations evaluated from the CRW model over 0.29 s is compared with the corresponding square root of the $\overline{u'_1 u'_1}$ and $\overline{u'_2 u'_2}$ (Reynolds stresses over density) predicted by RSTM in Figure 3.4 to check the validity of the numerical solution of the Langevin stochastic differential equation. It is seen that the predicted streamwise and spanwise velocity fluctuations have large magnitude close to the walls that decrease toward the center of the channel. Figure 3.4 shows the CRW model is consistent with the RSTM turbulence model.

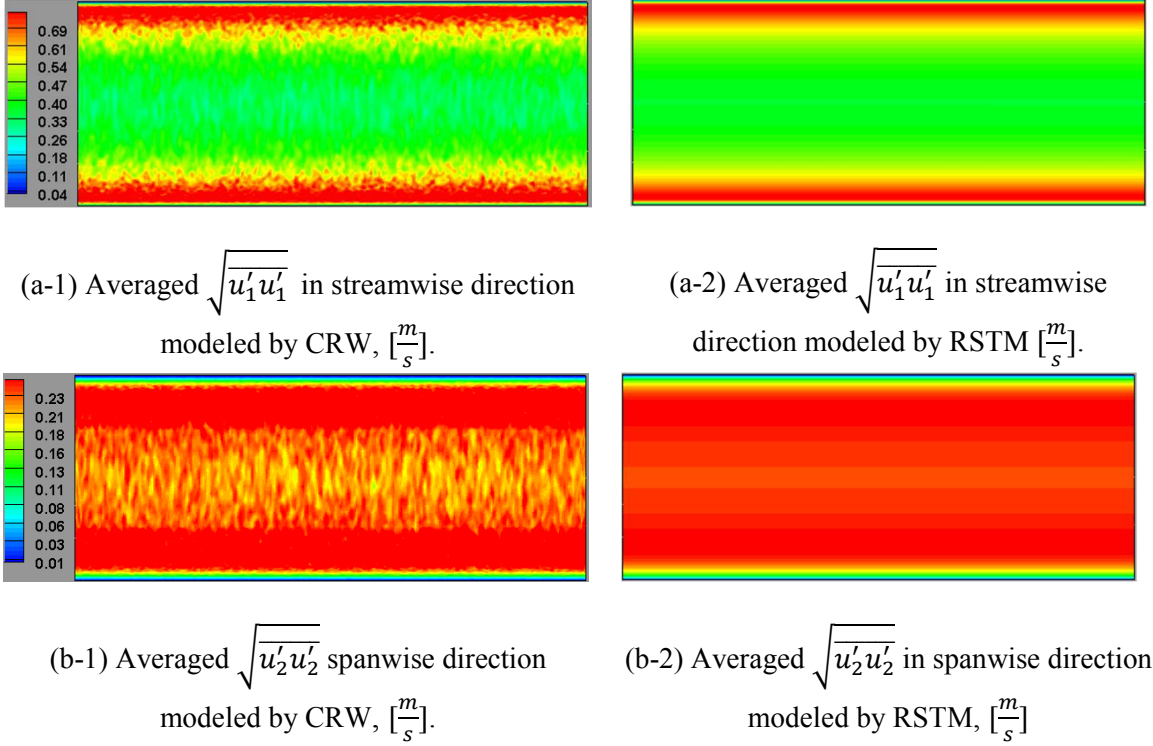
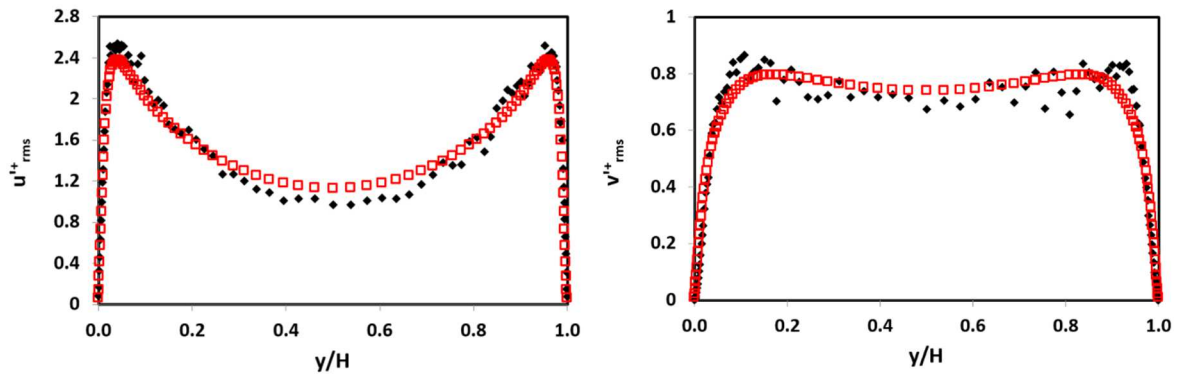


Figure 3.4 Comparison of the root mean-square velocity fluctuations modeled through CRW and the square root of the time averaged Reynolds stress from RSTM.

The non-dimensional profiles of RMS of velocity fluctuations from CRW, $u'_{rms} = \frac{\sqrt{u'_1 u'_1}}{u^*}$

and $v'_{rms} = \frac{\sqrt{v'_1 v'_1}}{u^*}$ at a line crossing the mid-channel are compared with the corresponding values predicted by RSTM in Figure 3.5. It is seen that the velocity fluctuations generated by the stochastic Langevin equation, are consistent with the turbulence model predictions.



Comparison of normalized RMS u'^+ predicted by CRW model and RSTM.

Comparison of normalized RMS v'^+ predicted by CRW model and RSTM.

Figure 3.5 Comparison of the profile of the normalized root mean square of the velocity fluctuations by CRW model, Equation (3.8), shown by black diamond marks, and RSTM turbulence model, which are red the square marks.

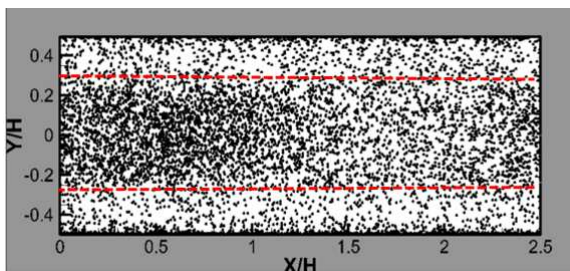
3.4.1.2 Particle distribution in a 2D channel flow

The particle distribution and deposition in the channel flow is investigated including the effect of turbulence velocity fluctuations on particle dispersion. In addition, the effects of Brownian motion, Saffman lift force and are considered in the particle transport equation. The effect of gravity force is considered in the horizontal channel. 100,000 particles are injected uniformly at the channel inlet which has a height of 2 cm. When particles reach a distance to the wall equal to their radius, it is assumed that they deposit on the wall and are removed from the computational domain. Dispersion and deposition of particles with sizes of 1.5, 2, 3, 4, 5, 7, 10, 15, 25, 30 and 50 μm are studies. Since the periodic boundary condition is used, the particles exiting from the outlet (on the right) will enter the channel from the inlet (on the left). In Figure 3.6 the number distribution of particles in sizes of 3 μm and 30 μm at 0.2 s after the injection from inlet in the vertical and horizontal channels are shown. Pictures on the left, represent the particles distribution in

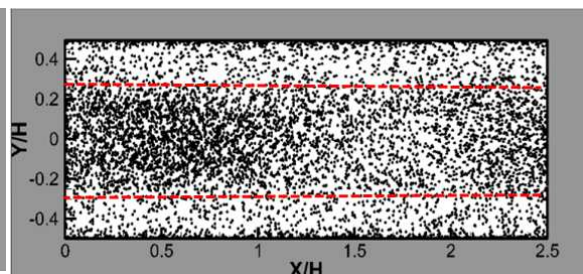
the vertical and figures on the right represent the horizontal channel. In this figure red lines separate the regions where the number concentration of particles are 80% greater than the rest of the channel, identified by image processing using Image-J software.

In the vertical channel, both 3 μm and 30 μm particles have high concentrations in the central region of the channel. In the region outside the red lines the 3 μm particles accumulated close to the walls, while the concentration of 30 μm particles is smaller due to their high deposition rate over 0.2 s. Particles with diameter of 30 μm deposit at higher rates than the 3 μm particle, because the effect of turbulent eddy – impaction process is stronger for larger particles.

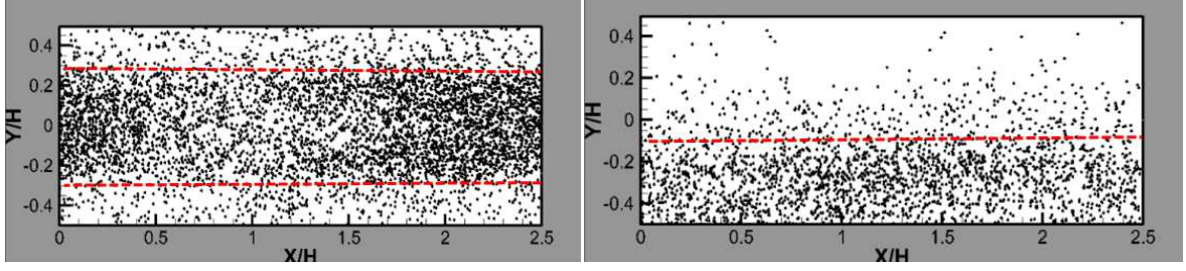
In horizontal channel gravity is downward and normal to the lower wall. Comparing the concentration distribution of particles shows that the gravity force has accumulated the larger particles in lower half of the channel. However, the concentration distribution of 3 μm particles in the horizontal channel is mostly similar to the vertical channel, which shows the gravity did not significantly affect these particles due to their small size, and still the main mechanism of dispersion is the turbulent diffusivity.



(i-1) 3 μm particles in the vertical channel



(ii-1) 3 μm particles in the horizontal channel



(i-2) 30 μm particles in the vertical channel. (ii-2) 30 μm particles in the horizontal channel.

Figure 3.6 Comparison of particle distribution in the vertical (left) and horizontal channel flow for particles in sizes of 3 μm (top) and 30 μm (bottom).

The accuracy of the particle transport model is evaluated by comparing the deposition velocity of particles predicted in the numerical model in the vertical and horizontal channel flows with the available numerical and experimental data.

The non-dimensional deposition velocity of particles is given as,

$$u_d^+ = \frac{J}{C_0 u^*} \quad (3.18)$$

J is the particle mass flux to the wall per unit time, C_0 is the particles initial concentration and u^* is the shear velocity. Dehbi (2008) calculated the deposition velocity of particles in a pipe of diameter D and length L in which particles are injected from the whole cross section of the pipe as,

$$u_d^+ = \frac{1}{4} \frac{D \bar{U}}{L u^*} \ln\left(\frac{N_{in}}{N_{out}}\right) \quad (3.19)$$

Here the channel height is replaced by D and \bar{U} is the bulk velocity. N_{in} and N_{out} are, respectively, the number of particles injected and exited the domain. Since periodic boundary condition is used in this study, $\frac{\bar{U}}{L} = \frac{1}{t_t}$, where the t_t is the time duration that

particle trajectory was analyzed. $N_{out} = N_{in} - N_d$, where N_d is the number of particles deposited. The non-dimensional particle relaxation time is given as $\tau^+ = \frac{\tau u^{*2}}{\nu} = \frac{s_p d_p^2 u^{*2}}{18\nu^2} C_c$.

The quadratic variation of normal velocity fluctuation as given by Equation (3.10), and the Lagrangian time scales near the wall as given by Equation (3.12) are included in the “User Defined Function” added to the ANSYS Fluent 12.1 software. Also, the two-layer wall boundary condition is used for more accurate evaluation of the velocity profile close to the wall. The continuous random walk model is applied using the Langevin equation given by Dehbi (2008), and the turbulent velocity fluctuations are generated for each particle individually. It should be emphasized that the flow field and particle transport equations are modeled using transient flow assumption.

The non-dimensional deposition velocity of particles, u_d^+ , for sizes covering transition to inertial regions $0.15 < \tau^+ < 550$ is presented in Figure 3.7 and Figure 3.8. The simulation results are compared with the 2D, RSTM channel flow provided by Tian and Ahmadi (2007) for both vertical and horizontal channel flows. They applied discrete random walk (DRM) model of ANSYS Fluent to model turbulent fluctuations and the standard wall function (STW) for the near wall velocity profile. The corresponding results in the Figure 3.7 and Figure 3.8 are denoted as RSTM, STW & DRW. Also, in their in-house PARTICLE code for tracking particles, they considered the two-layer zonal near wall condition and quadratic variation of the normal velocity fluctuation with the distance from walls. In their code they generated turbulent fluctuations using

continuous random walk (CRW) model, and their results are denoted in figures as Tian and Ahmadi_CRW.

The difference between the current model and the earlier Tian and Ahmadi_CRW is that here a subroutine is added to the CFD software, so a transient solution can be conducted for both particle transport and fluid phase simultaneously, which is important for the CFD analysis of particles in complex geometries.

In addition, the empirical equations of Wood (1981), and Fan and Ahmadi (1993), the simulation results of Li and Ahmadi (1993) and He and Ahmadi (1999), the DNS of McLaughlin and the experiments of Papavergos and Hedley (1984) for deposition velocity of particles in a vertical channel flow are reproduced in Figure 3.7.

As shown in Figure 3.7, the deposition velocities calculated by current transient RSTM turbulence model and by considering CRW model, denoted as RSTM and CRW model, in the vertical channel flow, follows the V-shaped curve of the deposition velocity of particles. The results of RSTM and CRW model agree well with the earlier experimental data and numerical simulation results. Small particles with the nondimensional relaxation time, τ^+ , of order 1 have the lowest rate of the deposition velocity ($u_d^+ \sim O(10^{-5})$), because of their low Brownian motion and inertia. The deposition velocity increases by increasing the particle sizes. When particle sizes reach $\tau^+ > 100$ the curve of deposition velocity flattens at $u_d^+ \sim O(0.1)$. Tian and Ahmadi (2007) showed that the RSTM model with standard wall function and DRW turbulent fluctuation model over-predicts the deposition velocity of particles in a vertical channel, and it is not able to capture the V-Shaped curve of the particle deposition.

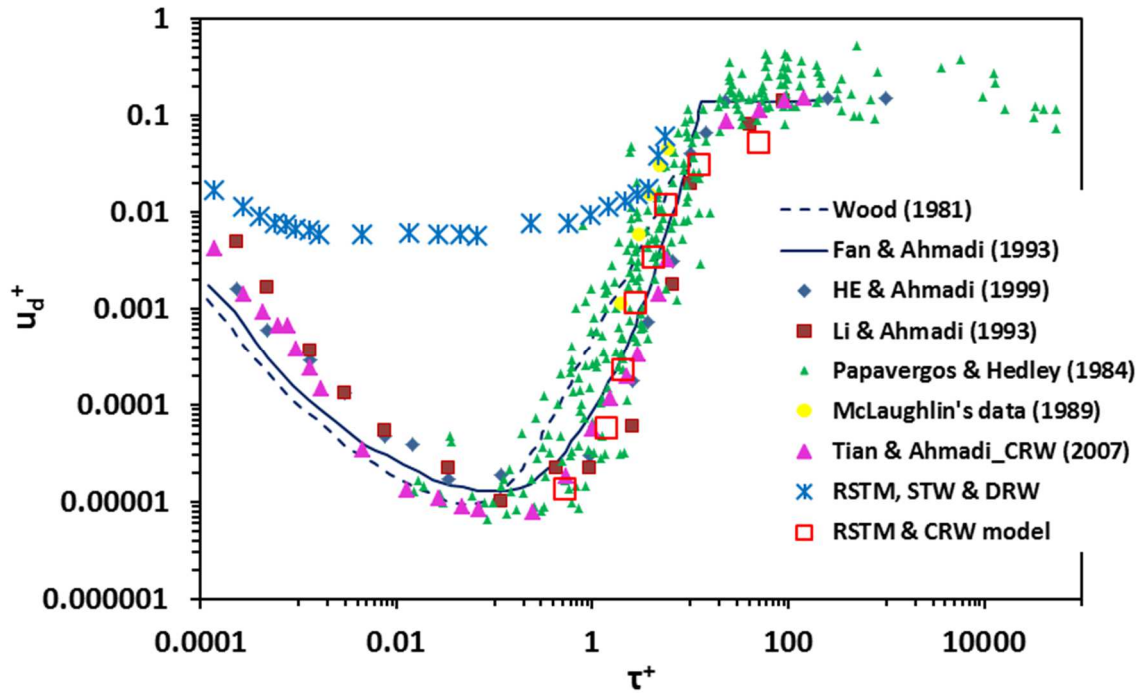


Figure 3.7 Deposition velocities of particles in a vertical channel, comparison of the current simulation (RSTM and CRW model) with previous experimental and numerical data.

in Figure 3.8 the accuracy of the deposition velocity predicted by RSTM, DRW model in a horizontal channel flow is evaluated by comparing the results with the empirical equations developed by Wood (1981), and Fan and Ahmadi (1993), and the experimental data of Montgomery and Corn (1970), Sehmel (1970) and Kvasnak et al. (1993), and also with the simulation results of Tian and Ahmadi (2007). The RSTM with CRW and two layer near wall velocity predicts the deposition velocities consistent with the Tian and Ahmadi (2007) simulation and other experimental data. The nondimensional deposition velocity of particles in transient regime ($\tau^+ \sim (1)$) in the horizontal channel, $u_d^+ \sim O(10^{-3})$, is much higher than that of the vertical channel, $u_d^+ \sim O(10^{-5})$, which is due to the effect of gravity on particles sedimentation. According to Tian and Ahmadi (2007), the deposition velocity of particles especially in small sizes is over-estimated by the DRW model because of the generation of large turbulent fluctuations by the DRW model.

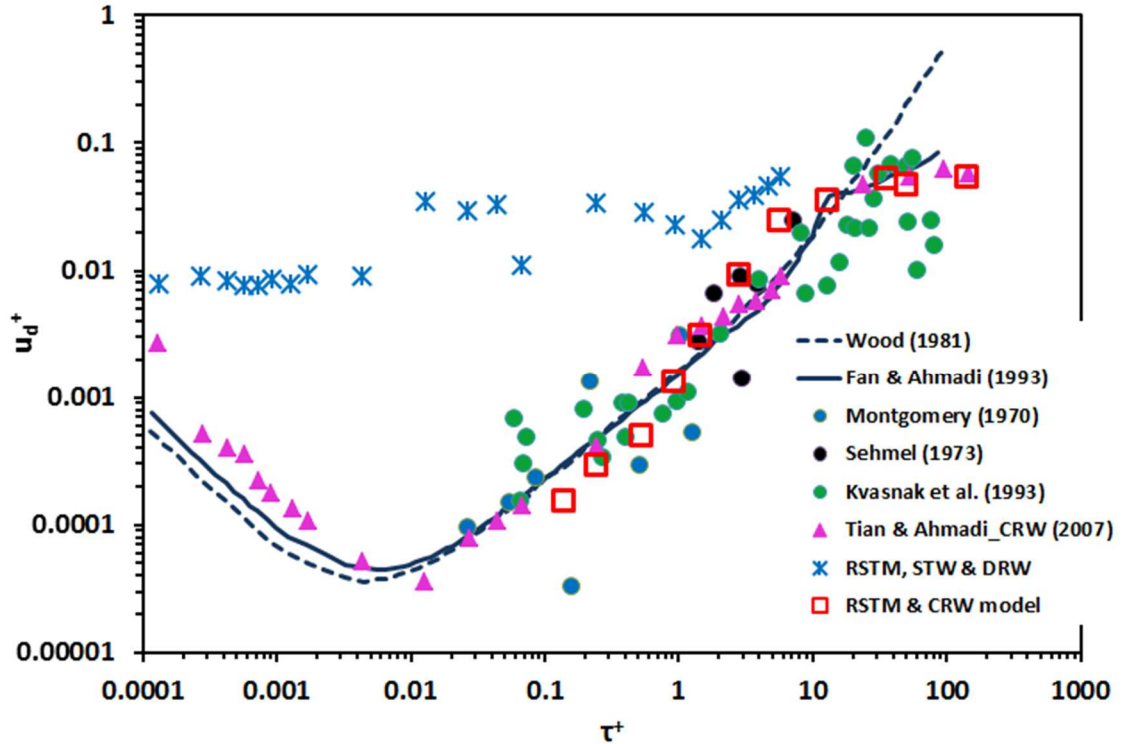
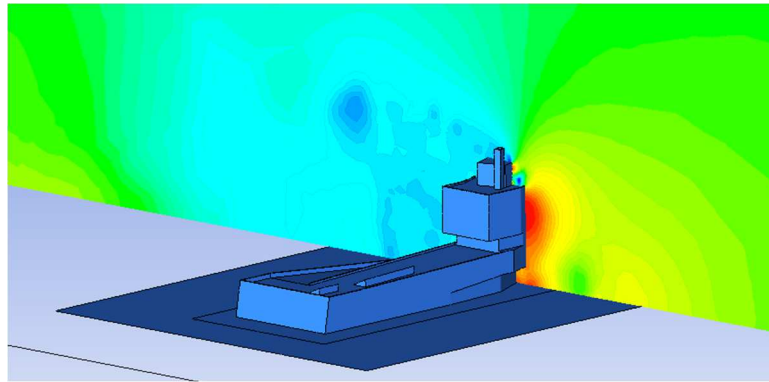
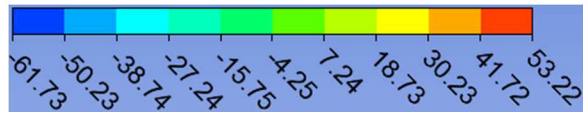


Figure 3.8 Deposition velocities of particles in a horizontal channel, comparison of the current simulation, (RSTM and CRW model) with previous experimental and numerical data.

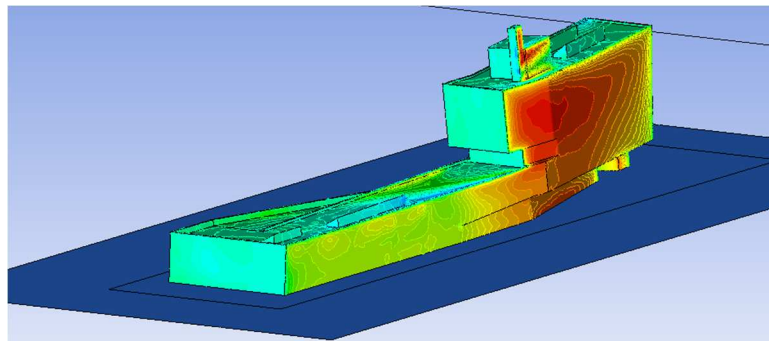
3.4.2 Particle deposition on the CoE Building model

Since the CoE Building is located at intersection of two major high ways, a series of studies are conducted to predict the deposition of particulate pollutants on several parts of the building. The outcome of the study would helpful to place the air intake of the building air-handling system, and to provide information on which rooms in the building may benefit from natural ventilation to save energy without concern about added air pollution.

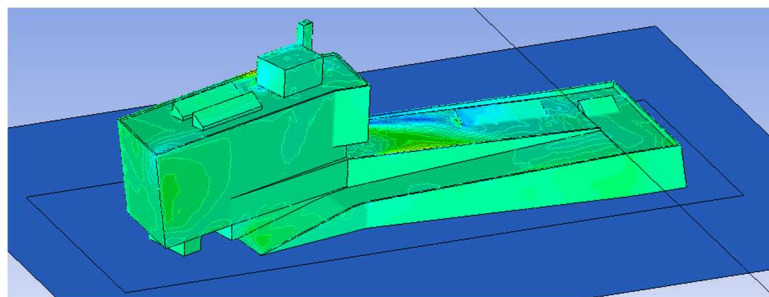
As was noted in Chapter II, the LES approach provided better details of the complex airflow field around the building that agreed with the PIV experimental data. Here the airflow is modeled using LES with dynamic kinetic energy subgrid scale model.



(a) Contours of pressure along a plane perpendicular to the building.



(b) Contours of the pressure on the front façade.



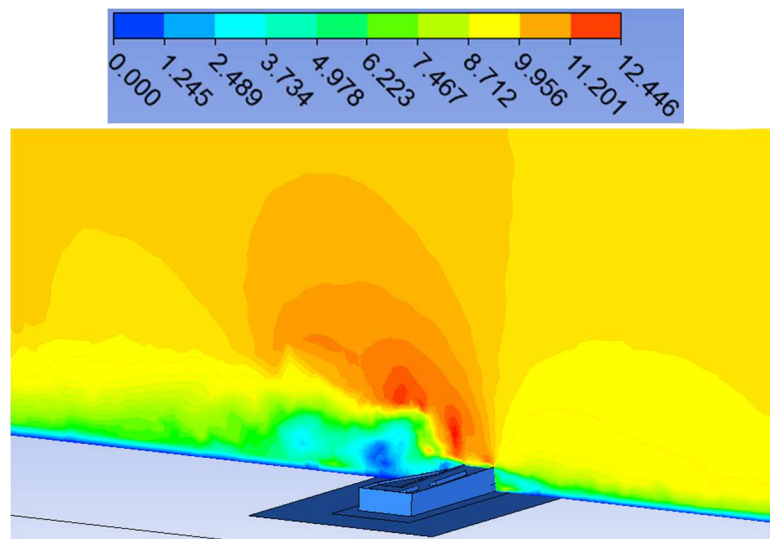
(c) Contours of pressure on the back side walls.

Figure 3.9 Pressure distribution around the building (a) pressure on a cross section passing the high rise section of the building (b) pressure on the front façade of the building (c) pressure on the back walls of the building.

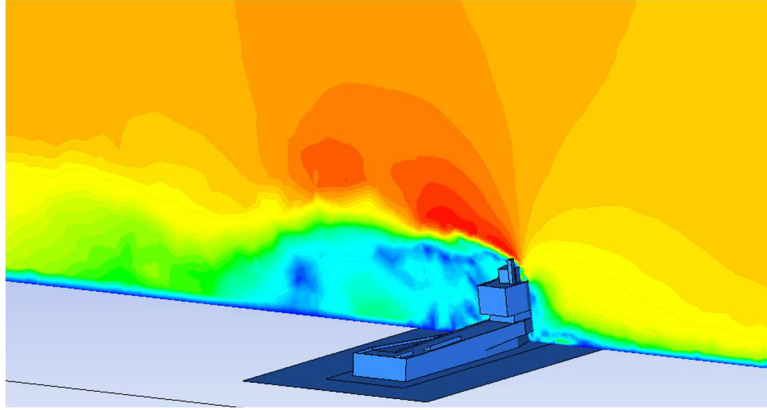
The case with wind velocity of 10 m/s perpendicular to the largest dimension of the building model is simulated. The corresponding Reynolds number based on the building height of 0.12 m is 81,200.

Contours of pressure on a plane crossing the building as well as on the walls in front and at the back side of the building calculated by LES are shown in Figure 3.9. The negative gauge pressure on the walls at the top and back side of the building model correspond to the recirculation zones. High wind pressure is exerted on the front façade of the building model (front with respect to the wind direction).

The velocity contours on two cross sectional planes one passing through the low-rise section of the building and the other one crossing the high-rise section are shown in Figure 3.10. The complexity of the geometry of the building model makes the wind flow field around it even more complicated. The flow separation at the leading edge and flow vortices at the back side is much more intense at the high-rise section of the building model rather than the low-rise one.



(a) Velocity contours on plane (I) crossing the low rise section of the CoE Building.



(b) Velocity contours on plane (II) crossing the high rise section of the CoE Building.

Figure 3.10 The contours of instantaneous velocity magnitudes along two planes crossing the CoE building.

Particles are tracked considering two layer zonal near wall condition and continuous random walk model (CRW). In CRW, fluctuations are modeled using Langevin stochastic equation given by Pozorski and Apte (2009). Also, Brownian motion, Saffman lift force and gravity force are considered in the particles transport equation.

The generated velocity fluctuations from Langevin equation are added to the resolved (large scale) velocity of the fluid modeled by LES, $(\tilde{u}^f + u'^f)$. The difference of the instantaneous flow velocity and the particle velocity, u^p , are used in the particle transport equation given by (3.1).

The velocity fluctuations are modeled for each particle separately, and the above mentioned procedure is repeated at the location of every single particle at each particle time step. The deposition velocity of particles on the walls of the CoE Building model is calculated using Equation (3.20).

Particles are considered spherical, and in diameter sizes of 1, 3, 5, 7 and 10. The particle-to-fluid density ratio is $S = 2000$. The schematic of the plane which the particles are injected from, and the locations where deposition velocity of particles is calculated are

shown in Figure 3.11. The injection plane is located upstream the building model at 0.22 m distance and its size covers the maximum height and length of the building. Also, particles are injected in a distance from the ground equal or greater than their diameter size to prevent the unreasonable deposition. The vertical gap between each particle at injection plane is 0.5 mm.

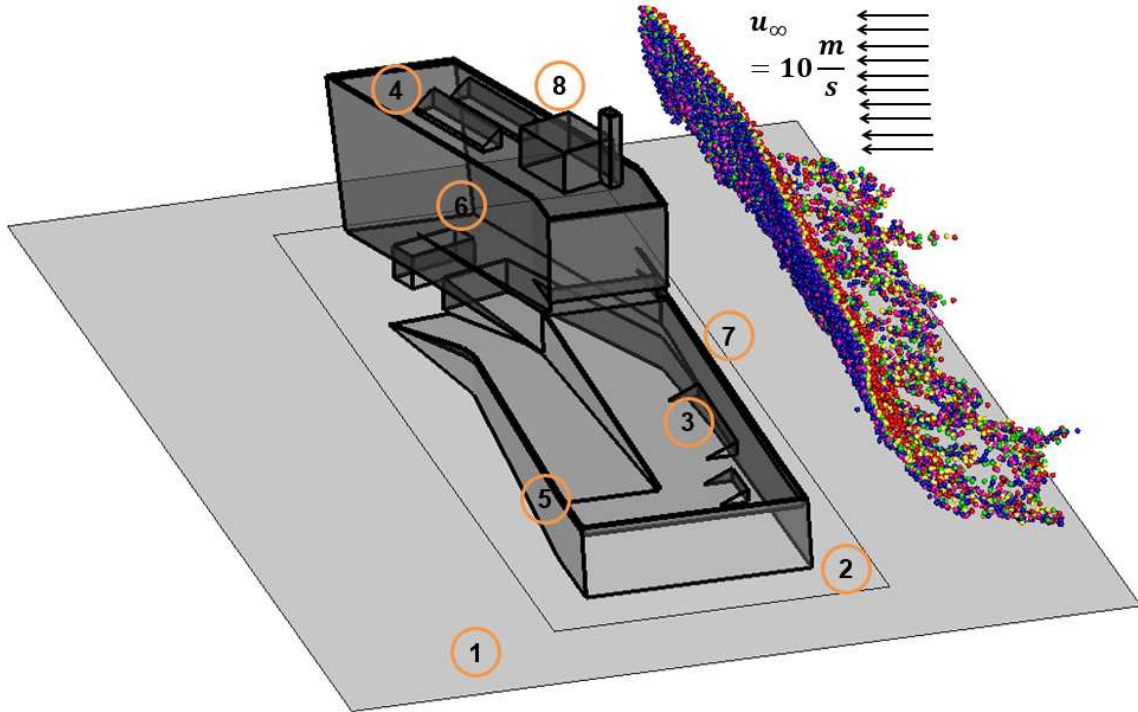


Figure 3.11 The injection plane upstream the model of the CoE Building, the local deposition rate of particles on 8 positions on the walls of the building is calculated.

Based on Equation (3.18) the non-dimensional deposition velocity of particles on the walls of the CoE building is calculated as,

$$u_d^+ = \frac{J}{u^* C_0} = \frac{\frac{N_d}{dt A_d}}{u^* \frac{N_0}{A_0 v_0 dt}} = \frac{1}{u^*} \frac{N_d v_0 A_0}{N_0 A_d} \quad (3.20)$$

Where N_d is the number of particles deposited on the area of A_d , the N_0 is the number of particles injected from the plane with the area of A_0 , and v_0 is the velocity of injection. To non-dimensionalize the deposition velocity the expression is divided by the shear velocity, u^* , which is averaged over the wall area under study.

The local deposition velocity of particles on 8 different areas surrounding the CoE Building model is presented in Figure 3.12.

Maximum deposition velocity of particles is seen on the front façade of the building which faces the wind stream, and also, on the ground attached to the upstream walls. The separation of the particles from the wind main-stream and their impact to the front wall causes the high deposition rates at this area. Also, the recirculation region at the lower level of the front façade shown in Figure 3.9 and the high turbulent velocity fluctuations identified by the turbulent kinetic energy shown in Figure 3.13 are the reasons of high deposition velocity on the ground close to the front walls. The high deposition rate of particles on the ground around the building shows the importance of studying the particle resuspension for calculating the pollution intake into the building. In charts 1, 2, 7 and 8, particles with lowest inertia have smallest deposition velocity, and the ones with highest inertia deposit the most.

At the backside of the building the total deposition velocity is 10 times smaller than the front façade. Charts 5 and 6 show the low deposition velocity of particles at back side of the building.

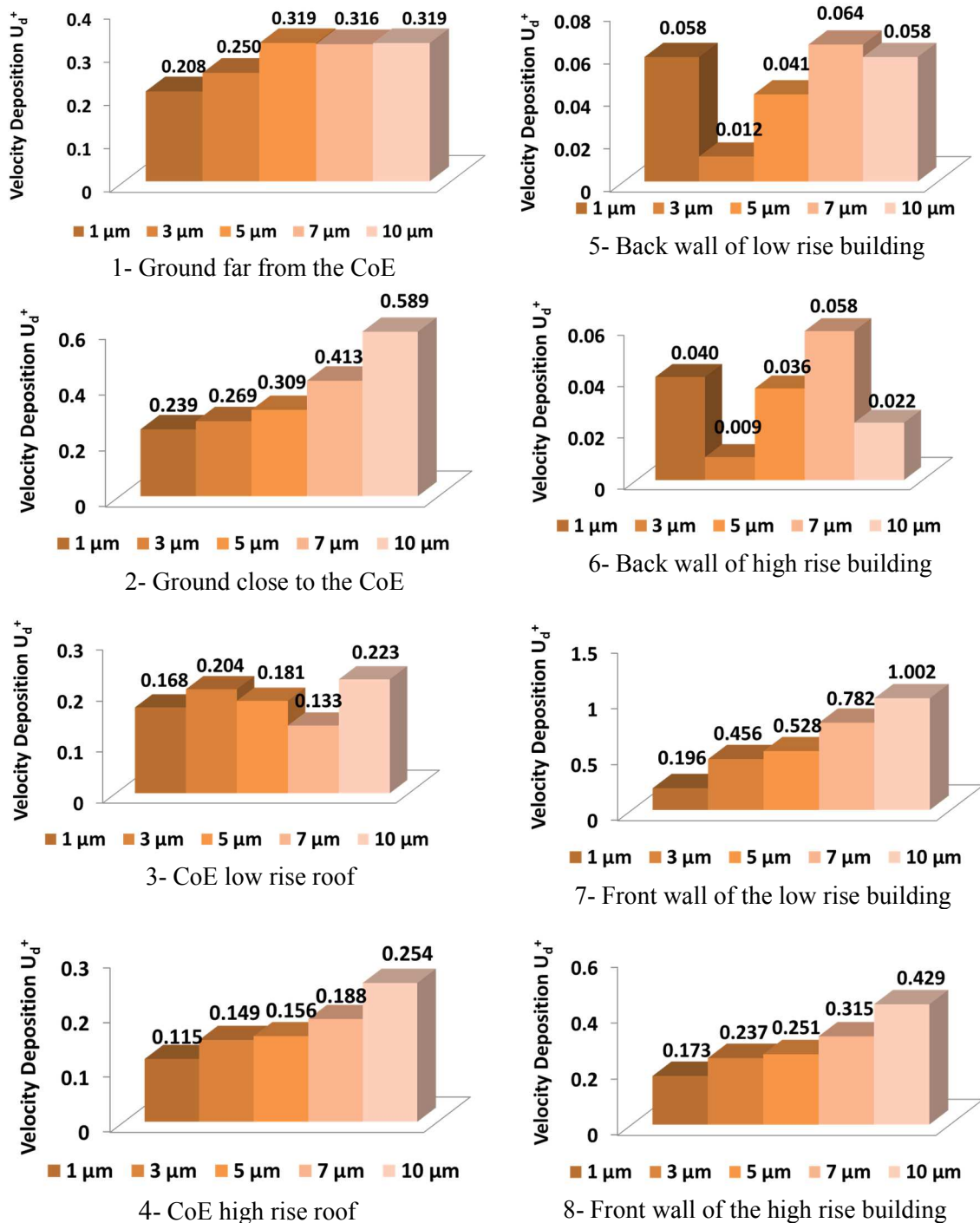


Figure 3.12 local deposition rate of particles on (1) the ground far from the CoE building, (2) the ground close to the building (3) the roof in low-rise section (4) the roof in high-rise section (5) the back wall of the low-rise section (6) the back wall of the high rise section (7) the front wall of the low-rise section (8) the front wall of the high-rise section.

The recirculation region and the high intensity of turbulent fluctuations at the back side of the building cause disordered deposition rates for the particle sizes under study.

The subgrid scale turbulent kinetic energy, modeled by Equation (3.17), around the building is shown in Figure 3.13. The highest turbulent kinetic energy is predicted at the separation points, at the intense recirculation region at the back side of the obstacle, and at the small recirculation region at the lower level of the front walls.

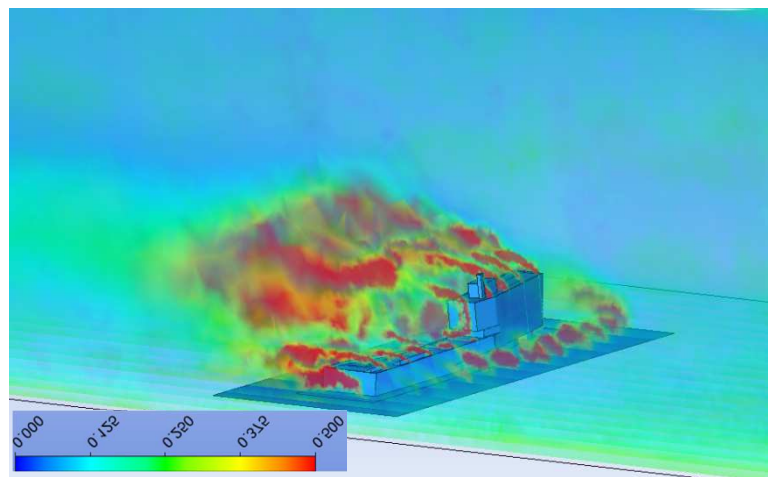


Figure 3.13 The subgrid scale turbulent kinetic energy modeled in LES.

The deposition velocity of particles on the roof of the building is relatively high (Chart 3 and Chart 4). Regarding Figure 3.13 the subgrid scale turbulent kinetic energy is high in this region which leads to the high turbulent velocity fluctuations. The combination of the turbulent fluctuations and the recirculation regions on the top side of the building causes the deposition of particles on the roof.

3.5 Conclusions

The turbulent velocity fluctuations are modeled through a Continuous Random Walk model using Langevin stochastic equation. The deposition velocity of particles in a wide range of 1.5 μm to 50 μm was captured in 2D horizontal and vertical channel flows. The Brownian motion, gravity and Saffman lift force beside the drag force induced from the reconstructed instantaneous turbulent velocity of fluid are considered in the particle transport equation. Also, near wall boundary layer corrections including enhanced wall treatment and quadratic variation of normal fluctuations are applied for study of particles in the channel flow. The comparison of the deposition velocity of particles with previous numerical and experimental data, showed a significant modification in calculating the deposition velocity of particles in ANSYS Fluent software.

The numerical model reconstructs the velocity fluctuations for each particle at each of its time steps. Therefore, two particles in the same computational cell may face different velocity fluctuations. Of course, fluctuations are the functions of the turbulent features in the domain. The progress of this model with respect to the Code developed by Lian and Ahmadi (2007) is that the current model is added to a user defined function, so the particle transport can be solved for a transient flow. For particles in a turbulent flow over a bluff body with complex geometry, it is important to be tracked simultaneously with the flow field.

Also since no subgrid scale velocity fluctuation for LES is available in ANSYS Fluent 12.1, a continuous random walk (CRW) model is developed to predict the subgrid scale fluctuations in LES. Particle distribution and deposition over the CoE building model are

tracked simultaneously with the airflow simulation using LES. The local deposition velocity of particles in size range of 1 μm to 10 μm over the building area is analyzed in the charts. Highest deposition rates occur on the front façade of the building and the ground attached to that, which is due to particle impaction and recirculation region at the bottom side of the wall. The lowest particle concentration is expected to be on the walls on the opposite side of the source of pollution. On the top side of the building the subgrid scale turbulent kinetic energy is high, leading high rate of particles deposition. Therefore, an accurate model of velocity fluctuations is necessary for predicting particles deposition and concentration in this region.

According to the presented simulation results and based on the concentration of the source of pollution, the rooms at the back side of the building are the best choices for using natural ventilation for saving energy. Also, it is suggested to put the air inlet of the Air Handling System in this region to prevent the pollutants from northern highway intake into the building. At separation and recirculation regions, where the highest turbulent kinetic energy exists, considering the SGS turbulent fluctuations improves the predictions of particles diffusion and deposition.

References

- Chen, H. C., and Patel, V. C., (1988). "Near-wall turbulence models for complex flows including separation." *AIAA J.*, 26, 641–648.
- Dehbi, A. (2008). "Turbulent particle dispersion in arbitrary wall-bounded geometries: a coupled CFD-Langevin-equation based approach." *Int.J.Multiphase Flow*, 34(9), 819-828.
- Dreeben, T. D., and Pope, S. B. (1997). "Probability density function and Reynolds-stress modeling of near-wall turbulent flows." *Physics of Fluids (1994-Present)*, 9(1), 154-163.
- Fan, F. G., and Ahmadi, G. (1993). "A sublayer model for turbulent deposition of particles in vertical ducts with smooth and rough surfaces." *J.Aerosol Sci.*, 24(1), 45-64.
- He, C., and Ahmadi, G. (1999). "Particle deposition in a nearly developed turbulent duct flow with electrophoresis." *J.Aerosol Sci.*, 30(6), 739-758.
- Kader, B., (1981). "Temperature and Concentration Profiles in Fully Turbulent Boundary Layers." *Int. J. Heat Mass Transfer*, 24(9), 1541-1544.
- Kim, W., and Menon, S. (1997). "Application of the localized dynamic subgrid-scale model to turbulent wall-bounded flows." *AIAA Paper*, 97-0210.
- Kvasnak, W., Ahmadi, G., and Schmidt, D. J. (2004). "An engineering model for the fuel spray formation of deforming droplets." *Atomization and Sprays*, 14(4).
- Li, A., and Ahmadi, G. (1992). "Dispersion and deposition of spherical particles from point sources in a turbulent channel flow." *Aerosol Science and Technology*, 16(4), 209-226.
- Li, A., and Ahmadi, G. (1993). "Deposition of aerosols on surfaces in a turbulent channel flow." *Int.J.Eng.Sci.*, 31(3), 435-451.
- McLaughlin, J. B. (1989). "Aerosol particle deposition in numerically simulated channel flow." *Physics of Fluids A: Fluid Dynamics*, 1 1211.
- Mito, Y., and Hanratty, T. J. (2002). "Use of a modified Langevin equation to describe turbulent dispersion of fluid particles in a channel flow." *Flow, Turbulence and Combustion*, 68(1), 1-26.
- Montgomery, T. L., and Corn, M. (1970). "Aerosol deposition in a pipe with turbulent airflow." *J.Aerosol Sci.*, 1(3), 185-213.
- Papavergos, P., and Hedley, A. (1984). "Particle deposition behaviour from turbulent flows." *Chemical Engineering Research and Design*, 62(5), 275-295.

Pozorski, J., and Apte, S. V. (2009). "Filtered particle tracking in isotropic turbulence and stochastic modeling of subgrid-scale dispersion." *Int.J.Multiphase Flow*, 35(2), 118-128.

Tian, L., and Ahmadi, G. (2007). "Particle deposition in turbulent duct flows-- comparisons of different model predictions." *J.Aerosol Sci.*, 38(4), 377-397.

Wood, N. (1981). "A simple method for the calculation of turbulent deposition to smooth and rough surfaces." *J.Aerosol Sci.*, 12(3), 275-290.

CHAPTER IV. Indoor secondary organic aerosols formation- Computer modeling of coagulation, surface growth and nucleation

Abstract

Typical furniture inside residential or office buildings is made from materials that emit terpenes, which are highly reactive with ozone in the air (Sarwar et al. 2003; Weschler 2000) and produce Secondary Organic Aerosols (SOAs). Secondary Organic Aerosols (SOAs) are nonvolatile and their high concentration could adversely influence human health. During the summer the concentration of SOAs in indoor environments may exceed by a factor of two to five times of that in other seasons (Weschler, 2000).

In this Chapter, a computer model for evaluating the concentration of secondary organic aerosols in indoor environment was developed. Chen and Hopke (2009 a, b) performed a series of experiments on secondary aerosol formation in a mixing chamber. Terpenes and ozone were injected into the mixing tank at constant rates. The air inside the chamber was well mixed with the aid of two fans, and a constant rate of air exchange for the mixing chamber was imposed. Chen and Hopke (2009 a, b) measured the number size distribution of the SOAs produced from the reaction of terpenes and ozone in the tank. Their data are used for verification of the developed computer model.

Three mechanisms are considered to affect the distribution of number size concentration of SOAs. From the reaction of terpene materials with ozone nonvolatile aldehyde gases are produced. When their concentration increases, their partial pressure eventually reaches the saturation pressure, and then the secondary organic aerosols (SOAs) are nucleated. The nonvolatile aldehyde gases, also, condense on the surface of the existing SOAs, which leads to the surface growth of the particles. In addition, the particles collide and coagulate due to their Brownian motions as well as turbulent airflow fluctuations. The SOAs nucleation, coagulation and surface growth in a homogeneous gas-particle mixture were numerically simulated using Method of Moments (MOM). In the method of moments, the shape of the distribution of particles is assumed, and the final number concentrations are evaluated from the moment equations. Finally, the simulation results were compared with the experimental data reported by Chen and Hopke (2009 a, b) for model verifications.

The method of moments was applied to simulate the concentration distribution of SOAs in a typical office space. The office included a model of a manikin seated behind a desk, a desktop PC on the desk and some furniture. The furniture was the source for emitting α -pinene, which reacts with ozone and creates the SOAs. The indoor airflow was simulated for two ventilation systems, and the particle number distributions were predicted, using the method of moments (MOMs). The ventilation airflow in the room and the Brownian motion caused the particle coagulation that led to the decrease of concentration of small particles and increase of the concentration of large particles. Also, the surface growth of particles led to increasing the size of particles. The air flow was laminar and the effect of turbulent fluctuations on particles collision was neglected.

Keywords: Particulate air pollutants; Air Ventilation; Method of Moments; Secondary Organic Aerosols; Indoor air.

4.1 Introduction

The initial particle concentration and the nucleation rate in the numerical model were set based on the data from the experiment of Chen and Hopke (2009 a, b). The experiment conditions were designed so that the concentration of the reactive oxygen species (ROS) produced from the reaction of α -pinene and ozone was relevant with the typical indoor air pollution caused by SOAs. α -pinene and ozone were injected at constant rate into the mixing chamber. An air exchange rate of 0.67 h^{-1} for the chamber was also imposed. The mixing chamber was a rectangular tank with a volume of 2.48 m^3 and a surface to volume ratio of 4.5 m^{-1} . The air inside the chamber was well mixed by two fans to generate a homogeneous mixture of air and chemical species injected into the tank. The schematic of the experimental setup is shown in Figure 4.1.

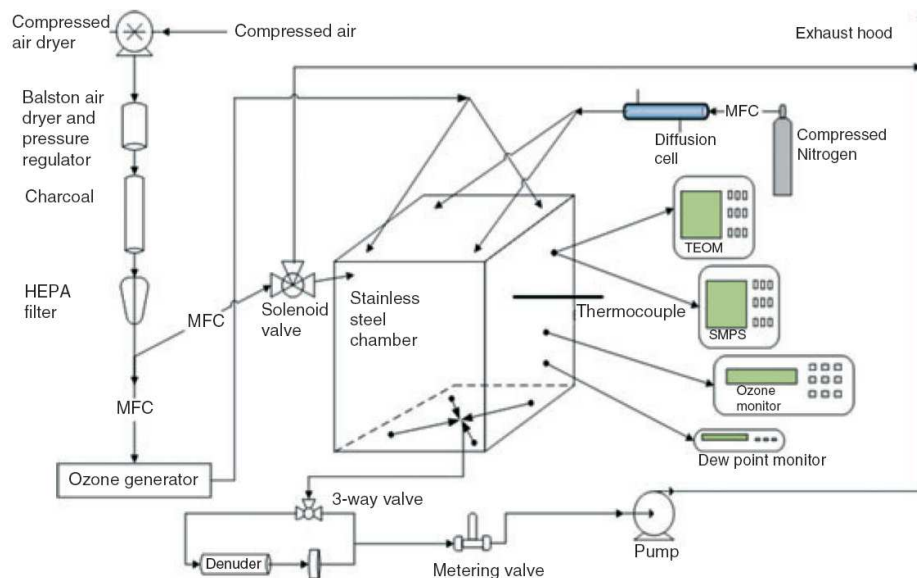


Figure 4.1 Experimental setup of Chen and Hopke (2009 a) with the stainless steel chamber.

Time series of SOA number concentration, volume concentration, and mass concentration, as well as, ozone concentrations as reported by Chen and Hopke (2009 a) are shown in Figure 4.2. The experiment was conducted for 21 hours. For 10 hours the chemical components were injected into the chamber and the air inside the chamber was exhausted continuously. About 1 h after the injection of α -pinene into the chamber, a nucleation burst of SOAs was occurred (blue marks at $t = 1$ h). Initially the collision rate of particles was quite low because of the dilute particle concentration. After about 7 h, the number size concentration of particles reached to a steady state condition (Chen and Hopke 2009 a). The chamber was kept under the steady state condition due to the balance between injection rate of chemical components, which led to SOA formation, and the exhaust rate of the mixture air.

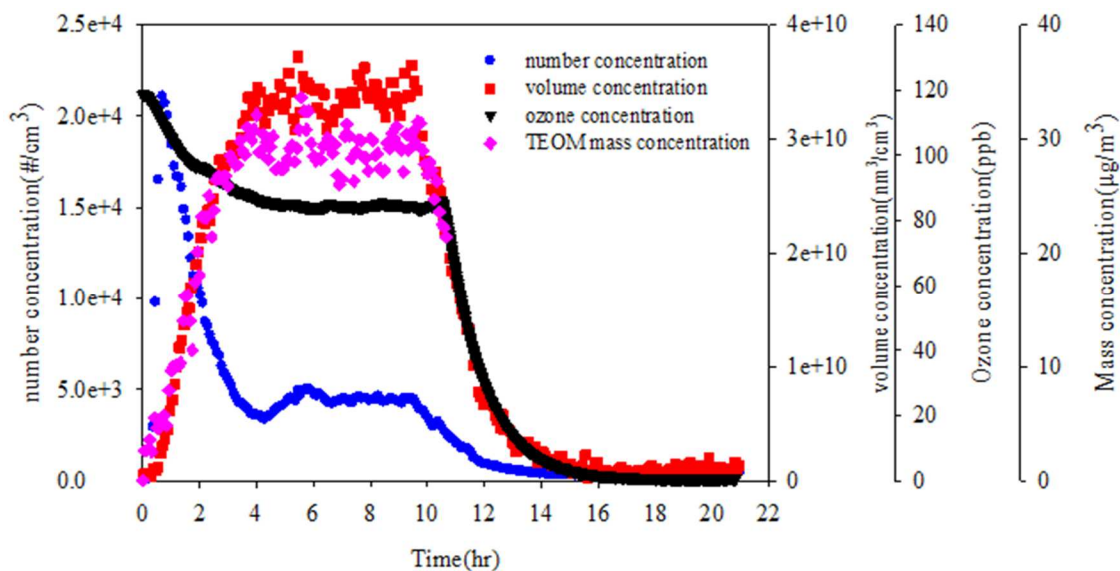


Figure 4.2 Time series of SOA number concentration, volume concentration, mass concentration and ozone concentration in the experiment of Chen and Hopke (2009a).

The concentration of particles in the chamber was in the steady state condition for about 2 h. The concentration distribution of SOA with respect to the particle sizes was

measured in the steady state condition. After 9 h, the injection of the chemical components was stopped, and all generated SOA evacuated from the chamber over time.

The experimental measurement of the particle sizes was limited to the range of 14 nm to 700 nm. The number size distribution of SOA were measured by Scanning Mobility Particle Sizer (SMPS) (Chen and Hopke, 2009 a, b), using differential mobility analysis.

In the numerical model the population balance equations of SOAs were simulated in a single cell using the Method of Moments (MOMs). A lognormal size distribution, which exists in a wide range of aerosol systems (Heintzenberg, 1994), was assumed in this simulation.

In this paper the first three moments, M_0 , M_1 and M_2 are calculated with respect to the particles volume (Brown et al. (2006), Frenklach (2002), Suh et al. (2002), Park et al. (1998)). The moment equations are obtained by multiplying the population balance equation by v_p^k , where v_p is the particle volume and k is the moments order, and integrating over zero to the maximum volume captured in the experiment (700 nm). A spatially homogeneous particle ensemble with constant density is assumed. Therefore, for instance, when two particles with same sizes collide, the new particle will have a volume two times the volume of the original particles.

4.2 Governing Equations

4.2.1 Population balance equation

The ozone/ α -pinene oxidization produces ultrafine particles. The smallest diameter size of particles measured in experiment was 14 nm. The population distribution of particles

developed over time due to the particle nucleation, coagulation and surface growth. Smoluchowski (1917) presented a model for the population balance determining the number concentration of particles due to Brownian coagulations. The continuum form of the population balance equation (PBE) in a homogeneous field is given as,

$$\frac{\partial n(v,t)}{\partial t} = \frac{1}{2} \int_0^v \beta(v-v',v')n(v-v',t)n(v',t)dv' - \int_0^\infty \beta(v,v')n(v,t)n(v',t)dv' + S \quad (4.1)$$

where, n is the particle size distribution function, β is the collision frequency function or collision kernel constant, v is one of the particle's specifications which can be its volume, diameter or mass, and S represents the source terms for particle concentration, which includes the nucleation and the surface growth rate. The first two terms on the RHS of equation (4.1) develop size distribution due to the particle coagulation. The first term on RHS represents the birth rate of the particles, in size v , due to the collision of smaller particles, and the second term is due to the loss rate of particles of a given size caused by their collision with other particles. The collision frequency or collision kernel constant, β , is the coefficient determines particles collision due to their Brownian motion.

The particle size spectrum is divided into three regimes based on their Knudson number,

Kn. The Knudson number, $Kn = \frac{\lambda}{r_d}$, is defined as the ratio of the air mean free path, at

temperature T , over the particle radius. Ultra-fine particles with $Kn > 50$ are considered to be in free molecular regime, particles with $Kn < 1$ are in continuum regime, and particles in between with $1 < Kn < 50$ are in the transition regime.

The collision kernel of the Brownian motion for the particles in the free molecular regime ($Kn > 50$) is given as

$$\beta(v, v') = K_{fm} (v^{\frac{1}{3}} + v'^{\frac{1}{3}})^2 \sqrt{\frac{1}{v} + \frac{1}{v'}} \quad Kn > 50 \quad (4.2)$$

K_{fm} is the free molecular collision coefficient, $K_{fm} = \left(\frac{3}{4\pi}\right)^{\frac{1}{6}} \left(\frac{6k_B T}{\rho}\right)^{\frac{1}{2}}$, and k_B is the Boltzmann constant.

The Brownian collision kernel in continuum regime ($Kn < 1$) is given as,

$$\beta(v, v') = K_{co} (v^{\frac{1}{3}} + v'^{\frac{1}{3}})^2 \left(\frac{C(v)}{v^{\frac{1}{3}}} + \frac{C(v')}{v'^{\frac{1}{3}}}\right) \quad Kn < 1 \quad (4.3)$$

K_{co} is the collision coefficient of fine particles, $K_{co} = \frac{2k_B T}{3\mu}$, where μ is the air molecular viscosity. $C(v)$ is the Cunningham slip correction factor, which has particularly high impact on calculating the collision kernel of nano particles. In order to simplify the integro-differential equation (4.1), it is assumed that $C(v) = 1 + A \cdot Kn$, which $A = 1.591$ (Lee and Hwang 1997; Lee et al. 1997). The source term, S , represents the nucleation and the surface growth of particles phase which are defined in the following sections.

4.2.2 Method of Moments (MOMs)

The PBE is a highly nonlinear integro-differential equation, the solution of which requires extensive computational resources, especially when a vast range of the particle sizes is under investigation. By using Method of Moments (MOM) the computation cost of modeling the population density distribution of SOAs is decreased significantly. To solve the moments equations, a lognormal Particle Size Distribution (PSD) is assumed.

The k^{th} moment of the particle size distribution, based on the integration over the k^{th} power of particle volume is defined as

$$M_k(t) = \int_0^{\infty} v'^k n(v', t) dv' \quad (4.4)$$

The lognormal particle size distribution was defined as,

$$n(v, t) = \frac{1}{3v} \frac{N(t)}{\sqrt{2\pi} \ln \sigma_g(t)} \exp\left(\frac{-\ln^2(v/v_g(t))}{18 \ln^2 \sigma_g(t)}\right) \quad (4.5)$$

In Eq. (4.5), $n(t)$ is particle size distribution density function, $N(t)$ is the total number of particles which is equivalent to the zeroth moment M_0 , $v_g(t)$ is the geometric mean of the particles volume, $v_g = \sqrt[n]{v_1 v_2 \dots v_n} = M_1^2 / (M_0^{1.5} M_2^{0.5})$ (Brown et al., 2006), and $\sigma_g(t)$ is the

geometric standard deviation based on particle radius, $\sigma_g = \exp\left(\sqrt{\frac{\sum_{i=1}^{i=n} (\ln \frac{r_i}{r_g})^2}{n}}\right)$, where

r_g is the geometric mean radius (Brock and Oates 1987; Lee 1983; Pratsinis 1988; Williams 1986).

By substituting the lognormal distribution given by equation (4.5) into (4.4) the k^{th} moment of particle volume is determined as

$$M_k(t) = \frac{N}{3\sqrt{2\pi} \ln \sigma_g} \int_0^{\infty} v'^{k-1} \exp\left(\frac{-\ln^2\left(\frac{v'}{v_g}\right)}{18 \ln^2 \sigma_g}\right) dv' \quad (4.6)$$

Consequently, the k^{th} -moments as the function of the geometric mean volume and standard deviation are given as (Park et al. 1999)

$$M_k = N v_g^k \exp\left(\frac{9}{2} k^2 \ln^2(\sigma_g)\right) \quad (4.7)$$

Note that, $M_0 = N$, $M_1 = Nv_g \exp(\frac{9}{2} \ln^2(\sigma_g))$ and $M_2 = Nv_g^2 \exp(18 \ln^2(\sigma_g))$. M_0 represents the total number concentration of particles N , M_1 is the total volume concentration of particles which by multiplying by particles density equivalents to the total mass concentration.

In this study the solution of the PBE is approximated by the first three moments of the particle size distribution.

4.2.3 Coagulation

The Brownian coagulation of particles in size range between free molecular and continuum regimes are given as (Lee 1983; Lee and Hwang 1997; Lee et al. 1997; Park et al. 1999; Whitby and McMurry 1997),

$$\left. \frac{dM_0}{dt} \right|_{fm} = -b \cdot K_{fm} (M_0 M_{\frac{1}{6}} + 2M_{\frac{1}{3}} M_{\frac{1}{6}} + M_{\frac{2}{3}} M_{\frac{1}{2}}) \quad \text{Kn} > 50 \quad (4.8)$$

$$\left. \frac{dM_2}{dt} \right|_{fm} = 2b \cdot K_{fm} (M_{\frac{7}{6}} M_1 + 2M_{\frac{4}{3}} M_{\frac{5}{6}} + M_{\frac{1}{2}} M_{\frac{5}{3}}) \quad \text{Kn} > 50 \quad (4.9)$$

$$\left. \frac{dM_0}{dt} \right|_{co} = -K_{co} [M_0^2 + M_{\frac{1}{3}} M_{\frac{1}{3}} + A\lambda (\frac{4}{3}\pi)^{\frac{1}{3}} (M_0 M_{\frac{1}{3}} + M_{\frac{1}{3}} M_{\frac{2}{3}})] \quad \text{Kn} > 1 \quad (4.10)$$

$$\left. \frac{dM_2}{dt} \right|_{co} = 2K_{co} [M_1^2 + M_{\frac{4}{3}} M_{\frac{2}{3}} + A\lambda (\frac{4}{3}\pi)^{\frac{1}{3}} (M_1 M_{\frac{2}{3}} + M_{\frac{4}{3}} M_{\frac{1}{3}})] \quad \text{Kn} < 1 \quad (4.11)$$

Equations (4.8) to (4.11) are derived by integrating the equation (4.1) times a property of a particle (which can be its diameter, mass or volume) to the power of k (the order of the moment), and substituting the corresponding coagulation kernel. In this study moments are calculated based on the volume of particles, assuming that when two particles collide

and coagulate, their masses and volumes add up in the new particle generated (constant density). The fractional-order moments are calculated using equation (4.7).

The Brownian kernel is known for the very small particles as well as for the large particles, but it is not well modeled for particles in sizes in between. In order to model the moment evolution of the particles with the spectrum size covering the free molecular ($Kn > 50$), transient ($1 < Kn < 50$) and continuum ($Kn < 1$) regimes, the harmonic mean of the series of moment equations are applied by Pratsinis (1988) as.

$$\frac{dM_0}{dt} = \frac{\frac{dM_0}{dt}\Big|_{fm} \times \frac{dM_0}{dt}\Big|_{co}}{\frac{dM_0}{dt}\Big|_{fm} + \frac{dM_0}{dt}\Big|_{co}} \quad (4.12)$$

$$\frac{dM_2}{dt} = \frac{\frac{dM_2}{dt}\Big|_{fm} \times \frac{dM_2}{dt}\Big|_{co}}{\frac{dM_2}{dt}\Big|_{fm} + \frac{dM_2}{dt}\Big|_{co}} \quad (4.13)$$

Since the concentration of the SOAs in the mixing chamber was dilute, the rate of the Brownian coagulation of particles was small. Thus, beside the Brownian coagulation, the nucleation and the surface growth of particles play an important role in the evolution of particle moments and size distributions. These sources are represented in PBE (4.1) in term S, which are described in the following sections.

4.2.4 Surface growth

Basically the important mechanism of the formation of aerosol phase of the organic compounds is partitioning the semi-volatile organic vapors. The partitioning happens through either adsorption or absorption of condensable organic species from gas phase to

aerosol phase. Adsorption mechanism is discussed in next section. Absorptive partitioning is vapor-particle mass transport due to the condensation of the gaseous phase on the surface of the aerosol particles. According to the measurements of Chen and Hopke (2009 a) the absorption partitioning coefficient, K_p , of gaseous phase organic species, which themselves were the products of α -pinene and ozone, was 0.44 ± 0.08 which is large (greater than 0.1) (Bowman et al., 1997). Also, the accommodation coefficient was high, $\alpha = 0.25 \pm 0.01$, which indicates that the mass transfer equilibrium between gaseous and aerosol phase was achieved instantaneously. Therefore, the vapor was low volatile and strongly tended to absorb on the surface of the existing aerosols as an absorption medium.

The secondary organic gases (SOGs) absorption on the SOAs led to increasing the size of the SOAs. Therefore, the first and second moments, M_1 and M_2 , increased due to the additional mass to the SOAs. However, the total number of particles, and so the zeroth moment, M_0 , is constant due to partitioning. The surface growth is modeled based on the moment model developed by Frenklach and Harris (1987) and Lee (1983). The discretized model applied in the numerical solution is,

$$\frac{dM_k}{dt} = \pi \left(\frac{6}{\pi\rho} \right)^{\frac{2}{3}} \frac{k_s}{\Delta m} \sum_{i=0}^{k-1} \binom{k}{i} \Delta m^{k-i} M_{i+\frac{2}{3}} \quad (4.14)$$

k_s [gr/cm²] is the growth rate per unit area, and Δm represents the mass difference between adjacent size bins. In the computational model the mass difference between bins

is calculated as $\Delta m = \left(\frac{\pi}{6} \right) \rho (d_{\min})^3$, where ρ is the particle density, equal to $1.07 \left[\frac{g}{cm^3} \right]$,

and d_{\min} is the 0.1 nm.

4.2.5 Nucleation

The adsorption of the gaseous phase to the aerosol particles occurs when the concentration of the SOGs increases because of the reaction of the parent hydrocarbon, α -pinene here, with ozone, and its partial pressure exceeds its saturation state. Thus, gas to particle conversion can occur directly through nucleation. In the experiment carried out by Chen and Hopke (2009a), no initial seeding particles were injected in the reactor chamber so no aerosols as absorption medium existed. The organic gaseous produced from the reaction of α -pinene and ozone are semi-volatile with low saturation pressure. Within 1 h after injection of α -pinene a high concentration of secondary organic aerosols were nucleated in the mixing chamber (Figure 4.2). The α -pinene, ozone and air flow were constantly injected into the mixing chamber, and gas mixtures including the reaction by product and particulate phases were exhausted from the chamber. Therefore, nucleation occurs continuously in the tank and after 7 hours the rate of the nucleation and the exhaust of the particulate matters approached steady state condition.

In the experiment, the particle formation rate in the steady state condition was evaluated as $3310 \left[\frac{\#}{cm^3 h} \right]$. The same nucleation rate was implemented in the numerical simulation, assuming particles with 14 nm diameter, which was the minimum particle size measured by SMPS, were generated with the rate of $N = 3310 \left[\frac{\#}{cm^3 h} \right]$. Therefore, the rate of nucleation of the first three moments is calculated using Eq. (4.7).

4.2.6 Conversion of moments to particle concentration

To compare the numerical results of MOMs with the experimental data of Chen and Hopke (2009a), the moments are converted to the particles number concentration versus their sizes using lognormal size distribution ($n(v,t)$) given in Eq. 4.5. In the experiment the number concentration of 109 particle size bins, $d_{p_i}^{exp}$, $1 < i < 109$, in range of 14 nm to 700 nm was measured. The 109 bins were not distributed uniformly in this size range (14 nm-700 nm), and the width of the bins for small particles is smaller than the ones for the large particles. However, in the numerical model this size space is discretized into 6,716 size bins with the diameter intervals of 0.1 nm.

The integral of the particle size distribution density function, $n(v, t)$, over the size range of which $d_{p_i}^{exp}$ is in center, gives the number concentration of the particle, $N(v, t)$, at this size. ($d_{p_i}^{exp}$ is the size of the SOA, which its concentration is measured in the experiment)

$$N(v(d_{p_i}^{exp}), t) = \int_a^b n(v', t) dv', \quad (4.15)$$

$$\text{where } a = v(d_{p_i}^{exp} - \Delta), \quad b = v(d_{p_i}^{exp} + \Delta)$$

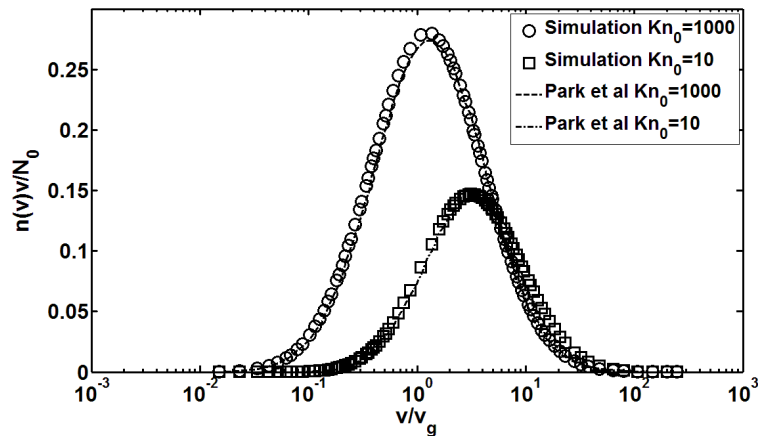
Here Δ indicates the interval size around the $d_{p_i}^{exp}$.

4.3 Validation of the numerical simulation for Brownian coagulation

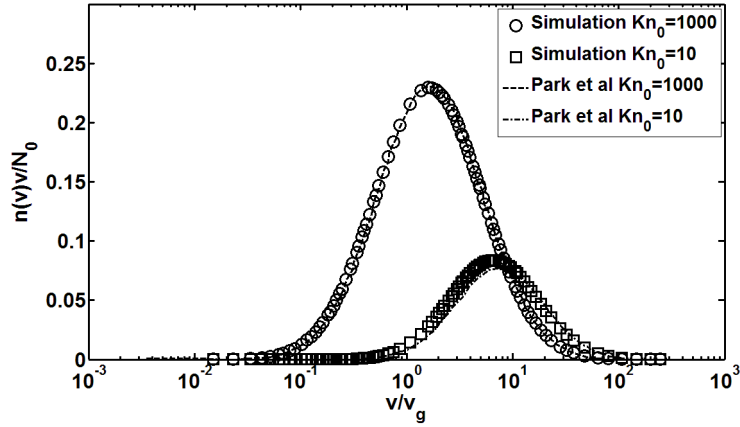
The Brownian coagulations of extremely small and small size particles are numerically simulated and compared with the analytical solution developed by Park et al. (1999) and Park and Lee (2000). The analytical solution of particles coagulation is provided by assuming that the particle concentrations follow the lognormal distribution. The PBE is

solved, using the MOMs, for particles in hypothetical size range of free molecular and continuum regimes. The particle size range is extended to the transition regimes by implementing the harmonic mean.

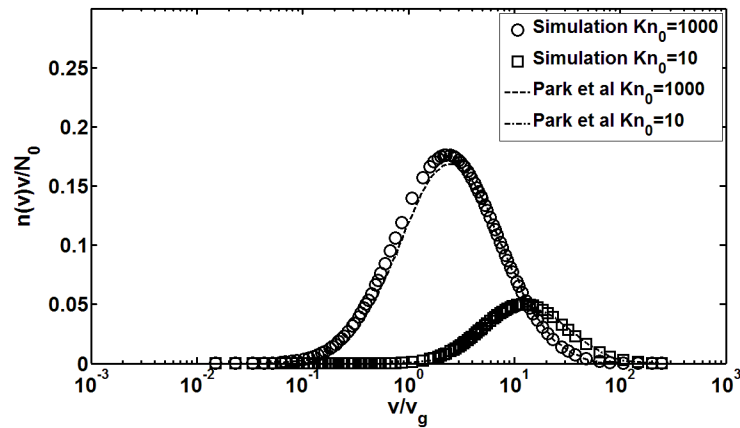
The discretized MOM equations are simulated using Runge-Kutta numerical method. The non-dimensionalized form of the particle number concentration distribution with respect to the non-dimensionalized size of particles is compared with the analytical solution obtained by Park et al. (1999). The study is conducted for two initial particle size distributions at the beginning of the process; one ultrafine particles with initial $Kn_0 = 1000$, and the other one fine particles, in the transition regime, with $Kn_0 = 10$. The particle number concentration is reconstructed from the predicted moments using the lognormal distribution function. The reconstructed number concentrations are shown in Figure 4.3 (a,b and c), respectively, for the non-dimensionalized time sequences of $t' = 0.2, 0.5$ and 1 , where $t' = K_{co}N_0t$.



(a) $K_{co}N_0t=0.2$



(b) $K_{co}N_0t=0.5$



(c) $K_{co}N_0t=1$

Figure 4.3 Comparison of numerical solution of particle Brownian coagulations with the analytical solution of Park et al. (1999) for three time intervals.

Comparing the coagulation rate of particles which were initially in the free molecular and transition regimes shows that the hypothetical particles with $Kn_0 = 1000$ have higher coagulation rate due to their larger collision kernel coefficient. Figure 4.3 also shows that the simulated number distribution of particle size using MOM is in good agreement with the analytical solution of Park et al. (1999).

4.4 Results and discussion

By injection of the chemical components in the mixing chamber a burst of aerosol nucleation occurs and after about 7 h the number-size concentration of particles reaches steady state condition. The evolution of the moments, M_0 , M_1 and M_2 over this time is modeled using the Method of Moments (MOMs). The zeroth moment, M_0 , represents the number concentration of particles and the first moment, M_1 , determines the total mass concentration.

In order to numerically simulate the experiment of Chen and Hopke (2009 a) as described in section 4.2, the Brownian coagulation, the surface growth and the constant nucleation of particles are included in the model. Also, the loss of mass conservation due to the particulate phase exhaust from the chamber during the experiment is included in the analysis. The concentration of the aerosols in sizes measured in the experiment are predicted from the moments and based on the lognormal size distribution of aerosols (Eq. (4.7) and Eq. (4.15)).

The time evolution of the number concentrations of particles for four time intervals, $t = 1, 1.5, 2.5$ and 5 h, are shown in Figure 4.4. The time $t = 1$ h corresponds to the initial phase, when the chemical supply is freshly introduced into the chamber, and $t = 5$ h represents the late stage, when the concentration distribution is in its middle way to the steady state condition. The concentration of small particles in size of 20 nm is the highest at the beginning of the particle population development at $t = 1$ h. As time passes by 4 h, the peak of number concentration shifts from small particles of about 20 nm to large particles of about 110 nm, which is due to the particles coagulation and surface growth.

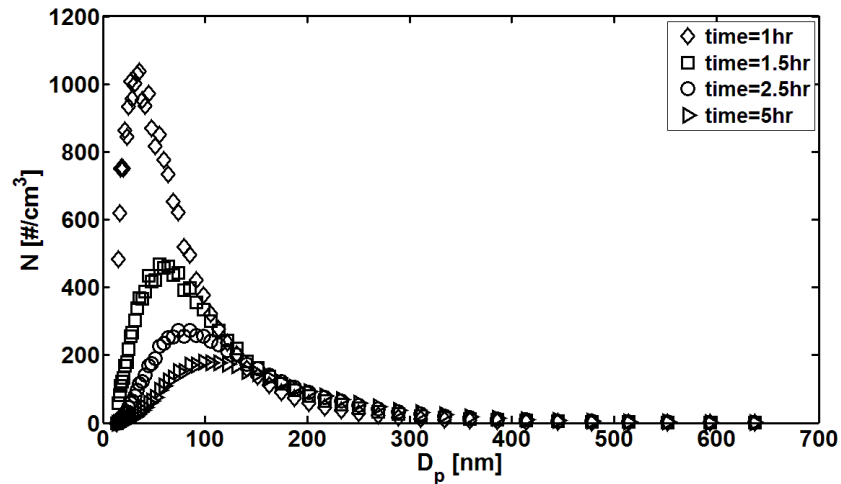


Figure 4.4 Time evolution of particles concentration distribution due to coagulation, nucleation and surface growth.

The predicted concentration distribution at $t = 7$ h is compared with the experimental data of steady state conditions by Chen and Hopke (2009a) in Figure 4.5. The size distribution is plotted as $dN^*/d(\text{Log}(D_p))$, which is non-dimensionalized by dividing the concentration to the total number concentration of particles, $N^* = N/N_{\text{total}}$. Also, the D_p axis is in a logarithmic scale. The discrepancies between the predicted concentration distribution and the experimental data for the size range of 20 to 40 nm and 80 to 110 nm are because of the complexity of the mechanisms involved in the size-concentration development of SOAs in the experiment. Other than that the simulated size distribution follows the trend of the experiment measurements. Before time $t = 7$ h the concentration predicted for particles with $D_p < 150$ nm is larger than the experimental data, and for $D_p > 150$ it is smaller than the experiment. For this case, the rate of nucleation, coagulation and condensation on particles are in equilibrium with the rate of the SOAs leaving the chamber.

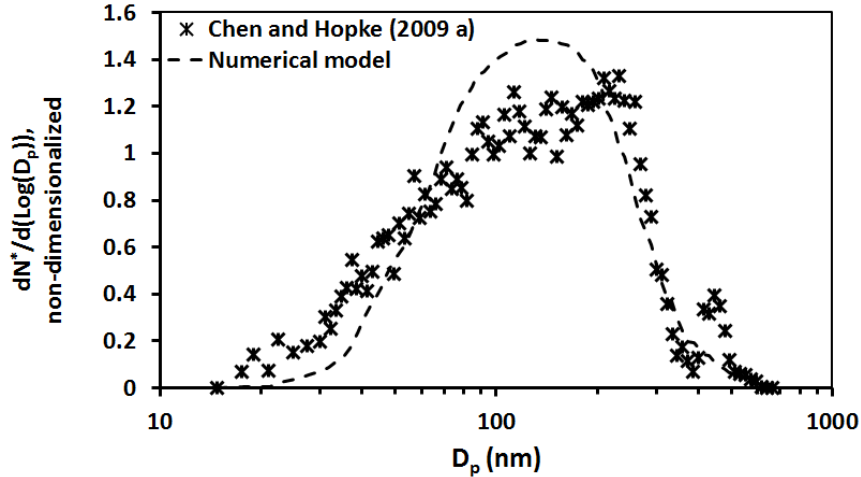


Figure 4.5 Comparison of the predicted particles concentration distribution with the experimental data of Chen and Hopke (2009a) at $t = 7$ h.

The experimental data shows a second peak of the number concentration at the particle size range between 400 nm and 500 nm. It is conjectured that this second peak is due to the second-generation of condensable semi-volatile products resulting from the reaction of first-generation products with OH which consequently would increase the surface growth of aerosol phase. The MOM was not able to capture the second peak, based on the available experimental data.

Also, the time evolutions of the first three moments of the particle concentration distributions are shown in Figure 4.6. The moments are non-dimensionalized by division by their initial values. The total number of particles, M_0 , decreased in time because of the particles collision and coagulation. At initial phase, the total particle mass, M_1 , increased sharply due to the SOAs nucleation and the surface growth. After $t = 90$ min the rate of mass production approached steady condition due to the balance with the rate of particles exiting from the chamber. When two particles collide, their masses and, based on the assumption of the constant density, their volumes were added together. So, coagulation led to increasing the total surface to volume ratio of the SOAs represented by M_2 . The

maximum surface to volume ratio of the SOAs occurred at $t = 70$ min and then with a slow slop it decreased to the steady conditions.

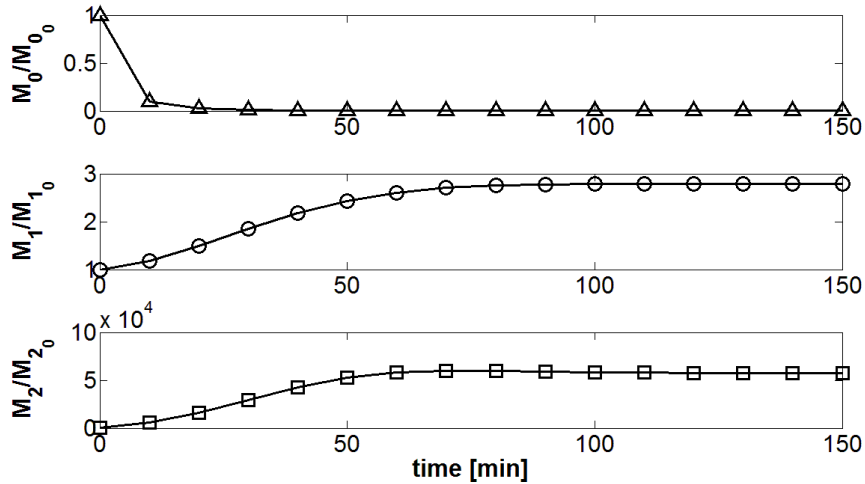


Figure 4.6 The time evolution of the moments of the particle concentration distribution.

4.5 Distribution of SOAs in an office with mixed-mode ventilation systems

4.5.1 Introduction

A large portion of the indoor air pollutants are due to the formation of the SOAs from reaction of ozone in the air with the materials used in the indoor environment including paints, cleaners and furniture. The model developed for the evolution of moments of SOAs is applied to study the indoor air concentration distribution for two mixed-mode ventilation systems in a typical office space. The two dimensional geometry of the office space under study is shown in Figure 4.7. A human model is considered behind a desk, a computer screen is on the desk, and a couch, which is the emission source of the SOAs, is next to the desk. The room size is $6 \times 3 \text{ m}^2$.

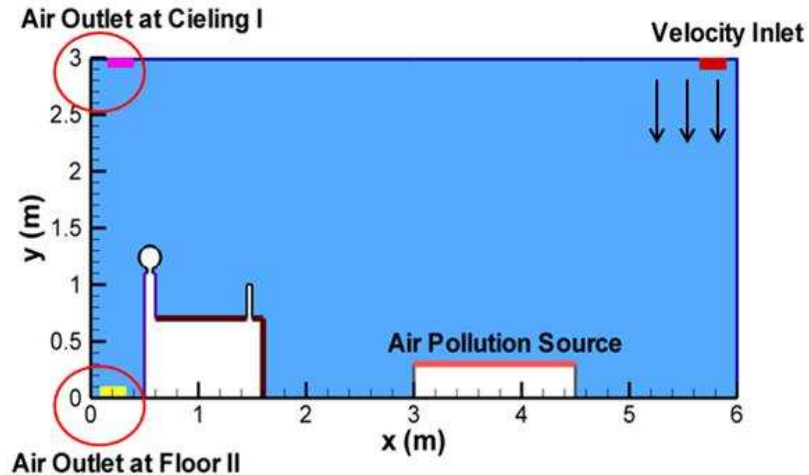


Figure 4.7 The 2D geometry of the office model, with two ventilation systems. In case (I), the air outlet is located at the ceiling. In Case (II), the air outlet is located on the floor.

Two types of ventilation systems are considered. In both cases the fresh air enters the room from the ceiling. In case (I) air leaves the room from the ceiling at the opposite side of the inlet, and in case (II) the air is sucked out from the floor behind the human model. The Air Change Rate (ACR) is 5 h^{-1} which is a typical ACR for an office room. Thus, the velocity of the air at the inlet of the ventilation system is 0.1 m/s . Since the velocity magnitude and, consequently, the Reynolds number in the room space are too small, the flow field is numerically simulated using unsteady laminar model. The time step is set for 0.2 seconds, and the concentration of the SOAs is tracked over time.

Structured rectangular grid cells in size of $1 \times 1 \text{ cm}^2$ are constructed in the most area of the numerical domain using GAMBIT software. The only exception is the zone close to the head of the manikin, which triangular grids are generated.

The concentration distribution and size variation of particulate pollutants over time are investigated. A wide range of particle sizes from ultra-fine particles in molecular regime ($\text{Kn} > 50$) to coarse particles in continuum regime ($\text{Kn} < 1$) is studied.

By integrating the orders of volumes of the particles over the PBEs the moment equations are attained. The method of moments is more time efficient in comparison with the other methods of solving PBEs. Furthermore, the particle concentration distribution was predicted, presuming a log-normal Gaussian distribution as a closure approach for the moment equations. Particles in size of 14 nm are emitted with the rate of $3310 \left[\frac{cm^3}{h} \right]$, from the couch at the center of the office. A User Defined Scalar (UDS) code is provided and added to the Fluent (ANSYS Inc.), to model the moments of the particles (using MOM) and the airflow simultaneously.

The numerical simulation is conducted by using the Fluent software (ANSYS Inc.), with the aid of a computer with 32 GB RAM and 4 parallel CPUs. The computational time was 72 h for each case study.

4.5.2 Results and discussion

The airflow field and the particulate pollutant transport in an office environment are simulated for two different ventilation systems. The contours of the flow fields and the pressure fields for the ventilation systems type (I) and type (II) are shown in Figure 4.8 and Figure 4.9, respectively. When the outlet is at the ceiling, the flow rate passes the area in vicinity of the manikin's head and mouth is less than when the outlet is designed on the floor. The negative pressure field, showed in Figure 4.9, in the area at the middle of the room and above the couch illustrates the recirculation zone.

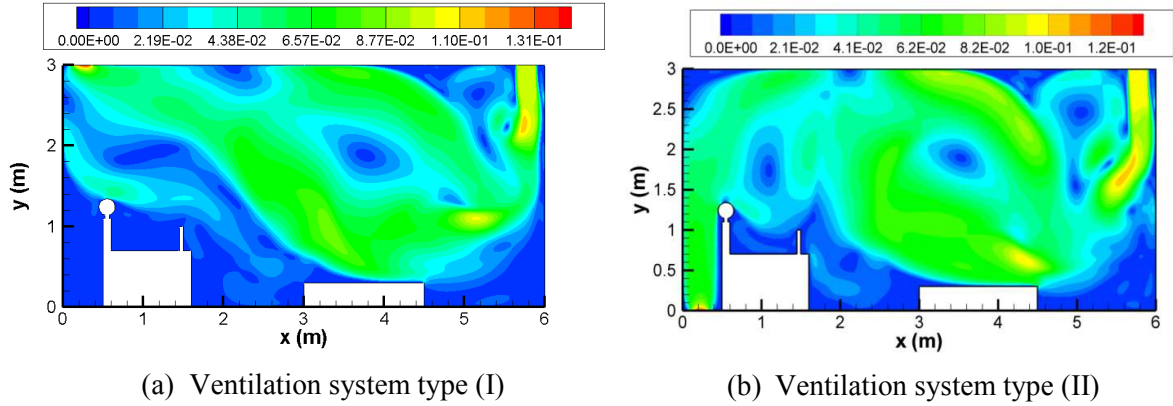


Figure 4.8 Contours of velocity magnitude, [m/s], for ventilation systems (a) type (I) and (b) type (II).

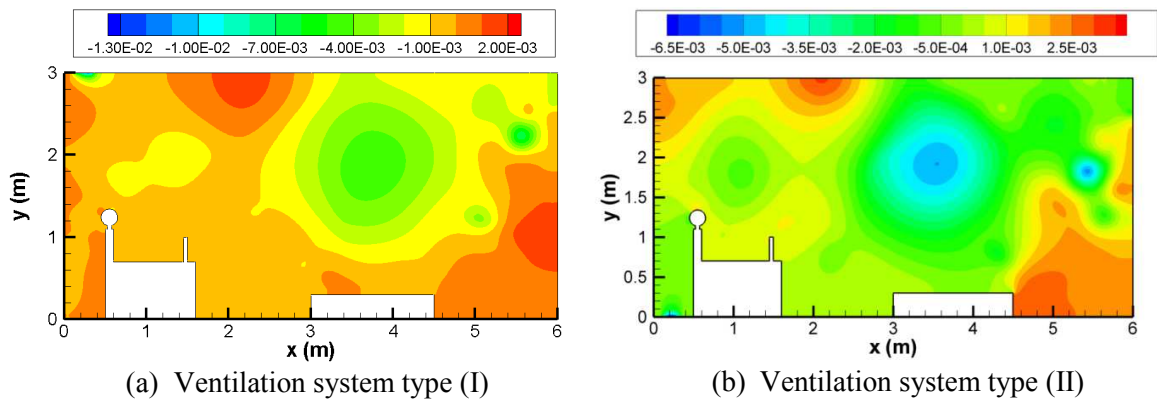


Figure 4.9 Pressure contours, [Pa], for ventilation systems (a) type (I) and (b) type (II).

It is assumed that a constant number of SOAs, with 14 nm diameter, emits every 0.3 s from the surface of the couch. The initial three moments of the particle concentration, emitted from the couch at each time step, equivalent to $M_0 = 4195200$ [#], $M_1 = 7 \times 10^7$ [#·cm³] and $M_2 = 1.5753 \times 10^{-35}$ [#·cm⁶]. The SOAs are transported by air circulation inside the room, and they are diffused by their Brownian motion.

The distribution of the zeroth moment, M_0 , over time is presented for ventilation systems (I) and (II) in Figure 4.10. The time series are 500, 1000 and 1500 s after the initial emission of the particles from the source of the air pollution. The plume of nano particles is carried by the air flow from the source towards the outlet. The concentration of

particulate pollutants at the circulation center, and where the velocity magnitude is low is higher than the other regions. Also, the time average of the pollutants concentration at the vicinity of the manikin's mouth is higher in the ventilation system type (II), rather than in the ventilation system type (I), where the air outlet is located at the ceiling.

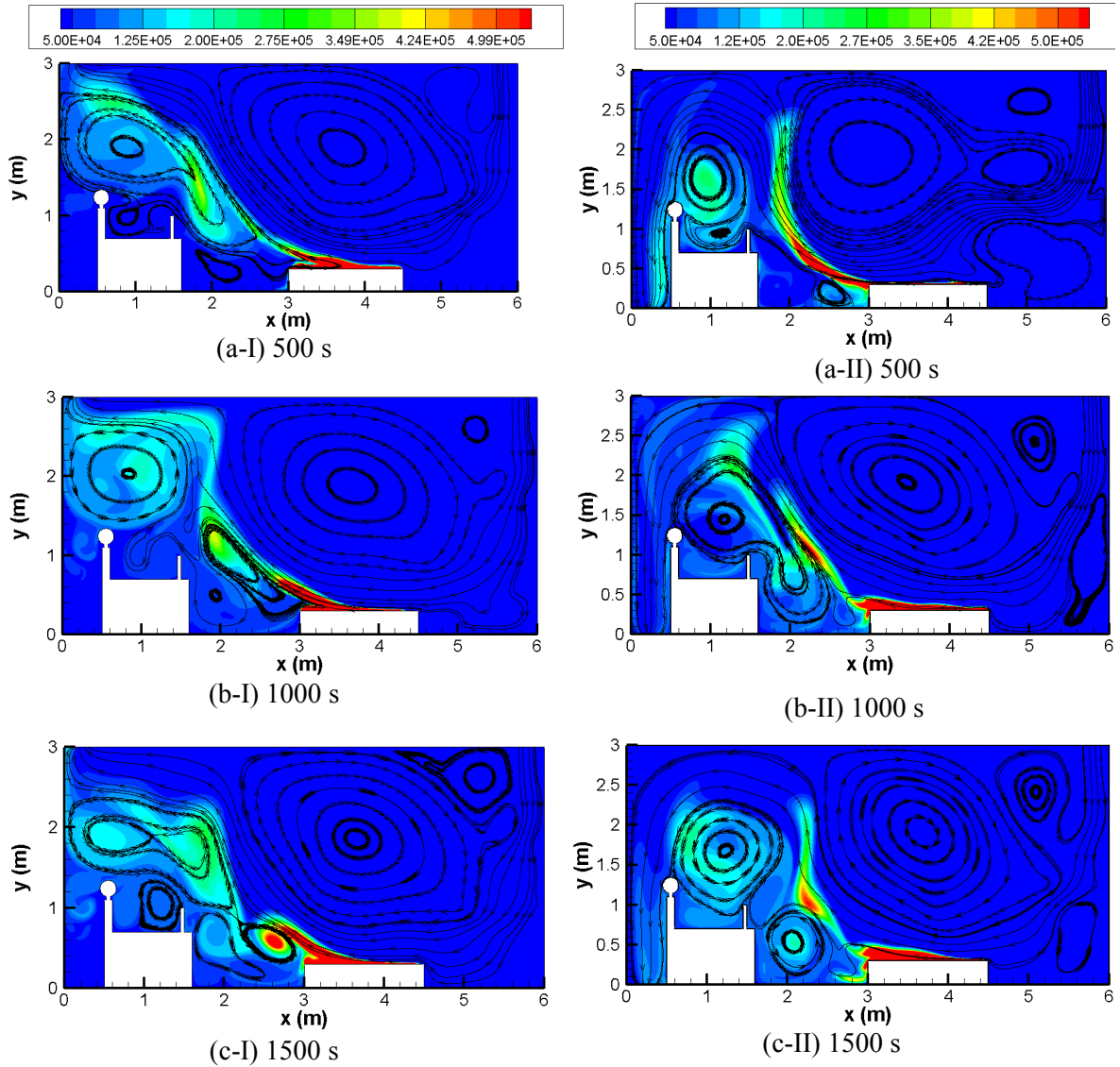


Figure 4.10 Contours of M_0 , total number of particles [#], at time intervals, (a) 500 s, (b) 1000 s and (c) 1500 s for ventilation systems (I) and (II).

The time evolution of non-scaled parameters, $\frac{M_0}{M_{0_0}} \times 100$, $\frac{M_1}{M_{1_0}} \times 100$ and $\frac{M_2}{M_{2_0}} \times 100$, at a point close to the mouth of the manikin, for ventilation system (I) is shown in Figure 4.11. The moments of concentration distribution are non-dimensionalized by dividing by the initial moments distributed in the room. The pollutants moments increased by time till about 25 min when it reached the steady state condition. The total number concentration of the particulate pollutants reached 150 times its initial concentration in vicinity of the manikin's mouth due to the distribution of emitted particles from the couch surface by the ventilation of air in the room. Similarly the first and second moments got 550 and 2000 times bigger than their initial values, respectively.

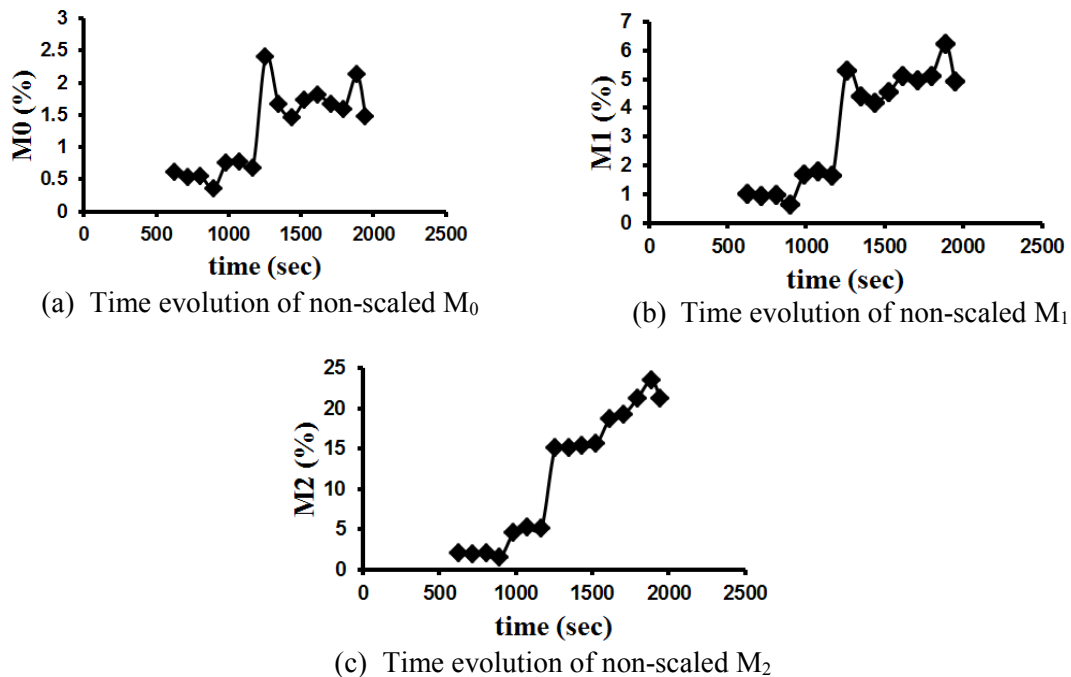
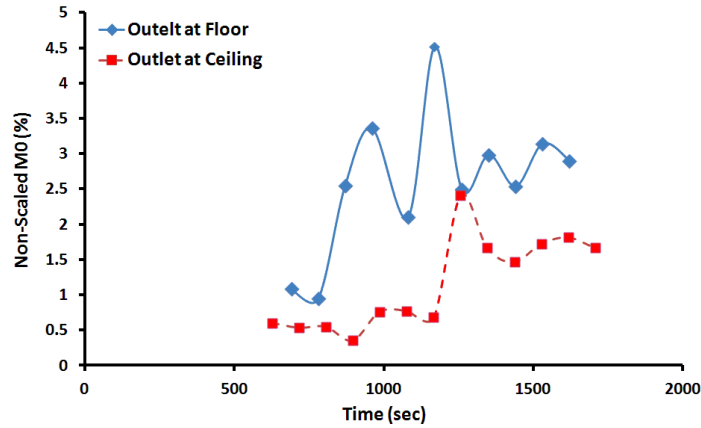


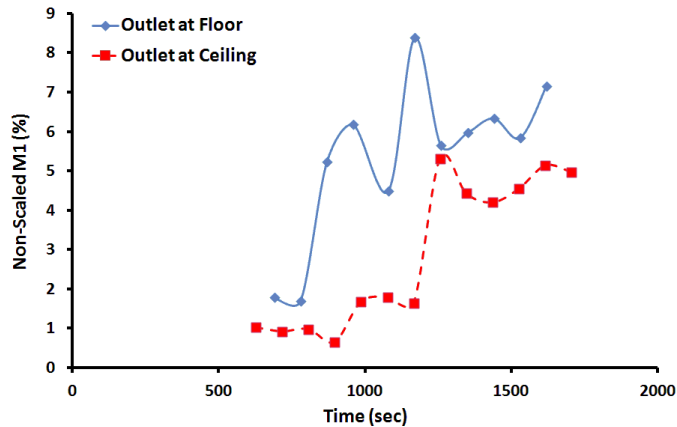
Figure 4.11 The time evolution of the moments of concentration distribution at a point close to the mouth of the manikin for ventilation system (I).

In addition, the evolutions of the M_0 and M_1 moments over time are compared for both ventilation systems in Figure 4.12. The total number concentration, M_0 , as well as the

total mass concentration, M_1 , of particulate pollutants close to the manikin's mouth was much smaller in case which the outlet is located at the ceiling, rather than the case which the outlet is on the floor behind the manikin.



(a) Comparison of non-scaled moment, M_0 , for two ventilation systems with outlet in floor and in ceiling



(a) Comparison of non-scaled moment, M_1 , for two ventilation systems with outlet in floor and in ceiling

Figure 4.12 Comparison of the total number concentration (M_0) and the total mass concentration (M_1) of particulate pollutants at the manikin's breathing zone.

4.6 Conclusions

The nucleation, coagulation and surface growth of a wide range of particle sizes were modeled, by using the MOMs with assuming that the PSDs follow a lognormal function.

The simulation was compared with the experiment performed in a dynamic mixing

chamber by Chen and Hopke (2009 a). The Brownian collision kernel, applied in coagulation simulation, was evaluated by comparing with the solutions of Park et al. (1999). The SOAs concentration distribution were reconstructed based on the predicted first three moments, and compared with the experiment measurements extracted in steady state conditions by Chen and Hopke (2009 a). The numerical simulation predicted the nucleation burst, transition and steady state stages of the particles concentration distribution which was in agreement with the experimental data.

Also, the concentration distribution of the particulate pollutants was coupled with the air flow in a 2D model of an office room as a sample of an indoor environment. Two ventilation systems with outlet located on the ceiling and at the floor are investigated. The pollutant concentrations distributed in space because of the particles' Brownian motion as well as the drag force induced from their interaction with the airflow field. Comparing the distribution of air pollution in two ventilation systems showed that the one with an air outlet at the ceiling was more efficient in terms of keeping the SOAs away from the resident sitting behind his/her workstation. Monitoring the concentration of particulate pollutants at a point in vicinity of the mouth of the human model showed that for both cases the pollution increased and reached a steady condition in 20 minutes which is the time for a complete air exchange in the room.

References

ANSYS Inc. (a). "FLUENT 12.1.4." .

ANSYS Inc. (b). "GAMBIT 4.2.6." .

Brock, J., and Oates, J. (1987). "Moment simulation of aerosol evaporation." *J.Aerosol Sci.*, 18(1), 59-64.

Chen, X., and Hopke, P. (2009a). "Secondary organic aerosol from α -pinene ozonolysis in dynamic chamber system." *Indoor Air*, 19(4), 335-345.

Chen, X., and Hopke, P. K. (2009b). "A Chamber Study of Secondary Organic Aerosol From Ozonolysis of Biogenic Hydrocarbons." PhD thesis, Center for the Environment, Clarkson University, .

Frenklach, M., and Harris, S. J. (1987). "Aerosol dynamics modeling using the method of moments." *J.Colloid Interface Sci.*, 118(1), 252-261.

Lee, K. (1983). "Change of particle size distribution during Brownian coagulation." *J.Colloid Interface Sci.*, 92(2), 315-325.

Lee, K., and Hwang, J. (1997). "Erratum to "Log-Normally Preserving Size Distribution for Brownian Coagulation in the Free Molecule Regime" by Lee et al. and "Coagulation Rate of Polydisperse Particles" by Lee and Chen." .

Lee, K., Lee, Y., and Han, D. (1997). "The log-normal size distribution theory for Brownian coagulation in the low Knudsen number regime." *J.Colloid Interface Sci.*, 188(2), 486-492.

Park, S., Lee, K., Otto, E., and Fissan, H. (1999). "The log-normal size distribution theory of brownian aerosol coagulation for the entire particle size range:: Part I-- analytical solution using the harmonic mean coagulation kernel." *J.Aerosol Sci.*, 30(1), 3-16.

Park, S. H., and Lee, K. W. (2000). "Condensational growth of polydispersed aerosols for the entire particle size range." *J.Aerosol Sci.*, 31, Supplement 1(0), 813-814.

Pratsinis, S. E. (1988). "Simultaneous nucleation, condensation, and coagulation in aerosol reactors." *J.Colloid Interface Sci.*, 124(2), 416-427.

Sarwar, G., Corsi, R., Allen, D., and Weschler, C. (2003). "The significance of secondary organic aerosol formation and growth in buildings: experimental and computational evidence." *Atmos.Environ.*, 37(9-10), 1365-1381.

Smoluchowski, M. (1917). "Versuch einer mathematischen Theorie der Koagulationskinetik kolloider Lösungen." *Z.Phys.Chem.*, 92(129-168), 9.

Weschler, C. J. (2000). "Ozone in indoor environments: concentration and chemistry." *Indoor Air*, 10(4), 269-288.

Whitby, E. R., and McMurry, P. H. (1997). "Modal aerosol dynamics modeling." *Aerosol Science and Technology*, 27(6), 673-688.

Williams, M. (1986). "Some topics in nuclear aerosol dynamics." *Prog.Nuclear Energy*, 17(1), 1-52.

CONCLUSIONS

Based on the presented results, the following conclusions are drawn:

Particle Transport and Deposition Around Bluff Bodies

1. A computational model for analyzing the airflow and particle pollutants in duct, and around bluff bodies was developed. Both RSTM and LES models were used in the computational model. The computational model also included Lagrangian particle tracking approach.
2. To investigate the particulate pollutant transport over a bluff body with complex geometry, and at high Reynolds number ($Re = 80,000$), first the detailed features of the mean airflow are computed. Then, the velocity fluctuations are evaluated because of their important role in predicting the particle dispersion and deposition.
 - a. The Large Eddy Simulation predicted the detailed features of the flow field, in agreement with the PIV measurements.
 - b. Although RANS-RSTM predicted the general patterns of the flow and pressure fields, it was not able to capture the details of the recirculation zones at the same computational domain as the LES.
 - c. Using the Langevin stochastic differential equation, a model for reconstructing the turbulent velocity fluctuations was developed. A User Defined Function (UDF) for simulating the turbulent fluctuation using the Continuous Random Walk model was developed and used for the RANS-RSTM of ANSYS-Fluent 12.1 code. The new model adds the capability

of studying particle transport and deposition in transient turbulent flows. The earlier model developed by Tian and Ahmadi (2007) was restricted to steady mean flows.

- d. Since ANSYS Fluent12.1 does not provide a model for generating subgrid scale velocity fluctuations when the LES is used, a new Continuous Random Walk UDF model was developed and used for reconstructing the subgrid scale velocity fluctuations.
3. The SGS turbulent kinetic energy over the building model showed a high turbulent region on the top side of the building.
4. The deposition of particulate pollutant over the model of the CoE Building was analyzed. The highest concentration of the particles was found at the front façade and over the ground close to the building. The large fluid velocity fluctuations at top roof led to high concentration of particulate pollutants in this region. The lowest particle concentrations were found at the back side of the building, where the recirculation regions existed.

Secondary Organic Aerosols Formation, Distribution and Transport

5. Using the population dynamics approach, a computational model for evaluating the evolution of size distribution of Secondary Organic Aerosols (SOA) was developed and compared with the experimental data from an indoor dynamic flow chamber system. The population dynamics of SOAs in a mixing chamber was modeled using method of moments (MOM), where nucleation, Brownian coagulation and surface growth of SOAs were included. Moments were evaluated for a lognormal size distribution. The resulting moments were converted to the

aerosols concentrations for the size bins that were used in the experimental measurements and compared with the data.

6. The concentration of SOAs in size of 14 nm were at its highest peak at the beginning of the process, $t = 1$ h after injection of chemical components into the mixing chamber. As time evolved the number concentration of smaller particles ($dp < 100$ nm) decreased and that of larger particles ($dp > 100$ nm) increased. That was due to the collision and coagulation of the aerosols, and also, because of the condensation of semi-volatile aldehyde gases on the existing aerosols (surface growth). After 7 h the concentration distribution of SOAs matched the experimental data measured in steady state condition which occurred in the time interval of 7 to 9 h after the process started.
7. The SOAs formation, transport and concentration in an office space were modeled and the effectiveness of two mixed-mode ventilation systems on air quality was evaluated. The air inlet was in the ceiling for both ventilation systems, and the outlets were placed in the ceiling and in the floor. Comparison of the concentration of SOAs in the breathing zone of the manikin in the office showed that, for the particular configuration studied, when the outlet register was placed in the ceiling the pollutant concentration in the manikin breathing zone is less than that for the case with the outlet in the floor.

FUTURE WORKS

- a) The particle transport model in a 2D turbulent channel flow was evaluated, and the effect of the turbulent velocity fluctuations was studied. The following future investigations would be worthwhile continuation for better understanding of particle transport in the 3D and transient turbulent flow fields:
1. Providing a detailed model of the Eulerian time scale and length scale seen by the particles with small Stokes number using the LES of turbulent airflow field.
 2. Performing a detailed study of particle dispersion and deposition in a 3D channel flow using LES.
 3. Investigating the particles transport and deposition for turbulent flows over a square cylinder with emphasis on the effect of transient feature of the airflow field.
 4. In the 3D flow in a square duct in addition to the small and large turbulent eddies, secondary flows play an important role in distributing particles. Providing an understanding of the effect of secondary flows on the particle distribution pattern in the duct flow would be a potential future work.
- b) The air flows over the wall mounted square cylinder and the scale-model of the CoE building were modeled using RSTM and LES turbulence models, the following investigations may help understanding the particles dispersion over a bluff body,
1. Comparing the deposition velocity of particles on the square cylinder for the turbulent flows modeled by RSTM and LES.

2. Studying the wind flow and particle deposition over the full-scale model of the CoE building would give more realistic information about the pollution distribution over the building. The flow field can be modeled using hybrid LES and RANS turbulence models to reduce the computational time. Also a measurement over the size and concentration distribution of the air pollutants at the source points, which are the highways around the CoE building, and at the inlet of the air handling system would be extremely valuable data to set the numerical model and evaluate its predictions.
- c) The population density of secondary organic aerosols (SOAs), was modeled using method of moments (MOM), and by considering the particles nucleation, Brownian coagulation and surface growth. The following investigation may refine the estimation of the size-concentration distribution of these semi-volatile particles
1. Since SOA are semi-volatile, surface growth plays an important role in their size-concentration distribution over time. Therefore, a precise study on the thermal properties of the main components of SOAs would modify the available models of surface growth.
 2. Using quadratic method of moments (QMOM) instead of MOM may increase the accuracy of solving population balance equation.
 3. In current MOM three moments of particle concentration was applied. Using larger number of moments may improve the predictions of size distribution.
- d) The population balance equation of SOAs was coupled with the air flow field produced by a mixing ventilation system in an office model,

1. Since the rate of size and concentration distribution of SOAs is small, it would be interesting to model the pollution distribution in a room with natural ventilation system, and by considering the body temperature of the manikin.

REFERENCES

- Abramov, R. V. (2007). "An improved algorithm for the multidimensional moment-constrained maximum entropy problem." *Journal of Computational Physics*, 226(1), 621-644.
- Ahmadi, G., and Li, A. (2000). "Computer simulation of particle transport and deposition near a small isolated building." *J. Wind Eng. Ind. Aerodyn.*, 84(1), 23-46.
- Alexopoulos, A. H., and Kiparissides, C. A. (2005). "Part II: Dynamic evolution of the particle size distribution in particulate processes undergoing simultaneous particle nucleation, growth and aggregation." *Chemical Engineering Science*, 60(15), 4157-4169.
- Armenio, V., Piomelli, U., and Fiorotto, V. (1999). "Effect of the subgrid scales on particle motion." *Phys. Fluids*, 11 3030.
- ASHRAE. (2011). "Ultraviolet air and surface treatment." *ASHRAE Handbook*, HVAC Applications.
- Baetke, F., Werner, H., and Wengle, H. (1990). "Numerical simulation of turbulent flow over surface-mounted obstacles with sharp edges and corners." *J. Wind Eng. Ind. Aerodyn.*, 35(0), 129-147.
- Bahnfleth, W., Lee, B., Lau, J., and Freihaut, J. (2009). "Annual Simulation of in-duct ultraviolet germicidal irradiation system performance." *Eleventh International IBPSA Conference. Escócia*.
- Baik, J. J., and Kim, J. J. (1999). "A numerical study of flow and pollutant dispersion characteristics in urban street canyons." *J. Appl. Meteorol.*, 38(11), 1576-1589.
- Baldyga, J., and Orciuch, W. (1999). "Closure method for precipitation in inhomogeneous turbulence." *14th international symposium on industrial crystallization, IChemE, CD ROM ISBN 0-85295-424-7, Paper, .*
- Bandyopadhyay, K., Bhattacharya, A. K., Biswas, P., and Drabold, D. (2005). "Maximum entropy and the problem of moments: A stable algorithm." *Physical Review E*, 71(5), 057701.
- Barrett, J., and Jheeta, J. (1996). "Improving the accuracy of the moments method for solving the aerosol general dynamic equation." *J. Aerosol Sci.*, 27(8), 1135-1142.
- Batterham, R. J., Hall, J. S., and Barton, G. (1981). "Pelletizing kinetics and simulation of full-scale balling circuits." *Proc. 3rd Int. Symp. on Agglomeration, Nürnberg, Germany*, A136.

- Behrman, A. J., and Shofer, F. S. (1998). "Tuberculosis exposure and control in an urban emergency department." *Ann. Emerg. Med.*, 31(3), 370-375.
- Bensberg, A., Roth, P., Brink, R., and Lange, H. (1999). "Modeling of particle evolution in aerosol reactors with coflowing gaseous reactants." *AIChE J.*, 45(10), 2097-2107.
- Berrouk, A., Laurence, D., Riley, J., and Stock, D. (2007). "Stochastic modelling of inertial particle dispersion by subgrid motion for LES of high Reynolds number pipe flow." *Journal of Turbulence*, (8),.
- Bierman, A. (2007). "Field evaluation of ultraviolet germicidal irradiation (UVGI) in an air duct system." .
- Bleck, R. (1970). "A fast, approximative method for integrating the stochastic coalescence equation." *Journal of Geophysical Research*, 75(27), 5165-5171.
- Bowman, F. M., Odum, J. R., Seinfeld, J. H., and Pandis, S. N. (1997). "Mathematical model for gas-particle partitioning of secondary organic aerosols." *Atmos. Environ.*, 31(23), 3921-3931.
- Brickner, P. W., Vincent, R. L., First, M., Nardell, E., Murray, M., and Kaufman, W. (2003). "The application of ultraviolet germicidal irradiation to control transmission of airborne disease: bioterrorism countermeasure." *Public Health Rep.*, 118(2), 99.
- Brock, J., and Oates, J. (1987). "Moment simulation of aerosol evaporation." *J. Aerosol Sci.*, 18(1), 59-64.
- Brown, D., P., Kauppinen, E., I., Jokiniemi, J., K., Rubin, S. and G., Biswas P., (2006) "A method of moments based CFD model for polydisperse aerosol flows with strong interphase mass and heat transfer." *Computers & Fluids*, 35, 762-780.
- Brzoska, M. A., Stock, D., and Lamb, B. (1997). "Determination of plume capture by the building wake." *J. Wind Eng. Ind. Aerodyn.*, 67, 909-922.
- Calluau, D., Davd, L., and Texier, A. (2005). "Vortex shedding process investigation downstream a surface-mounted block." *Journal of Visualization*, 8(2), 99-108.
- Castro, I. P., and Dianat, M. (1983). "Surface flow patterns on rectangular bodies in thick boundary layers." *J. Wind Eng. Ind. Aerodyn.*, 11(1-3), 107-119.
- Castro, I. P., and Robins, A. G. (1977). "The flow around a surface-mounted cube in uniform and turbulent streams." *J. Fluid Mech.*, 79(2), 307-335.
- Chang, C., and Meroney, R. N. (2001). "Numerical and physical modeling of bluff body flow and dispersion in urban street canyons." *J. Wind Eng. Ind. Aerodyn.*, 89(14-15), 1325-1334.

- Chen, X., and Hopke, P. (2009a). "Secondary organic aerosol from α -pinene ozonolysis in dynamic chamber system." *Indoor Air*, 19(4), 335-345.
- Chen, X., and Hopke, P. K. (2009b). "A Chamber Study of Secondary Organic Aerosol From Ozonolysis of Biogenic Hydrocarbons." PhD thesis, Center for the Environment, Clarkson University, .
- Cheng, Y., Lien, F., Yee, E., and Sinclair, R. (2003). "A comparison of large Eddy simulations with a standard k- ϵ Reynolds-averaged Navier–Stokes model for the prediction of a fully developed turbulent flow over a matrix of cubes." *J.Wind Eng.Ind.Aerodyn.*, 91(11), 1301-1328.
- Chi, O. F., Yamada, H., and Shiozawa, K. (1996). "Evaluation of a two-dimensional numerical model for air quality simulation in a street canyon." *Atmos.Environ.*, 30(23), 3909-3915.
- CIE. (2003). "Ultraviolet air disinfection." *Commission Internationale De L'Eclairage, Vienna*, 155.
- Dehbi, A. (2008). "Turbulent particle dispersion in arbitrary wall-bounded geometries: a coupled CFD-Langevin-equation based approach." *Int.J.Multiphase Flow*, 34(9), 819-828.
- Dreeben, T. D., and Pope, S. B. (1997). "Probability density function and Reynolds-stress modeling of near-wall turbulent flows." *Physics of Fluids (1994-Present)*, 9(1), 154-163.
- Diemer, R., and Olson, J. (2002). "A moment methodology for coagulation and breakage problems: Part 2--moment models and distribution reconstruction." *Chemical Engineering Science*, 57(12), 2211-2228.
- Durbin, P. (1995). "Separated flow computations with the k- ϵ -v2 model." *AIAA J.*, 33(4), 659-664.
- Escombe, A. R., Moore, D. A. J., Gilman, R. H., Navincopa, M., Ticona, E., Mitchell, B., Noakes, C., Martínez, C., Sheen, P., and Ramirez, R. (2009). "Upper-room ultraviolet light and negative air ionization to prevent tuberculosis transmission." *PLoS Medicine*, 6(3), e1000043.
- Fan, F. G., and Ahmadi, G. (1993). "A sublayer model for turbulent deposition of particles in vertical ducts with smooth and rough surfaces." *J.Aerosol Sci.*, 24(1), 45-64.
- Fan, Z., Li, P., Weschler, C., Fiedler, N., Kipen, H., and Zhang, J. (2003). "Ozone-initiated reactions with mixtures of volatile organic compounds under simulated indoor conditions." *Environ.Sci.Technol.*, 37(9), 1811-1821.
- Ferziger, J. H. (1990). "Approaches to turbulent flow computation: Applications to flow over obstacles." *J.Wind Eng.Ind.Aerodyn.*, 35(0), 1-19.

- Fick, J., Pommer, L., Åstrand, A., Östin, R., Nilsson, C., and Andersson, B. (2005). "Ozonolysis of monoterpenes in mechanical ventilation systems." *Atmos. Environ.*, 39(34), 6315-6325.
- First, M., Rudnick, S. N., Banahan, K. F., Vincent, R. L., and Brickner, P. W. (2007). "Fundamental factors affecting upper-room ultraviolet germicidal irradiation—part I. Experimental." *Journal of Occupational and Environmental Hygiene*, 4(5), 321-331.
- First, M. W., Nardell, E., Chaisson, W., and Riley, R. (1999). "Guidelines for the Application of Upper-Room Ultraviolet Germicidal Irradiation for Preventing Transmission of Airborne Contagion-Part I: Basic Principles." *transactions-American society of heating refrigerating and air conditioning engineers*, 105 869-876.
- Frenklach, M., and Harris, S. J. (1987). "Aerosol dynamics modeling using the method of moments." *J.Colloid Interface Sci.*, 118(1), 252-261.
- Frenklach, M. (2002). "Method of moments with interpolative closure." *Chemical Engineering Science*, 57(12), 2229-2239.
- Frenklach, M., and Harris, S. J. (1987). "Aerosol dynamics modeling using the method of moments." *J.Colloid Interface Sci.*, 118(1), 252-261.
- Friedlander, S. K. (1977). "Smoke, dust and haze: Fundamentals of aerosol behavior." *New York, Wiley-Interscience, 1977.333 p.*, 1.
- Fröhlich, J., and Rodi, W. (2004). "LES of the flow around a circular cylinder of finite height." *Int J Heat Fluid Flow*, 25(3), 537-548.
- Gelbard, F., and Seinfeld, J. H. (1979). "Exact solution of the general dynamic equation for aerosol growth by condensation." *J.Colloid Interface Sci.*, 68(1), 173-183.
- Gidhagen, L., Johansson, C., Ström, J., Kristensson, A., Swietlicki, E., Pirjola, L., and Hansson, H. C. (2003). "Model simulation of ultrafine particles inside a road tunnel." *Atmos. Environ.*, 37(15), 2023-2036.
- Gobert, C., and Manhart, M. (2011). "Subgrid modelling for particle-LES by Spectrally Optimised Interpolation (SOI)." *Journal of Computational Physics*, 230(21), 7796-7820.
- He, C., and Ahmadi, G. (1999). "Particle deposition in a nearly developed turbulent duct flow with electrophoresis." *J.Aerosol Sci.*, 30(6), 739-758.
- Heintzenberg, J. (1994). "Properties of the log-normal particle size distribution." *Aerosol. Sci. Technol.*, 21, 46–8.
- Hefny, M. M., and Ooka, R. (2009). "CFD analysis of pollutant dispersion around buildings: Effect of cell geometry." *Build. Environ.*, 44(8), 1699-1706.

- Hidy, G. M. (1965). "On the theory of the coagulation of noninteracting particles in Brownian motion." *J.Colloid Sci.*, 20(2), 123-144.
- Higson, H., Griffiths, R., Jones, C., and Hall, D. (1994). "Concentration measurements around an isolated building: a comparison between wind tunnel and field data." *Atmos.EnvIRON.*, 28(11), 1827-1836.
- Hinds, W. C. (1982). "Aerosol technology: properties, behavior, and measurement of airborne particles." .
- Hounslow, M., Ryall, R., and Marshall, V. (1988). "A discretized population balance for nucleation, growth, and aggregation." *AIChE J.*, 34(11), 1821-1832.
- Hoxey, R., and Richards, P. (1993). "Flow patterns and pressure field around a full-scale building." *J.Wind Eng.Ind.Aerodyn.*, 50 203-212.
- Hubbard, H., Coleman, B., Sarwar, G., and Corsi, R. (2005). "Effects of an ozone-generating air purifier on indoor secondary particles in three residential dwellings." *Indoor Air*, 15(6), 432-444.
- Hulburt, H., and Katz, S. (1964). "Some problems in particle technology:: A statistical mechanical formulation." *Chemical Engineering Science*, 19(8), 555-574.
- Hunt, J. C. R., Abell, C. J., Peterka, J. A., and Woo, H. (1978). "Kinetic studies of the flows around free or surface mounted obstacles, applying topology to flow visualization." *Journal of Fluid Mechanics*, 86(1), 179-200.
- Hussein, H. J., and Martinuzzi, R. (1996). "Energy balance for turbulent flow around a surface mounted cube placed in a channel." *Phys.Fluids*, 8 764.
- Iaccarino, G., Ooi, A., Durbin, P., and Behnia, M. (2003). "Reynolds averaged simulation of unsteady separated flow." *Int J Heat Fluid Flow*, 24(2), 147-156.
- Jain, S., Fotou, G. P., and Kodas, T. T. (1997). "A theoretical study on gas-phase coating of aerosol particles." *J.Colloid Interface Sci.*, 185(1), 26-38.
- Jain, S., and Kodas, T. (1998). "Asymptotic widths of size distributions resulting from collisional growth assuming log-normally distributed fractal aggregates." *J.Aerosol Sci.*, 29(3), 259-261.
- Jin, G., He, G., Wang, L., and Zhang, J. (2010). "Subgrid scale fluid velocity timescales seen by inertial particles in large-eddy simulation of particle-laden turbulence." *Int.J.Multiphase Flow*, 36(5), 432-437.
- Kass, R. E., and Wasserman, L. (1996). "The selection of prior distributions by formal rules." *Journal of the American Statistical Association*, 91(435), 1343-1370.

- Kehe, J., Bohl, D., Ahmadi, G., and Tavakoli, B. (2009). "Experimental Study of Airflow Around the Syracuse CoE Building." ASME, .
- Kemp, S. J., Kuehn, T. H., Pui, D. Y. H., Vesley, D., and Streifel, A. J. (1995). "Filter collection efficiency and growth of microorganisms on filters loaded with outdoor air." *ASHRAE Trans*, (1), 228-238.
- Kethley, T. W., and Branch, K. (1972). "Ultraviolet lamps for room air disinfection. Effect of sampling location and particle size of bacterial aerosol." *Arch. Environ. Health*, 25(3), 205-214.
- Kielkiewicz, M. (1994). "Accuracy of the moments method." *Ann. Nucl. Energy*, 21(3), 189-193.
- Kim, Y. M., Harrad, S., and Harrison, R. M. (2001). "Concentrations and sources of VOCs in urban domestic and public microenvironments." *Environ. Sci. Technol.*, 35(6), 997-1004.
- Kim, W., and Menon, S. (1997). "Application of the localized dynamic subgrid-scale model to turbulent wall-bounded flows." *AIAA Paper*, 97-0210.
- Ko, G., Burge, H. A., Nardell, E. A., and Thompson, K. M. (2001). "Estimation of tuberculosis risk and incidence under upper room ultraviolet germicidal irradiation in a waiting room in a hypothetical scenario." *Risk Analysis*, 21(4), 657-674.
- Ko, G., First, M. W., and Burge, H. A. (2002). "The characterization of upper-room ultraviolet germicidal irradiation in inactivating airborne microorganisms." *Environ. Health Perspect.*, 110(1), 95.
- Kowalski, W. (2009). *Ultraviolet Germicidal Irradiation Handbook: UVGI for Air and Surface Disinfection*. Springer Verlag, .
- Kowalski, W. J. (2003). *Immune building systems technology*. McGraw-Hill Professional, .
- Kraichnan, R. H. (1970). "Diffusion by a random velocity field." *Phys. Fluids*, 13 22.
- Kujundzic, E., Hernandez, M., and Miller, S. L. (2007). "Ultraviolet germicidal irradiation inactivation of airborne fungal spores and bacteria in upper-room air and HVAC in-duct configurations." *Journal of Environmental Engineering and Science*, 6(1), 1-9.
- Kumar, S., and Ramkrishna, D. (1996a). "On the solution of population balance equations by discretization—I. A fixed pivot technique." *Chemical Engineering Science*, 51(8), 1311-1332.

- Kumar, S., and Ramkrishna, D. (1996b). "On the solution of population balance equations by discretization—II. A moving pivot technique." *Chemical Engineering Science*, 51(8), 1333-1342.
- Kvasnak, W., Ahmadi, G., and Schmidt, D. J. (2004). "An engineering model for the fuel spray formation of deforming droplets." *Atomization and Sprays*, 14(4).
- Lee, K. (1983). "Change of particle size distribution during Brownian coagulation." *J. Colloid Interface Sci.*, 92(2), 315-325.
- Lee, K., and Chen, H. (1984). "Coagulation rate of polydisperse particles." *Aerosol Science and Technology*, 3(3), 327-334.
- Lee, K., Lee, Y., and Han, D. (1997). "The log-normal size distribution theory for Brownian coagulation in the low Knudsen number regime." *J. Colloid Interface Sci.*, 188(2), 486-492.
- Lee, S., Lam, S., and Kin Fai, H. (2001). "Characterization of VOCs, ozone, and PM₁₀ emissions from office equipment in an environmental chamber." *Build. Environ.*, 36(7), 837-842.
- Leuzzi, G., and Monti, P. (1998). "Particle trajectory simulation of dispersion around a building." *Atmos. Environ.*, 32(2), 203-214.
- Levetin, E., Shaughnessy, R., Rogers, C. A., and Scheir, R. (2001). "Effectiveness of germicidal UV radiation for reducing fungal contamination within air-handling units." *Appl. Environ. Microbiol.*, 67(8), 3712-3715.
- Li, A., and Ahmadi, G. (1992). "Dispersion and deposition of spherical particles from point sources in a turbulent channel flow." *Aerosol Science and Technology*, 16(4), 209-226.
- Li, A., and Ahmadi, G. (1993). "Deposition of aerosols on surfaces in a turbulent channel flow." *Int. J. Eng. Sci.*, 31(3), 435-451.
- Li, A., Ahmadi, G., Bayer, R. G., and Gaynes, M. A. (1994). "Aerosol particle deposition in an obstructed turbulent duct flow." *J. Aerosol Sci.*, 25(1), 91-112.
- Li, Y., Huang, X., Yu, I., Wong, T., and Qian, H. (2005). "Role of air distribution in SARS transmission during the largest nosocomial outbreak in Hong Kong." *Indoor Air*, 15(2), 83-95.
- Lien, F. S., and Yee, E. (2004). "Numerical Modelling of the Turbulent Flow Developing Within and Over a 3-D Building Array, Part I: A High-Resolution Reynolds-Averaged Navier—Stokes Approach." *Bound.-Layer Meteorol.*, 112(3), 427-466.

- Lister, J., Smit, D., and Hounslow, M. (1995). "Adjustable discretized population balance for growth and aggregation." *AIChE J.*, 41(3), 591-603.
- Liu, C., and Ahmadi, G. (2006). "Transport and deposition of particles near a building model." *Build. Environ.*, 41(6), 828-836.
- Liu, S., and Lin, J. (2008). "Numerical Simulation of Nanoparticle Coagulation in a Poiseuille Flow Via a Moment Method." *Journal of Hydrodynamics, Ser.B*, 20(1), 1-9.
- Long, C. M., Suh, H. H., Kobzik, L., Catalano, P. J., Ning, Y. Y., and Koutrakis, P. (2001). "A pilot investigation of the relative toxicity of indoor and outdoor fine particles: in vitro effects of endotoxin and other particulate properties." *Environ. Health Perspect.*, 109(10), 1019.
- Long, C. M., Suh, H. H., and Koutrakis, P. (2000). "Characterization of indoor particle sources using continuous mass and size monitors." *J. Air Waste Manage. Assoc.*, 50(7), 1236-1250.
- Marchisio, D. L., and Fox, R. O. (2005). "Solution of population balance equations using the direct quadrature method of moments." *J. Aerosol Sci.*, 36(1), 43-73.
- Markutsya, S., Subramaniam, S., Vigil, R. D., and Fox, R. O. (2008). "On Brownian dynamics simulation of nanoparticle aggregation." *Ind Eng Chem Res*, 47(10), 3338-3345.
- Martinuzzi, R., and Tropea, C. (1993). "The flow around surface-mounted, prismatic obstacles placed in a fully developed channel flow." *TRANSACTIONS-AMERICAN SOCIETY OF MECHANICAL ENGINEERS JOURNAL OF FLUIDS ENGINEERING*, 115 85-85.
- Maus, R., and Umhauer, H. (1997). "Collection efficiencies of coarse and fine dust filter media for airborne biological particles." *J. Aerosol Sci.*, 28(3), 401-415.
- McDevitt, J. J., Milton, D. K., Rudnick, S. N., and First, M. W. (2008). "Inactivation of poxviruses by upper-room UVC light in a simulated hospital room environment." *PLoS One*, 3(9), e3186.
- McGraw, R. (1997). "Description of aerosol dynamics by the quadrature method of moments." *Aerosol Science and Technology*, 27(2), 255-265.
- McLaughlin, J. B. (1989). "Aerosol particle deposition in numerically simulated channel flow." *Physics of Fluids A: Fluid Dynamics*, 1 1211.
- Mito, Y., and Hanratty, T. J. (2002). "Use of a modified Langevin equation to describe turbulent dispersion of fluid particles in a channel flow." *Flow, Turbulence and Combustion*, 68(1), 1-26.

- Miller, S. L., and Macher, J. M. (2000). "Evaluation of a methodology for quantifying the effect of room air ultraviolet germicidal irradiation on airborne bacteria." *Aerosol.Sci.Technol.*, 33(3), 274-295.
- Mirzai, M., Harvey, J., and Jones, C. (1994). "Wind tunnel investigation of dispersion of pollutants due to wind flow around a small building." *Atmos.Environ.*, 28(11), 1819-1826.
- Montgomery, T. L., and Corn, M. (1970). "Aerosol deposition in a pipe with turbulent airflow." *J.Aerosol Sci.*, 1(3), 185-213.
- Montgomery, R. D., and Baker, R. (2006). "Study verifies coil cleaning saves energy." *ASHRAE J.*, 48(11), 34-38.
- Murakami, S., Mochida, A., and Hayashi, Y. (1990). "Examining the κ - ϵ model by means of a wind tunnel test and large-eddy simulation of the turbulence structure around a cube." *J.Wind Eng.Ind.Aerodyn.*, 35(0), 87-100.
- Nakamura, H., Igarashi, T., and Tsutsui, T. (2001). "Local heat transfer around a wall-mounted cube in the turbulent boundary layer." *Int.J.Heat Mass Transfer*, 44(18), 3385-3395.
- Nambiar, D., Kumar, R., Das, T., and Gandhi, K. (1992). "A new model for the breakage frequency of drops in turbulent stirred dispersions." *Chemical Engineering Science*, 47(12), 2989-3002.
- Nazaroff, W. W., and Weschler, C. J. (2004). "Cleaning products and air fresheners: exposure to primary and secondary air pollutants." *Atmos.Environ.*, 38(18), 2841-2865.
- Nazridoust, K., and Ahmadi, G. (2006). "Airflow and pollutant transport in street canyons." *J.Wind Eng.Ind.Aerodyn.*, 94(6), 491-522.
- NIOSH. (2009). *Environmental control for tuberculosis: Basic upper-room ultraviolet germicidal irradiation guidelines for healthcare settings*. NIOSH, .
- Ochoa, J., and Fueyo, N. (2004). "Large Eddy Simulation of the flow past a square cylinder." *PHOENICS Journal of Computational Fluid Dynamics and its Applications*, 17.
- Otto, E., Stratmann, F., Fissan, H., Vemury, S., and Pratsinis, S. E. (1994). "Quasi-Self-Preserving Log-Normal Size Distributions in the Transition Regime." *Particle and Particle Systems Characterization*, 11(5), 359-366.
- Otto, E., Stratmann, F., Fissan, H., Vemury, S., and Pratsinis, S. E. (1993). "39 P 17 Brownian coagulation in the transition regime II: A comparison of two modelling approaches." *J.Aerosol Sci.*, 24, Supplement 1(0), S535-S536.

- Ounis, H., Ahmadi, G., and McLaughlin, J. B. (1991). "Dispersion and deposition of Brownian particles from point sources in a simulated turbulent channel flow." *J.Colloid Interface Sci.*, 147(1), 233-250.
- Papavergos, P., and Hedley, A. (1984). "Particle deposition behaviour from turbulent flows." *Chemical Engineering Research and Design*, 62(5), 275-295.
- Park, S., Lee, K., Otto, E., and Fissan, H. (1999). "The log-normal size distribution theory of brownian aerosol coagulation for the entire particle size range:: Part I-- analytical solution using the harmonic mean coagulation kernel." *J.Aerosol Sci.*, 30(1), 3-16.
- Pirjola, L., Tsyro, S., Tarrason, L., and Kulmala, M. (2003). "A monodisperse aerosol dynamics module, a promising candidate for use in long-range transport models: Box model tests." *J.Geophys.Res*, 108(D9), 4258.
- Pope, S. (1979). "A rational method of determining probability distributions in turbulent reacting flows." *J.Non-Equilib.Thermodyn*, 4(309), 1979.
- Pozorski, J., and Apte, S. V. (2009). "Filtered particle tracking in isotropic turbulence and stochastic modeling of subgrid-scale dispersion." *Int.J.Multiphase Flow*, 35(2), 118-128.
- Pratsinis, S. E. (1988). "Simultaneous nucleation, condensation, and coagulation in aerosol reactors." *J.Colloid Interface Sci.*, 124(2), 416-427.
- Qian, J., Tavakoli, B., Goldasteh, I., Ahmadi, G., Ferro, A., R., (2014). "Building removal of particulate pollutant plume during outdoor resuspension event." *Building and Environment*, 75, 161-169.
- Reed, N. G. (2010). "The History of Ultraviolet Germicidal Irradiation for Air Disinfection." *Public Health Rep.*, 125(1), 15.
- Rigopoulos, S. (2007). "PDF method for population balance in turbulent reactive flow." *Chemical Engineering Science*, 62(23), 6865-6878.
- Robinson, J. P., Thomas, J., and Behar, J. V. (1991). "Report to the United States Environmental Protection Agency under Contract No. 69-01-7324, Delivery Order 12, Exposure Assessment Research Division." .
- Rodi, W. (1998). "Large-eddy simulations of the flow past bluff bodies: state-of-the art." *JSME International Journal.Ser.B, Fluids and Thermal Engineering*, 41(2), 361-374.
- Rodi, W. (1997a). "Comparison of LES and RANS calculations of the flow around bluff bodies." *J.Wind Eng.Ind.Aerodyn.*, 69 55-75.

- Rodi, W., Ferziger, J.H., Breuer, M., Pourquie, M., (1997b). "Status of large-eddy simulation: results of a workshop." *J.Fluids Eng.*, 119 248-262.
- Rohr, A. C., Weschler, C. J., Koutrakis, P., and Spengler, J. D. (2003). "Generation and quantification of ultrafine particles through terpene/ozone reaction in a chamber setting." *Aerosol.Sci.Technol.*, 37(1), 65-78.
- Rudnick, S. N., and First, M. W. (2007). "Fundamental factors affecting upper-room ultraviolet germicidal irradiation—part II. Predicting effectiveness." *Journal of Occupational and Environmental Hygiene*, 4(5), 352-362.
- Rutala, W. A., Jones, S. M., Worthington, J. M., Reist, P. C., and Weber, D. J. (1995). "Efficacy of portable filtration units in reducing aerosolized particles in the size range of *Mycobacterium tuberculosis*." *Infection Control and Hospital Epidemiology*, 391-398.
- Santanam, S., Spengler, J. D., and Ryan, P. B. (29 July- 3 August 1990). "Particulate matter exposures estimated from an indoor-outdoor source apportionment study." *The 5th International Conference on Indoor Air Quality and Climate*, 583-588.
- Sarwar, G., Corsi, R., Allen, D., and Weschler, C. (2003). "The significance of secondary organic aerosol formation and growth in buildings: experimental and computational evidence." *Atmos.Environ.*, 37(9–10), 1365-1381.
- Scales, J. A., and Tenorio, L. (2001). "Prior information and uncertainty in inverse problems." *Geophysics*, 66(2), 389-397.
- Shah, K. B., and Ferziger, J. H. (1997). "A fluid mechanics view of wind engineering: Large eddy simulation of flow past a cubic obstacle." *J.Wind Eng.Ind.Aerodyn.*, 67 211-224.
- Shams, M., Ahmadi, G., and Rahimzadeh, H. (2000). "A sublayer model for deposition of nano- and micro-particles in turbulent flows." *Chemical Engineering Science*, 55(24), 6097-6107.
- Shotorban, B., and Mashayek, F. (2005). "Modeling subgrid-scale effects on particles by approximate deconvolution." *Phys.Fluids*, 17 081701.
- Singer, B. C., Coleman, B. K., Destailats, H., Hodgson, A. T., Lunden, M. M., Weschler, C. J., and Nazaroff, W. W. (2006). "Indoor secondary pollutants from cleaning product and air freshener use in the presence of ozone." *Atmos.Environ.*, 40(35), 6696-6710.
- Smirnov, A., Shi, S., and Celik, I. (2001). "Random flow generation technique for large eddy simulations and particle-dynamics modeling." *Journal of Fluids Engineering*, 123 359.

- Smoluchowski, M. (1917). "Versuch einer mathematischen Theorie der Koagulationskinetik kolloider Lösungen." *Z.Phys.Chem.*, 92(129-168), 9.
- Stathopoulos, T., and Zhou, Y. S. (1993). "Numerical simulation of wind-induced pressures on buildings of various geometries." *J.Wind Eng.Ind.Aerodyn.*, 46–47(0), 419-430.
- Suh, S., M., Zachariah, M., R. and Girshick, S., L., (2002). "Numerical modeling of silicon oxide particle formation and transport in a one-dimensional low-pressure chemical vapor deposition reactor." *Journal of Aerosol Science*, 33, 943-959.
- Sutton, P., Mossman, M., Reinisch, F., and Harrison, R. (2002). "A determination of healthcare worker exposure to Mycobacterium tuberculosis in two Californian hospitals." *J. Hosp. Infect.*, 51(4), 281-287.
- Tennekes H., Lumley J.L. (1972). "A First Course in Turbulence." *Cambridge, MA: MIT Pres*, 65-68.
- Tian, L., and Ahmadi, G. (2007). "Particle deposition in turbulent duct flows-- comparisons of different model predictions." *J.Aerosol Sci.*, 38(4), 377-397.
- Toftum, J., Freund, S., Salthammer, T., and Weschler, C. J. (2008). "Secondary organic aerosols from ozone-initiated reactions with emissions from wood-based materials and a "green" paint." *Atmos. Environ.*, 42(33), 7632-7640.
- Turkiyyah, G., Reed, D., and Yang, J. (1995). "Fast vortex methods for predicting wind-induced pressures on buildings." *J.Wind Eng.Ind.Aerodyn.*, 58(1–2), 51-79.
- Tutar, M., and Oguz, G. (2002). "Large eddy simulation of wind flow around parallel buildings with varying configurations." *Fluid Dyn.Res.*, 31(5-6), 289-315.
- U.S. DHHS. (2009). "National healthcare quality report." *U.S. Department of Health and Human Services. Agency for Healthcare Research and Quality (AHRQ) Publication*, .
- van Hooff, T., and Blocken, B. (2010). "Coupled urban wind flow and indoor natural ventilation modelling on a high-resolution grid: A case study for the Amsterdam Arena stadium." *Environmental Modelling and Software*, 25(1), 51-65.
- Wang, L., and Fox, R. O. (2003). "Application of in situ adaptive tabulation to CFD simulation of nano-particle formation by reactive precipitation." *Chemical Engineering Science*, 58(19), 4387-4401.
- Weschler, C. J. (2000). "Ozone in indoor environments: concentration and chemistry." *Indoor Air*, 10(4), 269-288.

- Weschler, C. J., and Shields, H. C. (2003). "Experiments probing the influence of air exchange rates on secondary organic aerosols derived from indoor chemistry." *Atmos. Environ.*, 37(39-40), 5621-5631.
- Weschler, C. J. (2009). "Changes in indoor pollutants since the 1950s." *Atmos. Environ.*, 43(1), 153-169.
- Williams, M. (1986). "Some topics in nuclear aerosol dynamics." *Prog. Nuclear Energy*, 17(1), 1-52.
- Winkler, C. M., Rani, S. L., and Vanka, S. P. (2006). "A numerical study of particle wall-deposition in a turbulent square duct flow." *Powder Technol.*, 170(1), 12-25.
- Wong, P., Ko, N., and Chiu, A. (1995). "Flow characteristics around two parallel adjacent square cylinders of different sizes." *J. Wind Eng. Ind. Aerodyn.*, 54 263-275.
- Wood, N. (1981). "A simple method for the calculation of turbulent deposition to smooth and rough surfaces." *J. Aerosol Sci.*, 12(3), 275-290.
- Wright, D. L. (2000). "Retrieval of optical properties of atmospheric aerosols from moments of the particle size distribution." *J. Aerosol Sci.*, 31(1), 1-18.
- Wu, J., and Menon, S. (2001). "Aerosol dynamics in the near field of engine exhaust plumes." *J. Appl. Meteorol.*, 40(4), 795-809.
- Xia, J., and YC Leung, D. (2001). "Pollutant dispersion in urban street canopies." *Atmos. Environ.*, 35(11), 2033-2043.
- Xu, P., Peccia, J., Fabian, P., Martyny, J. W., Fennelly, K. P., Hernandez, M., and Miller, S. L. (2003). "Efficacy of ultraviolet germicidal irradiation of upper-room air in inactivating airborne bacterial spores and mycobacteria in full-scale studies." *Atmos. Environ.*, 37(3), 405-419.
- Yakhot, A., Liu, H., and Nikitin, N. (2006). "Turbulent flow around a wall-mounted cube: A direct numerical simulation." *Int J Heat Fluid Flow*, 27(6), 994-1009.
- Zhang, H., and Ahmadi, G. (2000). "Aerosol particle transport and deposition in vertical and horizontal turbulent duct flows." *J. Fluid Mech.*, 406(1), 55-88.
- Zhang, H., Ahmadi, G., Fan, F. G., and McLaughlin, J. B. (2001). "Ellipsoidal particles transport and deposition in turbulent channel flows." *Int. J. Multiphase Flow*, 27(6), 971-1009.
- Zhu, Y., and Hinds, W. C. (2005). "Predicting particle number concentrations near a highway based on vertical concentration profile." *Atmos. Environ.*, 39(8), 1557-1566.

APPENDIX

The user defined function (UDF) developed to model turbulent velocity fluctuations in RSTM turbulence model of a channel flow. The quadratic variation of normal velocity fluctuations near the wall as suggested by Li and Ahmadi (2007), $\sqrt{v'^2} \propto y^2$ as $y \rightarrow 0$ is considered.

```
/* Unsteady Particle Tracking */
/* control on initialization in DPM Scalar Update */
/* access to the cell and particle macros */
#include "udf.h"
#include "dpm.h"
#include "random.h"
#define ustr 0.320713
#define NU 0.000014607346

DEFINE_DPM_SCALAR_UPDATE (vFluctutn,cell,thread,initialize,p)
{
    real delT = CURRENT_TIMESTEP;
    real TE, TEp, yp, zig1, zig2;
    real t0, td, pResTime;
    t0 = p->time_of_birth;
    td = P_TIME(p);
    pResTime = td-t0;
    if (pResTime > delT){initialize = 0;}
    if (initialize)
    {
        P_USER_REAL(p,0) = sqrt(C_RUU(cell,thread));
        P_USER_REAL(p,1) = sqrt(C_RVV(cell,thread));
    }
    else
    {
        if (P_POS(p)[1] <= 0.015 && P_POS(p)[1] >= 0.005)
        {
            TE = (2./14.)*(C_K(cell,thread))/(C_D(cell,thread));
            /*middle******/
            P_USER_REAL(p,0) = P_USER_REAL(p,0)*(1-
            delT/TE)+sqrt(2.*delT/TE*C_RUU(cell,thread))*gauss_random
            P_USER_REAL(p,1) = P_USER_REAL(p,1)*(1-
            delT/TE)+sqrt(2.*delT/TE*C_RVV(cell,thread))*gauss_random();
        }
    }
}
```

```

    }
    else if (P_POS(p)[1] > 0.001 && P_POS(p)[1] < 0.005)
    {
        yp = (P_POS(p)[1])*ustr/NU;
        TEp = 7.122+0.5731*yp-0.00129*yp*yp;
        TE = TEp*NU/(ustr*ustr);

/*logLayer1*****/
        zig1=ustr*0.4*yp/(1+0.0239*pow(yp,1.496));
        zig2=ustr*0.0116*pow(yp,2)/(1.+0.203*yp+0.0014*pow(yp,2.421));
        P_USER_REAL(p,0) = P_USER_REAL(p,0)*(1-
delt/TE)+sqrt(2.*delt/TE)*zig1*gauss_random();
        P_USER_REAL(p,1) = P_USER_REAL(p,1)*(1-
delt/TE)+sqrt(2.*delt/TE)*zig2*gauss_random();
    }
    else if (P_POS(p)[1] < 0.001)
    {
        yp = (P_POS(p)[1])*ustr/NU;
        TEp = 10;
        TE = TEp*NU/(ustr*ustr);

/*subLayer1*****/
        zig1=ustr*0.4*yp/(1+0.0239*pow(yp,1.496));
        zig2=ustr*0.0116*pow(yp,2)/(1.+0.203*yp+0.0014*pow(yp,2.421));
        P_USER_REAL(p,0) = P_USER_REAL(p,0)*(1-
delt/TE)+sqrt(2.*delt/TE)*zig1*gauss_random();
        P_USER_REAL(p,1) = P_USER_REAL(p,1)*(1-
delt/TE)+sqrt(2.*delt/TE)*zig2*gauss_random();
    }
    else if (P_POS(p)[1] <= 0.019 && P_POS(p)[1] >= 0.015)
    {
        yp = (0.02-P_POS(p)[1])*ustr/NU;
        TEp = 7.122+0.5731*yp-0.00129*yp*yp;
        TE = TEp*NU/(ustr*ustr);

/*logLayer2*****/
        zig1=ustr*0.4*yp/(1+0.0239*pow(yp,1.496));
        zig2=ustr*0.0116*pow(yp,2)/(1.+0.203*yp+0.0014*pow(yp,2.421));
        P_USER_REAL(p,0) = P_USER_REAL(p,0)*(1-
delt/TE)+sqrt(2.*delt/TE)*zig1*gauss_random();
        P_USER_REAL(p,1) = P_USER_REAL(p,1)*(1-
delt/TE)+sqrt(2.*delt/TE)*zig2*gauss_random();
    }

```

```

        else if (P_POS(p)[1] > 0.019)
        {
            yp = (0.02-P_POS(p)[1])*ustr/NU;
            TEp = 10;
            TE = TEp*NU/(ustr*ustr);

            /*subLayer2*****
            zig1=ustr*0.4*yp/(1+0.0239*pow(yp,1.496));
            zig2=ustr*0.0116*pow(yp,2)/(1.+0.203*yp+0.0014*pow(yp,2.421));
            P_USER_REAL(p,0) = P_USER_REAL(p,0)*(1-
delt/TE)+sqrt(2.*delt/TE)*zig1*gauss_random();
            P_USER_REAL(p,1) = P_USER_REAL(p,1)*(1-
delt/TE)+sqrt(2.*delt/TE)*zig2*gauss_random();
        }
    }
    /* Message("u'= %f v'=%f\n birthTime = %f pTime = %f pID =
%d\n",P_USER_REAL(p,0), P_USER_REAL(p,1), p->time_of_birth, P_TIME(p),
P_INJ_ID(P_INJECTION(p))); */
}

DEFINE_DPM_BODY_FORCE(fluctF,p, i)
{
    /* get the cell and Thread that the particle is currently in */
    cell_t cc = RP_CELL(&(p->cCell));
    Thread *tt = RP_THREAD(&(p->cCell));
    real dp, CD, Sp, ttau, Rep, FD;
    real bForce=0.;
    dp = P_DIAM(p);
    Sp = 2400.; /*Rop/Rof*/
    //NU = MU/1.225;
    ttau = Sp*dp*dp/(18.*NU);
    Rep = dp/NU*sqrt(pow((C_U(cc,tt)-P_VEL(p)[0]),2)+pow((C_V(cc,tt)-
P_VEL(p)[1]),2));
    CD = (24./Rep)*(1+0.15*pow(Rep,0.687));
    FD = (1./ttau)*CD*(Rep/24);
    /* ***** Body Force ***** */
    if(i==0) {bForce= FD*P_USER_REAL(p,0);}
    if(i==1) {bForce= FD*P_USER_REAL(p,1);}

    /*Message("bodyForce= %f Reyp= %f CD= %f FD= %f\n
",P_POS(p)[1],Rep,CD,FD);*/
    return (bForce);
}

```

The user defined function (UDF) developed to model sub-grid scale (SGS) velocity fluctuations in LES turbulence model of the flow over a bluff body with complex geometry,

```

/* Unsteady Particle Tracking */
/* control on initialization in DPM Scalar Update */
/* access to the cell and particle macros - #define ustr 0.320713 */
#include "udf.h"
#include "dpm.h"
#include "random.h"
#define NU 0.000014607346
DEFINE_DPM_SCALAR_UPDATE(vFluctutn,c,t,initialize,p)
{
    real delt = CURRENT_TIMESTEP;
    float tau_sg, tau_Lp, tau_Ln, epsi, zig_sg; /*beta=TL/TE*/
    real t0, td, pResTime;
    real vol, Vmag, Vpmag;
    t0 = p->time_of_birth;
    td = P_TIME(p);
    pResTime = td-t0;
    if (pResTime > delt){initialize = 0;}
    if (initialize)
    {
        P_USER_REAL(p,0) = sqrt(2./3.*C_K(c,t));
        P_USER_REAL(p,1) = sqrt(2./3.*C_K(c,t));
    }
    else
    {
        zig_sg = sqrt(2./3.*C_K(c,t));
        /* ***** */
        vol = C_VOLUME(c,t);
        tau_sg = pow(vol,0.3333)/zig_sg;
        /* ***** */
        Vmag = pow(C_U(c,t),2)+pow(C_V(c,t),2)+pow(C_W(c,t),2);
        Vmag = sqrt(Vmag);
        Vpmag = pow(P_VEL(p)[0],2)+pow(P_VEL(p)[1],2)+pow(P_VEL(p)[2],2);
        Vpmag = sqrt(Vpmag);
        epsi = fabs(Vmag-Vpmag)/zig_sg;
        /* ***** */
        tau_Lp = tau_sg/(sqrt(1.+pow(epsi,2)));
    }
}

```

```

tau_Ln = tau_sg/(sqrt(1.+4.*pow(epsi,2)));
/* ***** */
P_USER_REAL(p,0) = exp(-delt/tau_Ln)*P_USER_REAL(p,0)+zig_sg*sqrt(1-exp(-
2*delt/tau_Ln))*gauss_random();
P_USER_REAL(p,1) = exp(-delt/tau_Lp)*P_USER_REAL(p,1)+zig_sg*sqrt(1-exp(-
2*delt/tau_Lp))*gauss_random();
P_USER_REAL(p,2) = exp(-delt/tau_Ln)*P_USER_REAL(p,2)+zig_sg*sqrt(1-exp(-
2*delt/tau_Ln))*gauss_random();
/* ***** */
/*Message("u'= %f v'=%f\n tau_Lp = %f tau_Ln = %f \n Vpmag = %f Vmag = %f
epsi = %f\n",P_USER_REAL(p,0), P_USER_REAL(p,1), tau_Lp, tau_Ln, Vpmag, Vmag,
epsi);*/
}
}
// Message("u'= %f v'=%f\n birthTime = %f pTime = %f pID =
%d\n",P_USER_REAL(p,0), P_USER_REAL(p,1), p->time_of_birth, P_TIME(p),
P_INJ_ID(P_INJECTION(p)));

DEFINE_DPM_BODY_FORCE(fluctF,p, i)
{
/* get the cell and Thread that the particle is currently in */
cell_t cc = RP_CELL(&(p->cCell));
Thread *tt = RP_THREAD(&(p->cCell));
real dp, CD, Sp, ttau, Rep, FD;
real bForce=0.;
dp = P_DIAM(p);
Sp = 2400.; /*Rop/Rof*/
//NU = MU/1.225;
ttau = Sp*dp*dp/(18.*NU);
Rep = dp/NU*sqrt(pow((C_U(cc,tt)-P_VEL(p)[0]),2)+pow((C_V(cc,tt)-
P_VEL(p)[1]),2)+pow((C_W(cc,tt)-P_VEL(p)[2]),2));
CD = (24./Rep)*(1+0.15*pow(Rep,0.687));
FD = (1./ttau)*CD*(Rep/24);
/* ***** Body Force ***** */
if(i==0) {bForce= FD*P_USER_REAL(p,0);}
if(i==1) {bForce= FD*P_USER_REAL(p,1);}
if(i==2) {bForce= FD*P_USER_REAL(p,2);}
//{ //bForce= DD*C_UDSI(cc,tt,3);
/*if ((P_POS(p)[1] > 0.008) || (P_POS(p)[1] < -0.008)) {bForce=
DD*P_USER_REAL(p,1)-DD*(C_V(cc,tt));}*/
//else{bForce= FD*P_USER_REAL(p,1);}
//}
/*if(i==2) bForce= FD*C_UDSI(c,t,2); */

```

```
        //Message("bodyForce= %f Reyp= %f CD= %f FD= %f\n",P_POS(p)[1],Rep,CD,FD);  
        return (bForce);  
    }
```